10-26-2016 12:00 AM

Energy Subtraction Methods as an Alternative to Conventional X-Ray Angiography

Christiane S. Burton, *The University of Western Ontario*

Recommended Citation

Abstract

Cardiovascular diseases (CVD) are currently the leading cause of death worldwide and x-ray angiography is used to assess a vast majority of CVD cases. Digital subtraction angiography (DSA) is a technique that is widely used to enhance the visibility of small vessels obscured by background structures by subtracting a mask and contrast image. However, DSA is generally unsuccessful for imaging the heart due to the motion that occurs between mask and contrasted images which cause motion artifacts. An alternative approach, known as dual-energy or energy subtraction angiography (ESA) is one that exploits the iodine k-edge by acquiring images with a low and high kV in rapid succession. The idea for ESA is to bring the benefits of DSA to cardiac imaging without motion artifacts. However, it was concluded in 1970's that image quality for ESA could not compete with that of DSA, and the approach was abandoned. We believe that this was due to technical limitations. In our work we show that conclusions about iodine SNR for ESA were based on limitations of early technical components that are no longer relevant. The goals of this thesis were to: 1) develop a theoretical model of iodine SNR that is independent of technology for DSA and ESA and validate our theory with experiment, and then factor in technical components; 2) optimize the iodine SNR for ESA based on parameters that a user can control; 3) image ESA in an anthropomorphic phantom to visualize bone suppression. It is shown that scatter and read noise were technical components that degraded iodine SNR for ESA in the past and both can overcome today. It is concluded that, when these conditions are satisfied, ESA iodine SNR equal to that of DSA for low iodine mass loadings (sufficient for artery sizes) for the same patient entrance exposure, and therefore may provide alternatives to DSA in situations where motion artifacts are expected to render a study as non-diagnostic, such as in coronary applications. In the future this will have important applications for subtraction imaging of the coronary arteries and other vessels where stenosis is vital to patient health.

Keywords

Co-Authorship

This thesis contains material from manuscripts either published or submitted for publication. Permission to reproduce manuscripts published in Medical Physics (American Institute of Physics) is included in Appendix .

Chapter 2 is based on an article "Energy subtraction angiography is comparable to digital subtraction angiography in terms of iodine Rose SNR" by Christiane S. Burton, John R. Mayo and Ian A. Cunningham that has been accepted for publication in Medical Physics (in press). I was responsible for study concept, mathematical developments, experimental design and execution, data simulation, data analysis and interpretation, and manuscript preparation, all of which was performed under the supervision of I. A. Cunningham.

Chapter 3 is based on the manuscript "Optimizing iodine SNR per root air KERMA for energy subtraction methods" by Christiane S. Burton, John R. Mayo, and I. A. Cunningham that has been submitted to Medical Physics for consideration for publication. I was responsible for study concept, mathematical developments, data simulation, data analysis and interpretation, and preparation of the manuscript, all under the supervision of I. A. Cunningham.

Chapter 4 is based on the manuscript "Energy-subtraction method in RANDO anthropomorphic phantom" by Christiane S. Burton, John R. Mayo and Ian A. Cunningham that will be submitted for consideration for publication in Medical Physics. I was responsible for study concept, mathematical developments, experimental design and execution, data simulation, data analysis and interpretation, and manuscript preparation, all of which was performed under the supervision of I. A. Cunningham.

Acknowledgements

My greatest acknowledgement is to my supervisor Dr. Ian A. Cunningham for all of his patience and guidance during my project in helping me develop skills that are necessary to be a successful scientist. It has been an honour to work with such a brilliant scientist and mentor. He has inculcated important skills in me such as cogency in my communication and forward thinking in my research that are required in science and everyday life (even grocery shopping!). I want to thank him for his patience and helping me to understand what it means to be a very good scientist. Dr. Cunningham's continued enthusiasm for asking important scientific questions in the field of medical imaging is inspiring and has made my graduate studies an enjoyable and rewarding yet challenging experience.

I would like to thank my advisory committee (in no particular order), Dr. Aaron So, Dr. George Hajdok, and Dr. Eugene Wong, for their valuable time and for keeping my project on track and helping me plan and address important scientific questions for my papers and thesis.

I would like to thank the administrative support of Barb Citton and Wendy Hough from the Department of Medical Biophysics, and Janice Kroenig from the Imaging Laboratories at Robarts Research Institute. Barb and Wendy provided invaluable guidance regarding submission procedures for graduate scholarship applications and Janice was especially helpful when it came to filling out expense reports.

I would like to thank the Cunningham group's laboratory assistant Michael (Mike) McDonald, MEng. Mike was very helpful in the construction of phantoms, and during our lab meetings has always provided valuable insight on my research. I would also like to acknowledge the scientific discussions I have had with Dr Jesse Tanguay, PhD, whom was very helpful at the beginning of my degree when I was trying to pick up where he left off. I would like to thank the newest additions to our lab, PhD candidate Tomi Nano and MSc candidate Terenz whom gave me ideas on how to present my work and who were supportive.

Contents

List of Tables

List of Figures

List of Symbols

In the following, overhead ˜ indicates a random variable, superscript † indicates a sampled detector signal consisting of a uniformly spaced distribution of δ-functions scaled by element signals, and RPP indicates a random point process consisting of a spatial distribution of randomly positioned δ-functions in the image plane.

Symbol	Definition
q_o , q_b	mean numbers of quanta per unit area [mm^{-2}] (image brightness) in object and background regions, respectively
A	area of pixel
C	object contrast (relative incremental change in scene brightness), $(q_o - q_b)/q_b$
N_b	mean number of background quanta measured in area A
σ_{N_b}	standard deviation in the number of background quanta measured in area A
d_I , d_W	uncorrelated pixels with mean values in iodinated and non-iodinated regions
σ_{d_W}	
$N_A \times N_A$	number of pixels in binned pixel
$K_d[\Delta]$	discrete auto-covariance function, $\Delta \neq 0$ only for uncorrelated pixels
$R(N_A)$	Ratio of auto-covariance function
q_S	number of scattered quanta per unit area [mm^{-2}]
k	constant of proportionality [keV^{-1}]
α	detector quantum efficiency
E_a	average energy absorbed in the binned pixel with each interaction
σ_R^2	detector additive readout noise
Q_o	number of quanta/mm^2/Gy

$D_\mathrm{W}, D_\mathrm{I}$ binned pixel values in iodinated and non-iodinated regions of a log-subtracted image

$\Delta D_\mathrm{D}, \triangle D_\mathrm{E}$ difference between binned pixel values for DSA, ESA

m,c   identify mask and contrast images for DSA

T_I iodine transmission

$\sigma^2_{\Delta D_\mathrm{D}}, \sigma^2_{\Delta D_\mathrm{E}}$ obtained by differentiating ΔD_D, $\triangle D_\mathrm{E}$ with respect to d_w

σ^2_c Pixel variance in photon-counting image.

l,h   low and high kV spectra

w ratio between mass attenuation coefficients of water at effective energies E_l and E_h

$\mathscr{K}_q$ Patient entrance air KERMA [μGy]

$\frac{\mu_{en}}{\rho}_{air}(E)$ Autocorrelation of $\tilde{c}(\mathbf{r})$.

List of Abbreviations

Symbol	Definition
CVD	Cardiovascular Diseases
CAD	Coronary Artery Disease
ECG	Electrocardiograph
DSA	Digital Subtraction Angiography
ESA	Energy Subtraction Angiography
ERA	Energy Resolving Angiography
SNR	Signal-to-Noise Ratio
FOM	Figure-of-Merit
SOV	Sum of Variance
CsI	Cesium Iodide
Se	Selenium
Gd_2O_2S	Gadolinium(III) Oxisulphide
CMOS	Complementary Metal-Oxide Semiconductor
kV	kilovoltage
mAs	product of current (mA) and exposure time (s)
DQE	Detector Quantum Efficiency
air KERMA	"Kinetic Energy Released per unit MAss in air", defined as the sum of the initial kinetic energies of all the charged particles liberated by uncharged ionizing radiation (i.e., indirectly ionizing radiation such as photons and neutrons) in a sample of matter, divided by the mass of the sample
DEXA	Dual-Energy X-ray Absorptiometry
DI	Detectability Index
ROC	Receiver Operating Characteristic
CNR	Contrast-to-Noise Ratio

Chapter 1

Introduction

1.1 Prevalence and forms of cardiovascular diseases (CVD)

According to the World Health Organization (WHO) cardiovascular diseases (CVDs) are currently the leading cause of mortality worldwide.[3] In 2011, Statistics Canada reported that the leading cause of death and acute care hospitalizations in Canada were CVDs, accounting for 30% of all deaths and 3 million hospitalizations.[15] In 2012, the organization estimated that 17.5 million people died of CVD, representing 31% of all global deaths.[145] In 2015, the Heart and Stroke Foundation reported that heart disease is the leading cause of death and disability in Canada, responsible for approximately 66,000 deaths each year.[39]

Cardiovascular disease is any disease involving blood vessels and all of these diseases involve atherosclerosis which is defined as the incomplete or complete blockage of blood vessels.[7] The etiology of atherosclerosis is described as the narrowing of the inner surface of an artery that is caused mainly by cholesterol uptake of white blood cells that accumulate along the inside of the vessel wall.[8] Examples of prevalent forms of CVDs resulting from atherosclerosis are coronary artery stenosis, carotid artery stenosis and cerebral aneurysms, acute limb ischaemia and pulmonary embolisms, and arteriovenous malformations (AVM) and renal artery stenosis.[7]

1.1.1 Coronary Artery Disease

In 2013 coronary artery disease (CAD) was the leading cause of death of all the CVDs.[92] Coronary artery disease develops when atherosclerosis occurs in the major blood vessels (coronary/epicardial arteries) that supply blood, oxygen and nutrients to the myocardium of the heart become damaged or diseased and may result in heart attacks and chest pain.

1.1.2 Other forms of CVD

WHO describes many other forms of CVD depending on the location the blood vessels are supplying. For example, cerebrovascular disease results from atherosclerosis in the carotid arteries leading to the head area and peripheral disease results from stenosis in blood vessels supplying the arms and legs. Another example is a pulmonary embolism (PE) is a blockage in one of the pulmonary arteries of the lungs which may be caused by a blood clot, fat globule, gas bubble or foreign material that travels to the lung from a blood vessel in the leg. In the case of PE not only does atherosclerosis impede the amount of blood traveling from the heart to the lungs, it causes increased pressure to the right ventricle thereby increasing blood pressure. The embolisms that originate from either the heart and pelvic region travel towards arteries in the leg, thigh, and lower limbs and cause acute limb ischaemia. Renal artery stenosis is caused by atherosclerosis that impedes blood flow to the target kidney in turn causing high blood pressure and atrophy of the affected kidney. CVD in any location can result in high blood pressure and has considerable impact on human health.

1.1.3 History of diagnostic techniques for CVD

CVD can affect an individual's health in many ways, therefore diagnostic images need to provide information on the location and severity of arterial narrowings (stenosis) for an accurate diagnosis.

1.1.3.1 Electrocardiogram limitation

Studies by Waller[141] in 1887 led to Einthoven inventing a string galvanometer. By hooking the galvanometer up to a patient and measuring various types of deflections[48] the electrocardiograph features could be used to describe and distinguish, and therefore diagnose, various cardiovascular diseases.[106] Today electrocardiography (ECG) is a device that detects electrical changes on the skin that arise from the myocardium depolarizing during each heartbeat.[72, 142] ECG is a commonly used diagnostic tool because it is simple to use, cost effective, and capable of diagnosing a diverse number of heart conditions. However, a major limitation of ECG is not having information on the specific location and severity of the artery narrowing.

A discovery in the 1890's would change that.

1.1.3.2 X-ray imaging

In 1895 Willhelm Roentgen discovered the production and detection of electromagnetic radiation in a wavelength range known as x-rays. He demonstrated this by taking an x-ray image of his wife's hand using film and even though the image appeared to be grainy there was contrast between the bones in her fingers, her ring and the background. There was a small group that picked up on x-ray imaging and noticed that blood vessels did not show up in the radiography image, and a year later they demonstrated that contrast could be created with use of a radio-opaque agent.

1.1.3.3 Contrast agents

In 1896, Haschek and Lindenthal were the very first group to demonstrate that vasculature could be seen in a radio graphic image by injecting calcium carbonate into cadavers.[1] Although this was an exciting discovery, they reported that calcium carbonate would not work in living beings. It was discovered later, in the 1920s, by Sicard and Forestier[115] that iodine-based contrast agent could be injected into a living human subject and since then
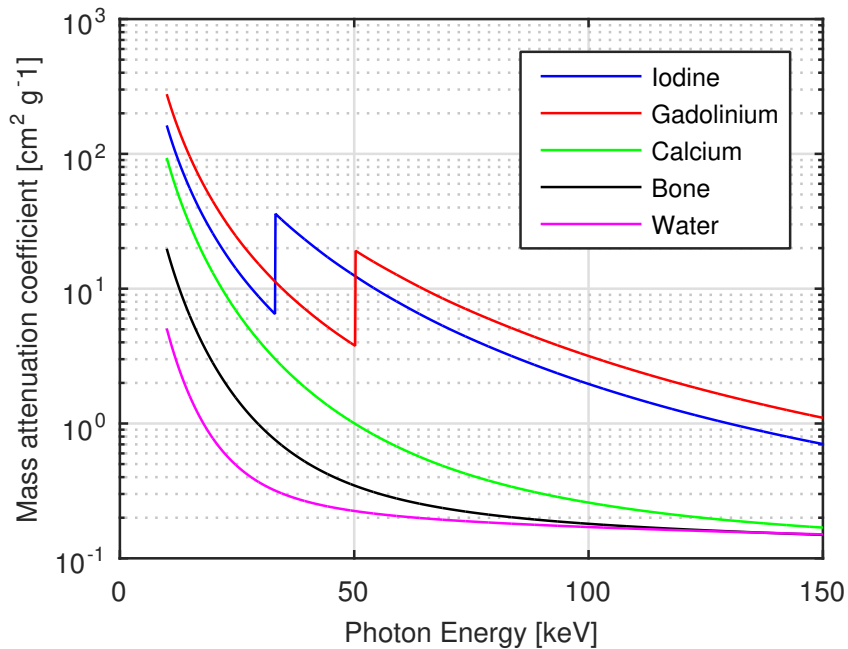
Figure 1.1.1: Attenuation properties of materials. Mass attenuation coefficients of iodine, calcium, bone, water, and gadolinium.

iodine has remained the most commonly used contrast agent in x-ray angiography.[28, 42, 43, 69, 70] The advantage of iodine over calcium carbonate is a K-edge at approximately 33.9 keV where the probability of photoelectric effect increases by a factor of 5, shown in Fig. 1.1.1. Iodine-based contrast agents were not used for imaging coronary arteries specifically until cardiac catheters were developed that would allow for selective injection of a contrast agent into the coronary arteries.

1.2   Cardiac catheterization

The concept of catheterization (without contrast injection) actually began in the early 1700's when Stephen Hales placed a long, thin, flexible tube, into the right and left ventricles of a live horse with the purpose of understanding the vascular system.[93] Variations on the technique were performed over the subsequent century until the 1840s when Claude Bernard picked up catheterization and used it to formally study cardiac physiology.[19] In

1927, not long after Sicard and Forestier demonstrated that iodine-based contrast agents can be used in live humans.[115] Around the same time, Dr Moniz for the first time used a catheter to inject iodine into vessels of the brain and imaged the head using x-rays, a method know today as cerebral angiography.[11] In 1929 Dr Werner Forssmann reported that he created an incision in one of his left antecubital veins and inserted a catheter into his venous system and then guided the catheter into his right atrium by taking many x-ray images to see inside his body.[29] In 1958 Dr Charles Dotter developed aortic root aortography where he would guide a catheter towards the aortic root and radiography contrast agent to visualize the coronary arteries very well.[25] He performed this procedure using animal models and reported that all animals survived afterwards. Mason Sones performed aortic root aortography later that year and reported that he had accidentally inserted a catheter into the patient's right coronary artery as the patient went into ventricular fibrillation and this resulted in the first known example of selective coronary arteriogram. The patient survived this procedure and it showed that contrast agent injected into the coronary artery was not fatal as was previously thought.[118]

1.2.1 Conventional angiography

In the early 1960s, angiography was emerging as a diagnostic procedure used for imaging patients that are candidates for having CVD. The purpose of performing angiography is to obtain an image with information on the location and severity of arterial stenosis. X-ray radiography is the most common imaging modality used for angiography[13, 62, 81, 23, 58] despite advances in other modalities such as intravenous ultrasound, CT, and MRI.[73, 123, 108] The advantage of using radiographs for angiography is that the images give a complete description of the stenosis with image resolution on the order of 0.1 mm.[126] However, the problem with angiography images is that in order to clearly see contrast between iodine-filled blood vessels from light and dark background structures such as lung and bone, respectively, the requirement is high radiation exposure and high concentrations
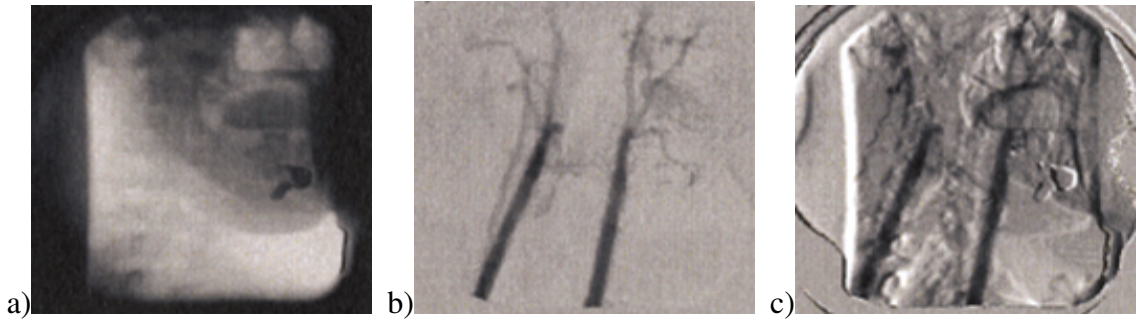
Figure 1.2.1: a) Mask image (left), b) DSA (center), c) and DSA with motion artifacts (right). Figure demonstrates how DSA images can be compromised by patient motion between mask and contrast images. (Permission to use images, image a) taken from reference [10] copyright line © 2008 IEEE, image b) taken from reference [10] copyright line © 2008 IEEE, and image c) taken from reference [10] copyright line © 2008 IEEE).

of iodine.

1.2.2 Necessity for subtraction methods for angiography

1.2.2.1 Digital subtraction angiography

Digital subtraction angiography (DSA) was discovered in the 1970's as a way of removing overlying bone, lung fields, and soft-tissue to produce iodine-specific images.[86, 4] A series of images of the anatomy (mask image) are acquired and subtracted from a series of images acquired after administration of iodine (contrast image) for the same region of interest. DSA can provide a clear image of the blood vessels where fig. 1.2.1 shows a single mask image, a DSA image with motion artifacts removed using motion correction, and DSA image with motion artifacts. DSA is primarily used for imaging arterial and venous occlusions, including carotid artery stenosis, pulmonary embolisms (pulmonary angiography) and acute limb ischaemia, renal artery stenosis, and cerebral aneurysms and arteriovenous malformations (AVM).[41, 98] The technique has been successfully used for mapping cerebral blood flow, detecting obstructions and lesions in the carotid arteries, and is also used for assessing patients prior to surgery and after coronary artery bypass surgery. DSA using radiography is considered the reference standard for vascular imaging

[65, 41] and it is therefore the reference technique that will be used when comparing new methods.[99]

1.2.2.2   Problem with digital subtraction angiography

The problem with DSA is that any motion that occurs in the several seconds between mask and contrast image acquisitions gives rise to motion artifacts, shown as light and dark regions, in the image and can render a study non-diagnostic.[78] Although software tools are available to assist with image registration for in-plane translation [139, 138, 140, 71, 137, 40, 147, 78, 10, 94] or rotation motions,[139, 138, 140, 71, 137, 260, 20, 40, 147, 78, 10, 94] cardiac and respiratory motion, swallowing after injection (carotid arteries), uncooperative patients, bowel and other involuntary motion remain the primary cause of failed image quality.[13, 17, 128] It is the need for a mask image that compromises image quality for DSA.[124]

1.2.3   The need for energy-dependent angiography

1.2.3.1   Introduction to dual-energy subtraction angiography

In 1953 Jacobson first attempted dual-energy subtraction using dichromatic absorption radiography.[49] Iodine-specific images were obtained by acquiring two images with low and high energies to exploit the K-edge discontinuity of the iodine mass attenuation coefficient.[4] This dual-energy subtraction concept developed throughout the late 1970's with notable studies by Mistretta,[86, 85, 84, 80, 81, 83, 87, 82] Kelcz,[59, 60] and other colleagues at the University of Wisconsin. Dual-energy was proposed as an alternative method to DSA for vascular imaging because it eliminated the need for a mask image.[86, 59, 105, 63, 46, 4] The idea was to implement a fast kV-switching generator to acquire low and high-kV images in rapid succession thereby making dual-energy angiography less sensitive to motion artifacts by eliminating the need for a mask image.[46, 13, 37, 90, 135] Early dual-energy
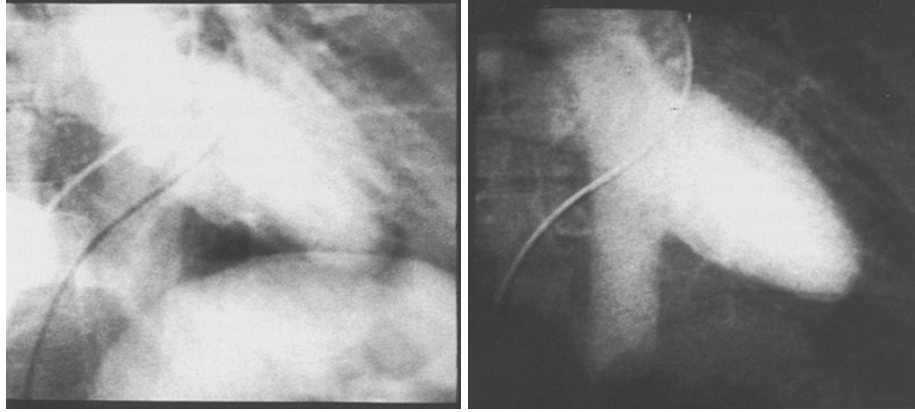
Figure 1.2.2: DSA (left) and ESA (right) images of an IV injection of the heart acquired in the 1990's. (Image taken from Ref. [135] Permission to reproduce is in Appendix.)

cardiac images published by Molloi and Mistretta[90] and Van Lysel[134, 135, 132, 136, 133] were exciting and demonstrated excellent insensitivity to motion artifacts. However, clinical implementation of energy subtraction was not generally adopted and showed less image quality in comparison to non-subtracted cardiac angiography. Fig 1.2.2 shows a dual-energy image of a dog's heart with the use of gating.

There are three well-known methods for energy-based subtraction described K-edge subtraction, [148, 86, 46, 13, 59, 60] triple-energy,[146, 59, 60, 107] and dual-energy.[121, 31, 66, 9, 30, 95, 114, 5, 13, 46, 37, 64, 4, 38, 74, 91, 90] each with their own benefits and limitations discussed in the next sub-sections.

1.2.3.2 K-edge subtraction

Jacobson[49] used x-ray sources with secondary radiation[18] to generate monoenergetic x-ray beams with energies that were below and above the iodine k-edge. However despite the ability to quantify iodine concentrations these secondary radiator sources were generally limited by low x-ray intensity and were not widely accepted as imaging tools.[84] Atkins et al. and Kramer et al. used solid state detectors for analyzing the energy of each photon forming the image produced by a conventional x-ray generator. Mistretta et al.[84] later demonstrated k-edge subtraction with quasi-monoenergetic spectra x-ray sources so

8

that higher quality images can be obtained in shorter times. However these energy analyses for each photon is time consuming and not practical.

In 1979 Houk et al.[46] demonstrated the method described by Mistretta in the left and right ventricles of a dog with minimal motion artifacts. Like Mistretta, Houk found that to generate quasi-monoenergetic beams in the clinic is impractical because it requires heavy filtration of low kV x-ray spectra and the very low number of photons at the kV of the x-ray spectra.[86, 46] The spectral width decreases with increasing filter thickness, however the number of photons decreases too, therefore the exposure time needs to increase in order to accumulate more photons. The number of photons used to generate a K-edge subtracted image can be a factor of 55-60 lower than DSA.[13]

In 1997 Zhong et al.[148] used emissions from barium and cerium targets and were successful at imaging stationary objects. However this method was not successful for imaging coronary arteries because of the time required to generate sufficient x-ray exposure levels. The limited number of photons often resulted in incomplete soft-tissue and bone suppression and also reduced iodine signal-to-noise ratio (SNR) compared to DSA.[84, 59, 60, 13, 12] This limits K-edge subtraction to imaging areas where the x-ray beam is projected through a relatively short path.

The problem of soft-tissue and bone suppression was later addressed and a triple energy method was proposed.

1.2.3.3 Triple-energy subtraction angiography

The goal of the triple-energy approach is to suppress both soft-tissue and bone from angiographic images by subtracting three images acquired with x-ray spectra each having different mean energies. Kelcz et al.[59] used a triple-energy approach using three filters and three kV to reduce pixel-intensity variations caused by residual soft-tissue and bone variations. However the required filters need to be thick so that the spectra do not overlap. Kelcz implemented a three-spectrum approach with 46, 54, and 62 kV x-ray spectra

filtered with iodine, cerium, and lead, respectively. While their approach suppressed soft-tissue and bone, the iodine-specific images suffered from severely reduced SNR due to power limitations of x-ray tubes. There were so few photons reaching the x-ray detector that iodine-specific images were severely compromised by noise associated with detector electronics, and the method suffered from other limitations including increase in patient dose, exposure time, and anode heat units.

As the concept of energy-based subtraction evolved, dual-energy approach became a focus of investigation.

1.2.3.4   Dual-energy

The goal of dual-energy approach is to suppress either soft-tissue or bone from angiographic images by subtracting of two images acquired with x-ray spectra having different mean energies. This is most commonly performed using applied tube voltages of 50-70 kV and 120-130 kV for low and high kV spectra, respectively, with 2-2.5 mm of copper filtration on the high kV spectrum.[37, 38, 134, 90, 91, 132, 133, 136, 88] This approach aims to suppress soft-tissue structures because they are the primary surrounding tissue that move like the heart, for example. Since bone is not fully suppressed in these images, early investigators subtracted pre-injection dual-energy images from post-injection dual-energy images to remove overlying bone structures, similar to DSA.[37, 38, 135, 132] Guthaner et al[37, 38] demonstrated that in cooperative patients this approach combines the benefits of bone suppression offered by DSA. Molloi et al[90] who used a dual-energy approach to quantify canine coronary arteries and, while bone was not fully suppressed from images, soft-tissue suppression resulted in superior iodine visualization compared to non-subtraction approaches. Also similar approaches have been useful in quantifying left-ventricular ejection fraction.[91, 135] Dual-energy approaches use much thinner filters than K-edge subtraction and three material compositions, however these early studies suffered from reduced SNR compared to DSA by at least a factor of 2-5. [37, 38, 74, 90, 91]

10

Early investigators used image intensifiers with video cameras.[74, 133, 143, 104, 101, 103] While these technologies were widely used for DSA, they suffered from veiling glare and other limitations that compromised the low-noise linear response required for dual-energy imaging.[111, 112] Even with the introduction of early flat-panel detectors,[258, 5, 104, 113, 27, 26, 109, 103, 100, 6, 124] Molloi et al.[26] showed only modest improvements in dual energy image quality.

1.2.3.5 Approaches to dual-energy

Three approaches to dual-energy imaging have been developed and reported over the years.[114, 5] The first method described requires a single kVp and dual-filtering at the source to generate two different beams, one with mean energy directed towards the kV peak and the other with a mean energy above the k-edge energy of the contrast agent.[114] This approach was not widely accepted because of poor separation of low and high energy spectra. The second approach is one that uses a single exposure where two radiation detectors that have different energy sensitivities separated by a filter are "sandwiched" together . The advantage of this approach is that patient motion misregistration artifacts are reduced and it is therefore a preferred method for detecting small calcified lesions in the lung in chest radiography.[9, 95, 30, 121, 31, 66] However, as with the first method, poor separation of energy spectra results in a grainy image. The third approach requires an x-ray generator to switch between two kilovoltages to produce low and high kV image exposures that are acquired within milliseconds of each other.[114] Despite technical complexity, the rapid kV value change seems to be a viable approach to implementing the dual kV technique for dual-energy subtraction imaging without motion artifacts.[4, 46, 13, 64, 37] Shaw et al[114] compared all three approaches and concluded that two separate kV and mAs exposures acquired a few milliseconds apart has better spectral separation between low and high kV acquisitions and therefore less noise compared to the other two, however implementation of a generator that is capable of fast kV switching

is not trivial. There are other problems that occur generally in a radiography setting with scatter,[76, 14, 54, 32, 55, 131, 116, 50, 68, 77, 149] beam hardening,[75, 76, 14] and read noise.

1.2.3.6   Limitations of early dual-energy studies

Early dual-energy studies had severely reduced SNR compared to DSA and non-subtraction approaches [83, 37, 38, 135, 132, 133, 136, 88] due to the combination of inefficient production of low-energy x-ray spectra and altering of high-energy spectra. In addition, early dual-energy studies were carried out using an image-intensifier-television system that convert x-ray energy to photons with wavelengths in the visible range in combination with a video camera used to detect visible photons. The image-intensifier-television system was limited by veiling glare[111, 112] and detector non-uniformities across the field of view.[16, 34] Cameras used in many of these systems reportedly suffered from substantial read-out lag that decreased the dual-energy iodine signal by 30-50% in some studies.[86, 87, 132, 88] Read-out lag, however, has minimal affect on DSA image signal because mask and contrast exposures are acquired many seconds apart. New flat-panel detectors which have emerged in the past few years do not have these limitations and also provide other advantages not found in image-intensifier-television systems. Namely, they provide high detector quantum efficiency (DQE) and a wider dynamic range.[119] However, one of the remaining limitations of energy subtraction is the increased stochastic noise in the subtracted image. Approaches to reduce dual-energy image noise have been previously reported which use post-processing on the digitally acquired images.[52, 56, 74, 133, 44, 143] These approaches work independent of the hardware used for image acquisition. Complementary improvements in hardware design and technology also serve to improve image quality. Past studies of dynamic dual-energy imaging have made use of x-ray image intensifiers.[89, 90, 132, 133] Advances in detector technology have seen the introduction of digital flat-panel detectors with high DQE, fast-frame readout capabilities and wide dy-

namic range. Molloi et al.[26] compared the dual-energy image quality using a current x-ray image intensifier and a digital flat-panel detector, and found that image quality was similar for the same patient exposure.

1.2.3.7 Current state of dual-energy subtraction angiography

Early dual-energy studies used technology of the time and it is therefore unclear whether reduced image quality was a result of technological limitations or of the fundamental physics. X-ray source and detector technologies have improved substantially over the past three decades and the limitations described above may no longer apply. This suggests that it may be the right time to revisit dual-energy with a focus on the image quality that can be achieved for a given radiation dose to the patient and how this compares to DSA and would it be less insensitive to motion artifacts.

1.3 Research problem

There is reason to believe that dual-energy methods, called energy-subtraction angiography (ESA), can compete directly with DSA to produce high-quality angiographic images for the same patient dose. For example, Tanguay et al.[124] compared image quality between DSA, ESA, and energy-resolving angiography (ERA) using a theoretical model that was validated using a Monte-Carlo simulation for the application of photon-counting methods. They concluded that ESA and ERA (using photon-counting detectors with x-ray spectroscopy capabilities) could produce comparable image quality in terms of the iodine SNR compared to DSA at low iodine concentrations. However, those calculations considered only the fundamental SNR as determined by the physics of x-ray interactions, and were not validated by experiment. These issues lead to the following research questions:

1. What limited ESA in the past? Was it a physical or technical limitation? If it is a technical limitation, can we use new technology to make ESA successful today?

2. Can we use physical parameters to optimize image quality in terms of iodine signal-to-noise ratio for ESA and how does it compare with DSA for the same radiation exposure and iodine mass loading?

3. Can we demonstrate that ESA works in an anthropomorphic phantom? Is the phantom a good representation of a patient?

The questions posed are important because they indicate how much research effort should be invested in developing ESA systems for applications in cardiac imaging. Answering these questions requires a thorough understanding of image formation and material-specific imaging and how various technical and physical processes affect ESA image quality. It will also require understanding of engineering behind the design and implementation of ESA in real-time.

1.3.1 Research objectives

1. To understand iodine signal and noise we will start our investigation by developing a theoretical model to come up with a metric of comparison of iodine SNR using the Rose model between DSA and ESA. We use the Rose model because it describes the minimal SNR required for visual detection of a uniform low-contrast object of area A in a uniform background with stationary noise and it only apply to a phantom with uniform background. We also apply the Rose model to higher concentrations to include signal from thicker iodinated structures such as 1 mm arteries. To check if we did the math correctly, we will validate our theoretical calculations for iodine signal-to-noise ratio for images obtained for DSA and ESA. We can use our theoretical model to compare technical parameters that may have affected ESA in the past.

2. To give a complete description and comparison of visual iodine detection for ESA and DSAwe will extend our Rose model to include noise from iodine in DSA and ESA images (Sum of Variances). We will use both the Rose and SOV theoretical models to optimize ESA and compare the iodine SNR for optimal parameters that the user may control

such as the kVp and the mAs.. We will use a monoenergetic approximation of the iodine SNR to optimize it in terms of the ratio of number of incident photons and relate it to the mAs ratio for our polyenergetic calculation.

3. We will show how well ESA is able to suppress bone in an anthropomorphic phantom (RANDO and DEXA wedges) while preserving iodine signal.

1.4   Thesis outline

The goal of this thesis is addressed in a series of 3 papers (Chapters 2 to 4) that have either been published, submitted for publication, or have been prepared for publication.

1.4.1   Chapter 2: Energy subtraction angiography can compete with digital subtraction angiography in terms of iodine Rose SNR

It is unclear why image quality for ESA was relatively poor compared to DSA in the past despite investigations into image quality of ESA for computed tomography and mammography, and radiography. It is therefore unknown whether dual-energy will generate iodine-specific images with similar image quality relative to DSA for similar patient entrance exposures with current technology that is available. It is difficult to compare both methods without understanding the fundamental iodine signal and noise properties.

Chapter 2 describes a theoretical framework for characterizing image quality and forming a metric of comparison between ESA and DSA. We validated our model by experiment where ESA and DSA images of a vascular phantom were acquired using an x-ray system with a flat panel CsI Xmaru1215CF-MPTM (Rayence Co., Ltd., Republic of Korea) detector. For ESA low and high applied tube voltages of 50 kVp and 120 kVp (2.5 mm-Cu), respectively, and for DSA mask and contrast images the applied tube voltage was 80 kVp. Using iodine-specific images of a stepwedge the iodine signal-to-noise ratio (SNR) per Kinetic Energy Released per unit mass (KERMA) in air was calculated for each iodine mass

loading for both ESA and DSA.

We show similar iodine-specific images for DSA and ESA for similar patient entrance exposures. Our experimental results are in excellent agreement with our theoretical calculations. A 500 μm CsI thickness can increase the iodine SNR per root exposure by 15-30% compared to thinner CsI thicknesses in older detector models. The acceptable read noise for ESA needs to be a factor of 5 lower than DSA and the acceptable scatter-to-primary ratio for ESA needs to be 0.05 in order for ESA to achieve similar iodine SNR per-root air KERMA to DSA. We show experimentally that we can achieve a scatter-to-primary ratio of 0.03-0.05 by increasing the air gap to 30 cm, which is a reasonable air gap used for fluoroscopy.

We conclude that ESA under these conditions is possible and has the potential to produce iodine-specific images similar to DSA for similar patient entrance air KERMA. ESA may potentially be used for background removal in situations where DSA cannot be used such as cardiac imaging.

[This chapter was published as the article "Energy subtraction angiography can compete with digital subtraction angiography in terms of iodine Rose SNR" by Christiane S. Burton, John R. Mayo and I. A. Cunningham, Medical Physics 43(11) 5925-5933 (2016).]

1.4.2 Chapter 3: Optimizing iodine SNR per root air KERMA for energy-subtraction methods

Once the theoretical framework had been established and validated for DSA and ESA iodine SNR we optimized physical parameters to achieve the best possible iodine SNR. A notable optimization study for dual-energy by Van Lysel[133] showed using a trial and error approach that the best results were obtained using a low-energy kV setting of 50 - 55 kV and the highest possible high-kV setting, coupled with a 1.5-2.0 mm beam-hardening filter on the high-energy spectrum to increase spectral separation[60] (minimize overlap). We show in chapter 2 that when scatter and detector read noise are taken into consideration

the iodine SNR for ESA is equal to that of DSA for low iodine mass loadings and for similar patient entrance exposure. Image quality is a combination of physical and technical parameters, therefore it is still unknown whether dual-energy is also limited by physical parameters.

In Chapter 2 we demonstrated that energy subtraction angiography under special and practical circumstances has similar iodine signal-to-noise ratio (SNR) for similar patient entrance air KERMA compared to digital subtraction angiography, the reference standard. However, the parameters used to achieve an iodine SNR were for a single technique and may have been sub-optimal, and therefore it is necessary to perform an optimization study. Image optimization can be determined by the mAs ratio in both the high and low kV beam for a fixed entrance exposure. In this paper the authors show mAs ratios that will yield optimal or near optimal (within 10% of optimal) iodine SNR per root air KERMA for ESA. Iodine SNR per root patient entrance air KERMA was optimized with respect to the mAs ratio (low/high) kV exposure. The mAs ratio is optimized for ESA by varying the ratio between the low and high mAs for three different water thicknesses and kVps of 50, 60, and 70 kV. The low kV of 50 kVp and a copper filter thickness of 2.5 mm for high kVp of 120 kV will yield the best possible iodine SNR per root air KERMA compared to 60 and 70 kVp. For ESA to translate to the clinic we looked at the iodine SNR for detector materials that are commercially available such as CsI, Gd_2O_3, and Se for material thicknesses of 0.4, 0.4, and 0.1 mm. We concluded that for ESA, techniques of 50 kV and 120 kV (2.5 mm copper) ESA should use an mAs ratio of 1.0, for 60 kV the optimal mAs ratio is 0.5, and for 70 kV the mAs ratio should be 0.3 for all patient thicknesses. The issue of heat loading may be overcome with use of a fast kVp-switching x-ray machine so that fewer images may be acquired.

[This chapter consists of the manuscript "Optimizing iodine SNR per root air KERMA for energy-subtraction methods" by Christiane S. Burton, John R. Mayo and I. A. Cunningham, being submitted for consideration for publication by Medical Physics.]

1.4.3 Chapter 4: Residual bone signal for dual-energy subtraction angiography

Once we discover what combined parameters will give optimal or near-optimal iodine SNR, the next step is to look at how well our dual-energy method works in an anthropomorphic phantom. A key study by Liu et al.[229] looked at dual-energy for a three material decomposition where they used mass conservation to express the third material in terms of total mass and found that the three material decomposition produced more accurate Hounsfield units for CT compared to a two-material decomposition for a three-material composition. Other studies looked at differentiating iodine from other material such as calcified plaque in the arteries in CT.[53, 36, 127, 24, 173, 178, 57, 125, 110, 79, 96] Van Lysel[135] has also shown that bone may be partially suppressed in dual-energy images. However, little has been done to address removing bone for dual-energy for a three material composition of iodine, water, and bone. The purpose of this study is to show what parameters are needed for suppressing bone from a dual-energy image and show the effect bone suppression has on the iodine signal.

We use two phantoms to demonstrate the effect of bone removal for iodine signal. The first phantom used for this study consists of iodinated stepwedge submerged in 20 cm thickness of water and bone-mimicking DEXA wedge material (SB3; Gammex-RMI, Middleton, WI, U.S.A.)[35, 45, 77, 33] that is attached to the outside surface of the tank. We acquired images of the iodine stepwedge and DEXA wedge together, and we took images of each wedge separately to calculate the transmission factor of iodine and DEXA material for each thickness. The second phantom consists of RANDO anthropomorphic vascular phantom,[2] a thin 2 cm thickness tank of water, and water-equivalent iodine-filled tubing submerged in the thin tank of water placed right up against the back of the RANDO phantom. In both cases we used a 30 cm air gap from Chapter 2 between the surface of the phantom and the surface of the detector. We used a very-low noise CsI/CMOS detector (Xmaru1215CF-MPTM, Rayence Co., Ltd., Korea) with square 49.5 μm elements

and 0.5 mm CsI. ESA images were acquired using a fast kV-switching generator (EMD Technologies, Montreal Canada) operating in single-exposure mode with several seconds between high and low-energy exposures. The ESA images were acquired using low kV of 50, 60, and 70 kV and a fixed high kV of 120 kV with 2.5 mm of copper filtration. We assessed whether the tubing used is water equivalent or not by filling the tube with water, then submerging the tube in water and acquiring images of the tubing at 50, 80 and 120 kV. We excluded the tubing that was visible compared to the background in the image. We attached small lead pieces to the end of each tube. For the tubes that we could not see we took an image profile in the x-direction of the image near the lead strip and plot it against the pixel values of the image. We used Amber Natural Latex Tubing with 1/8" inner diameter (I. D.) and wall thickness of 1/32".

In this study we show that soft-tissue suppression will preserve the iodine signal while weighting to remove cortical bone will suppress the thin DEXA steps only and increase image noise. Removing soft-tissue rather than bone would be better for iodine signal. We also show the with RANDO phantom that different weights affect how well iodine and bone-mimicking material can be visually seen in the image. With a weight of 0.2 the iodine signal appears to be completely suppressed along with the bone-mimicking material, but as the weight increases both iodine and bone signal appear in the image. Weights of 0.5 and 0.55 preserve the iodine signal and show better suppression of bone compared to images with weights of 0.6 and 0.8. We suggest that for 60 and 120 kV that a weight of 0.5 or 0.55 be used for imaging a three material composition. We show the benefits of dual-energy imaging compared to a single kV image of the RANDO vascular phantom where in the single kV image the iodine signal shows little contrast to the background.

We show that when using bone weighted ESA images the iodine signal decreases compared to soft-tissue subtraction. We show that iodine signal is very low with DEXA wedge signal cancellation for thin DEXA wedge thicknesses of 0.1 and 0.4 cm, and in practice we show that these ESA images will appear quite noisy compared to soft-tissue weighted ESA

images. We show that with an anthropomorphic phantom that ESA better removes soft-tissue and partially removes bone-mimicking material compared to conventional single kV image.

We conclude that soft-tissue weighted imaging is optimal for preserving iodine signal, partial bone removal (particularly thin bone), and ESA image noise. For 60 and 120 kV the weight needed to preserve iodine and partially suppress bone-mimicking material the best is between 0.5 and 0.55. We conclude that for a 3 material composition of iodine, water, and bone, water is the material that needs to be removed. In a future study we plan to consider addressing performing ESA in real-time similar to fluoroscopy for cardiac imaging.

[This chapter is a draft manuscript of an article to be submitted for publication "Bone removal for dual-energy subtraction angiography" by Christiane S. Burton, John R. Mayo and I. A. Cunningham.]

1.4.4   Goals and objectives

Image quality is determined by a combination of many physical and technical parameters. In this thesis we examine the fundamental signal and noise characteristics that can be achieved using both energy-based subtraction and DSA methods for the similar patient entrance exposures. Results are validated experimentally in a phantom study and the technical parameters required to achieve near ideal image quality are identified. It is shown that under many situations of practical importance, ESA can have image quality that compares favourably with DSA.

1.5   References

[1] H. L. Abrams. History of cardiac radiology. *American Journal of Roentgenology*, 167(2):431–438, 1996.

[2] S. W. Alderson. Method and apparatus for accurate radiation dosage control in breast cancer treatment. *Official Gazette of the United States Patent & Trademark Office Patents*, 1211(4):3858, 1998.

[3] G. Alleyne, R. Beaglegole, D. Bramley, J. Carrington, R. Chowdhury, M. Engelgau, M. Ezzati, C. Foster, O. Franco, V. Fuster, G. Gartlehner, D. Goodarz, V. Grabauskas, I. Graham, M. Hassan, J. Harold, C. Hawkes, C. Heneghan, K. Kotenko, L. Li, A. Lopez, G. Masset, J.-C. Mbanya, G. Mensah, R. Moodie, V. Narayan, S. Nishtar, S. Reddy, J. Rehm, M. Rayner, P. Scarborough, Y. Seedat, S. Shastri, P. Shetty, S. Smith, I. Sommer, L. Sperling, D. Stuckler, D. Webb, K. Wickramasinghe, D. Wood, Q. Youlin, and S. Yusuf. *Global Status Report on Noncommunicable Diseases 2014*. World Health Organization, Geneva, 2014.

[4] R. E. Alvarez and A. Macovski. Energy-selective reconstructions in x-ray computerized tomography. *Physics of Medicine and Biology*, 21(5):733–744, 1976.

[5] R. E. Alvarez, J. A. Seibert, and S. K. Thompson. Comparison of dual energy detector system performance. *Medical Physics*, 31(3):556–566, 2004.

[6] Robert E. Alvarez. Near optimal energy selective x-ray imaging system performance with simple detectors. *Medical Physics*, 37(2):822–841, 2010.

[7] A. Alwan, T. Armstrong, D. Bettcher, T. Boerma, F. Branca, J. C. Y. Ho, C. Mathers, R. Martinez, V. Poznyak, G. Roglic, L. Riley, E. d'Espaignet, G. Stevens, K. Taubert, and G. Xuereb. *Global atlas on cardiovascular disease prevention and control 2011*. World Health Organization, Geneva, 2011.

[8] M. Anthea, L. Roshan, J. Hopkins, C. W. McLaughlin, S. Johnson, M. Q. Warner, D. LaHart, and J. D. Wright. *Human Biology and Health*. Pearson Prentice Hall; 3 edition, 1997.

[9] G. T. Barnes, R. A. Sones, M. M. Tesic, D. R. Morgan, and J. N. Sanders. Detector for dual-energy digital radiography. *Radiology*, 156(2):537–540, 1985.

[10] Y. Bentoutou, N. Taleb, M. C. El Mezouar, M. Taleb, and L. Jetto. An invariant approach for image registration in digital subtraction angiography. *Pattern Recognition*, 35(12):2853– 2865, 2001.

[11] G. E. Berrios. The origins of psychosurgery: Shaw, burckhardt and moniz. *History of Psychiatry*, 8(1):61–81, 1997.

[12] W. R. Brody. Digital subtraction angiography. *Institute of Electrical and Electronics Engineers Transactions on Nuclear Science*, 29(3):1176–1180, 1982.

[13] W. R. Brody, G. Butt, A. Hall, and A. Macovski. A method for selective tissue and bone visualization using dual energy scanned projection radiography. *Med. Phys.*, 8(3):353–357, 1981.

[14] R. A. Brooks and G. Di Chiro. Beam hardening in x-ray reconstructive tomography. *Physics Medical Biology*, 21(3):390–398, 1976.

[15] Statistics Canada. *Mortality, summary list of causes 2008.* Statistics Canada, 2011.

[16] D. P. Chakraborty. Image intensifier distortion correction. *Medical Physics*, 14(2):249–252, 1987.

[17] W. A. Chilcote, M. T. Modic, W. A. Pavlicek, J. R. Little, A. J. Furian, P. M. Duchesneau, and M. A. Weinstein. Digital subtraction angiography of the carotid arteries: A comparative study in 100 patients. *Radiology*, 139(2):287–295, 1981.

[18] G. L. Clark, W. M. Duane, and W. W. Stirler. The secondary and tertiary rays from chemical elements of small atomic number due to primary x-rays from a molybdenum target. *Proceedings of the National Academy of Sciences*, 10(4):148–152, 1924.

[19] A. Cournand. Cardiac catheterization; development of the technique, its contributions to experimental medicine, and its initial applications in man. *Acta Medical Scandinavia Supplier*, 579:3–32, 1975.

[20] G. S. Cox and G. de Jager. Automatic registration of temporal image pairs for digital subtraction angiography. *Society of Photographic Instrumentation Engineers*, 2167:188–199, 1994.

[21] I. A. Cunningham and R. Shaw. Signal-to-noise optimization of medical imaging systems. *J. Opt. Soc. Am. A*, 16(3):621–632, 1999.

[22] G. T. Barnes D. M. Tucker and D. P. Chakraborty. Semiempirical model for generating tungsten target x-ray spectra. *Medical Physics*, 18(2):211–218, 1991.

[23] P. Dawson. Digital subtraction angiography: A critical analysis. *Clinical Radiology*, 39(5):474–477, 1988.

[24] K. Deng, C. Liu, R. Ma, C. Sun, X.-m. Wang, Z.-t. Ma, and X. I. Sun. Dual-energy direct bone removal ct angiography for evaluation of intracranial aneurysm or stenosis: comparison with conventional digital subtraction angiography. *Clin. Radiol.*, 64(5):534–541, 2009.

[25] C. T. Dotter and L. H. Frische. Visualization of the coronary circulation by occlusion aortography: a practical method. *Radiology*, 71(4):502–524, 1958.

[26] J. L Ducote, X. Tong, and S. Molloi. Dual-energy cardiac imaging: an image quality and dose comparison for a flat-panel detector and x-ray image intensifier. *Physics in Medicine and Biology*, 52(1):183–196, 2007.

[27] J. L. Ducote, T. Xu, and S. Molloi. 2007. *Physics in Medicine and Biology*, 52:183–196, 2007.

[28] H. W. Fischer and K. R. Thomson. Contrast media in coronary angiography: A review. *Investigation Radiology*, 13(5):450–459, 1978.

[29] W. Forssmann. Sondierung des rechten herzens. *Klin Wochenschr*, 8:2085, 1929.

[30] R. G. Fraser, C. Sanders, G. T. Barnes, H. MacMahon, M. L. Giger, K. Doi, A. W. Templeton, G. G. Cox, S. J. Dwyer, and C. R. Merritt. Digital imaging of the chest. *Radiology*, 171(2):297–307, 1989.

[31] D. M. Gauntt and G. T. Barnes. X-ray tube potential, filtration, and detector considerations in dual-energy chest radiography. *Medical Physics*, 21(2):203–218, 1994.

[32] G. H. Glover. Compton scatter effects in ct reconstructions. *Medical Physics*, 9(6):860–867, 1982.

[33] P. V. Granton, C. J. D. Norley, J. Umoh, E. A. Turley, B. C. Frier, E. G. Noble, and D. W. Holdsworth. Rapid in vivo whole body composition of rats using cone beam ct. *J. Appl. Physiol.*, 109(4):1162–1169, 2010.

[34] E. Gronenschild. The accuracy and reproducibility of a global method to correct for geometric image distortion in the x-ray imaging chain. *Med. Phys.*, 24(12):1875–1888, 1997.

[35] M. Gulam, M. M. Thornton, A. B. Hodsman, and D. W. Holdsworth. Bone mineral measurement of phalanges: Comparison of radiographic absorptiometry and area dual x-ray absorptiometry. *Radiology*, 216(2):586–591, 2000.

[36] R. G. Gupta, M. P. Catherine, C. Leidecker, T. J. Brady, J. A. Hirsch, R. G. Nogueira, and A. J. Yoo. Evaluation of dual-energy ct for differentiating intracerebral hemorrhage from iodinated contrast material staining. *Radiology*, 257(1):205–211, 2007.

[37] D. F. Guthaner, W. R. Brody, B. D. Lewis, G. S. Keyes, and B. F. Belanger. Clinical application of hybrid subtraction digital angiography:preliminary results. *Cardiovascular Interventional Radiology*, 6(4):290–294, 1983.

[38] D. F. Guthaner, L. Wexler, D. R. Enzmann, S. J. Riederer, G. S. Keyes, W. F. Collins, and W. R. Brody. Evaluation of peripheral vascular disease using digital subtraction angiography. *Radiology*, 147(2):393–398, 1983.

[39] Health and Stroke Foundation. 2015 report on the health of canadians. Report, February 2015.

[40] D. Healy, T. Olson, and J. Weaver. Reduced motion artifacts in medical imaging by adaptive spatio-temporal reconstruction. *Numerical Algorithms*, 9(1):55–84, 1995.

[41] R. Herzig, S. Burval, B. Krupka, I. Vlachova, K. Urbaneka, and J. Mares. Comparison of ultrasonography, ct angiography, and digital subtraction angiography in severe carotid stenoses. *Eur. J. Neurol.*, 11(11):774–781, 2004.

[42] C. B. Higgins. Effect of contrast materials on left ventricular function. *Investigation Radiology*, 15(6):S220–S231, 1980.

[43] C. B. Higgins, K. H. Gerber, R. F. Mattrey, and R. A. Slutsky. Evaluation of the hemodynamic effects of intravenous administration of ionic and nonionic contrast materials. implications for deriving physiologic measurements from computed tomography and digital cardiovascular imaging. *Radiology*, 142(3):681–686, 1982.

[44] D. A. Hinshaw and J. T. Dobbins. Recent progress in noise reduction and scatter correction in dual-energy imaging. *Society of Photographic Instrumentation Engineers Medical Imaging*, 2432(134):134–42, 1995.

[45] D. W. Holdsworth, M. M. Thorton, D. Drost, P. H. Watson, L. J. Fraher, and A. B. Hodsman. Rapid small-animal dual-energy x-ray absorptiometry using digital radiography. *Journal of Bone and Mineral Research*, 15(12):2451–2457, 2000.

[46] T. L. Houk, R. A. Kruger, C. A. Mistretta, S. J. Riederer, C. G. Shaw, J. C. Lancaster, and D. C. Flemming. Real-time digital k-edge subtraction fluoroscopy. *Investigation Radiology*, 14(4):270–278, 1979.

[47] P. Hua and I. Fram. Feature-basedimage registration for digital subtraction angiography. *Society of Photographic Instrumentation Engineers*, 1898:24–31, 1993.

[48] J. W. Hurst. Naming of the waves in the ecg, with a brief account of their genesis. *Circulation*, 98(18):1937–1942, 1998.

[49] B. Jacobson. Dichromatic absorption radiography. *Acta Radiologica*, 39(6):437–452, 1953.

[50] G. Jarry, S. A. Graham, D. J. Moseley, D. J. Jaffray, J. H. Siewerdsen, and F. Verhaegen. Characterization of scattered radiation in kv cbct images using monte carlo simulations. *Medical Physics*, 33(11):4320–4329, 2006.

[51] Francois Nicolas Bernhart Claus Jianguo Zhao John M. Sabol, Gopal B. Avinash and James T. Dobbins. The development and characterization of a dual-energy subtraction imaging system for chest radiography based on csi:ti amorphous silicon flat-panel technology. *SPIE.Medical Imaging*, 4320:399–409, 2001.

[52] P.C. Johns, D. J. Drost, M. J. Yaffe, and A. Fenster. Dual-energy mammography: initial experimental results. *Medical Physics*, 3(3):297–304, 1985.

[53] T. R. C. Johnson, B. Krauss, M. Sedlmair, M. Grasruck, H. Bruder, D. Morhard, C. Fink, S. Weekbach, M. Lenhard, B. Schmidt, T. Flohr, M. F. Reiser, and C. R.

Becker. Material differentiation by dual energy ct: initial experience. *Eur. Radiol.*, 17(6):1510–1517, 2007.

[54] P. M. Joseph and R. D. Spital. A method for correcting bone induced artifacts in ct scanners. *Journal of Computational Assisted Tomography*, 2(2):100–108, 1978.

[55] P. M. Joseph and R. D. Spital. The effects of scatter in x-ray computed tomography. *Med. Phys.*, 9(4):464–472, 1982.

[56] W.A. Kalender. An algorithm for noise suppression in dual energy ct material density images. *Institute of Electrical and Electronics Engineers Transactions on Medical Imaging*, 7(3):218 – 224, 1988.

[57] M.-J. Kang, C. M. Park, C. H. Lee, J. M. Goo, and H. J. Lee. A flexible method for multi-material decomposition of dual-energy ct images. *RadioGraphics*, 30(3):2022–2035, 2010.

[58] B. T. Katzen. Current status of digital angiography in vascular imaging. *Radiology Clinic of North America*, 33(1):1–14, 1995.

[59] F. Kelcz. Absorption-edge fluoroscopy using a three-spectrum technique. *Medical Physics*, 3(3):159–168, 1976.

[60] F. Kelcz, C. A. Mistretta, and S. J. Riederer. Spectral considerations for absorption-edge fluoroscopy. *Medical Physics*, 4(1):26–35, 1977.

[61] Andoh K Kinno Y, Odagiri K. Gadopentetate dimeglumine as an alternative contrast material for use in angiography. *Am J Radiol*, 160:1293–1294, 1993.

[62] R. A. Kruger. Estimation of the diameter of and iodine concentration within blood vessels using digital radiography devices. *Med. Phys.*, 8(5):652–658, 1981.

[63] R. A. Kruger, S. J. Riederer, and C. A. Mistretta. Relative properties of tomography, k-edge imaging, and k-edge tomography. *Med Phys*, 4(3):244–249, 1977.

[64] L. A. Lehmann, R. E. Alvarez, A. Marcovski, W. R. Brody, N. J. Pelc, S. J. Riederer, and A. L. Hall. Generalized image combinations in dual kvp digital radiography. *Med. Phys.*, 8(5):659–667, 1981.

[65] D. C. Levin, R. M. Schapiro, L. M. Boxt, L. Dunham, D. P. Harrington, and D. L. Ergun. Digital subtraction angiography: Principles and pitfalls of image improvement techniques. *American Journal of Roentgenology*, 143(3):447–454, 1984.

[66] F. Li, R. Engelmann, K. Doi, and H. MacMahon. Improved detection of small lung cancers with dual-energy subtraction chest radiography. *American Journal of Roentgenology*, 190(4):886–891, 2009.

[67] X. Liu, L. Yu, A. N. Primak, and C. H. McCollough. Quantitative imaging of element composition and mass fraction using dual-energy ct: Three-material decomposition. *Med. Phys.*, 35(5):1602–1609, 2009.

[68] J. S. Maltz, B. Gangadharan, S. Bose, D. H. Hristov, B. A. Faddegon, and A. Paidi. Algorithm for x-ray scatter, beam-hardening, and beam profile correction in diagnostic (kilovoltage) and treatment (megavoltage) cone beam ct. *Institute of Electrical and Electronics Engineers Translation Medical Imaging*, 27(12):1791–1810, 2008.

[69] G. B. Mancini, J. N. Bloomquist, V. Bhargava, J. B. Stein, W. Lew, R. A. Slutsky, R. Shabetai, and C. B. Higgins. Hemodynamic and electrocardiographic effects in man of a new nonionic contrast agent (iohexol): Advantages over standard ionic agents. *American Journal Cardiology*, 51(7):1218–1222, 1983.

[70] G. B. Mancini and C. B. Higgins. Digital subtraction angiography: A review of cardiac applications. *Progressive Cardiovascular Disease*, 28(2):111–141, 1985.

[71] V. R. Mandava, J. M. Fitzpatrick, and D. R. Pickens. Adaptive search space scaling in digital image registration. *Medical Imaging*, 8(3):251–262, 1989.

[72] D. L. Mann, D. P. Zipes, P. Libby, and R. O. Bonow. *Heart Disease: A Textbook of Cardiovascular Medicine*. Philadelphia, W.B. Saunders Co., 1997.

[73] C. D. Mathers and D. Loncar. Projections of global mortality and burden of disease from 2002 to 2030. *Public Library of Science Medicine*, 3(11):442, 2006.

[74] C. H. McCollough, M. S. Van Lysel, W. W. Peppler, and C. A. Mistretta. A correlated noise reduction algorithm for dual-energy digital subtraction angiography. *Med. Phys.*, 16(6):873–880, 1989.

[75] E. C. McCollough, J. L. Baker, O. W. Houser, and D. F. Reese. An evaluation of the quantitative and radiation features of a scanning x-ray transverse axial tomograph: the emi scanner. *Radiology*, 111(3):709–715, 1974.

[76] W. D. McDavid, R. G. Waggener, W. H. Payne, and M. J. Dennis. Spectral effects on three-dimensional reconstruction from x-rays. *Med. Phys.*, 2(6):321–324, 1975.

[77] J. A. Meganck, K. M. Kozloff, M. M. Thornton, S. M. Broski, and S. A. Goldstein. Beam hardening artifacts in micro-computed tomography scanning can be reduced by x-ray beam filtration and the resulting images can be used to accurately measure BMD. *Bone*, 45(6):1104–1116, 2009.

[78] E. H. W. Meijering, K. J. Zuiderveld, and M. A. Viergever. Image registration for digital subtraction angiography. *International Journal of Computer Vision*, 31(2):227–246, 1999.

[79] P. R. Mendonca, P. Lamb, and D. V. Sahani. A flexible method for multi-material decomposition of dual-energy ct images. *IEEE Trans. Med. Imaging.*, 33(1):99–116, 2014.

[80] C. A. Mistretta. X-ray image intensifiers. *AAPM No 3 The physics of medical imaging: recording system measurements and techniques (American Institute of Physics, 1979)*, pages 182–205, 1979.

[81] C A Mistretta and A. B. Crummy. Diagnosis of cardiovascular disease by digital subtraction angiography. *Science*, 214(4522):761–765, 1981.

[82] C. A. Mistretta and A. B. Crummy. Basic concepts of digital angiography. *Progressive Cardiovascular Disease*, 28(4):245–255, 1986.

[83] C. A. Mistretta, A. B. Crummy, and C. M. Strother. Digital angiography: a perspective. *Radiology*, 139(2):273–276, 1981.

[84] C. A. Mistretta, F. Kelcz, M. G. Ort, M. P. Siedband, J. R. Cameron, A. B. Crummy, and R. E. Polcyn. Absorption edge fluoroscopy. *Institute of Electrical and Electronics Engineers Translation Nuclear Science*, 21(1):645–651, 1974.

[85] C. A. Mistretta, M. G. Ort, J. R. Cameron, A. B. Crummy, and P. R. Moran. A multiple image subtraction technique for enhancing low contrast, periodic objects. *Investigation Radiology*, 8(1):43–49, 1973.

[86] C. A. Mistretta, M. G. Ort, F. Kelcz, J. R. Cameron, M. P. Siedband, and A. B. Crummy. Absorption edge fluoroscopy using quasi-monoenergetic x-ray beams. *Investigation Radiology*, 6(6):402–412, 1973.

[87] C. A. Mistretta, W. W. Peppler, M. Van Lysel, J. Dobbins, B. Hasegawa, P. D. Myerowitz, D. Swanson, C. S. Lee, N. Shaik, and W. Zarnstorff. Recent advances in digital radiography. *Annual Radiology (Paris)*, 26(7):537–542, 1983.

[88] S. Molloi, A. Ersahin, and Y. J. Qian. CCD camera for dual-energy digital subtraction angiography. *nstitute of Electrical and Electronics Engineers Transactions on Medical Imaging*, 14(4):747–752, 1995.

[89] S. Y. Molloi and C. A. Mistretta. Scatter-glare corrections in quantitative dual-energy fluoroscopy. *Med Phys*, 15(3):289–297, 1988.

[90] S. Y. Molloi and C. A. Mistretta. Quantification techniques for dual-energy cardiac imaging. *Medical Physics*, 16(2):209–217, 1989.

[91] S. Y. Molloi, D. M. Weber, W. W. Peppler, J. D. Folts, and C. A. Mistretta. Quantitative dual-energy coronary arteriography. *Investigation Radiology*, 25(8):908–914, 1990.

[92] Mortality and Causes of Death. Global, regional, and national age-sex specific all-cause and cause-specific mortality for 240 causes of death, 1990-2013: a systematic analysis for the global burden of disease study 2013. *Lancet*, 385(9963):117–171, 2013.

[93] R. L. Mueller and T. A. Sanborn. The history of interventional cardiology: cardiac catheterization, angioplasty, and related interventions. *American Heart Journal*, 129(1):146–172, 1995.

[94] M. Nejati, S. Sadri, and R. Amirfattahi. Nonrigid image registration in digital subtraction angiography using multilevel b-spline. *Biomedical Research International*, 2013(236315):1–12, 2013.

[95] L. T. Niklason, N. M. Hickey, D. P. Chakraborty, E. A. Sabbagh, M. V. Yester, R. G. Fraser, and G. T. Barnes. Simulated pulmonary nodules: detection with dual-energy digital versus conventional radiography. *Radiology*, 160(3):589–593, 1986.

[96] T. Niu, X. Dong, M. Petrongolo, and Z. Lei. Iterative image-domain decomposition for dual-energy ct. *Med. Phys.*, 41(4):1–11, 2014.

[97] A. K. Abu-Alfa P. Kuo, E. Kanal. Contrast agents and nephrogenic systemic fibrosis. *Radiology*, 242:647–649, 2007.

[98] Y.-S. Park and J.-T. Kwon. Recurrent cerebral arteriovenous malformation in a child : Case report and review of the literature. *The Korean Neurosurgical Society*, 45(6):401–404, 2009.

[99] F. Pomposelli. Arterial imaging in patients with lower extremity ischemia and diabetes mellitus. *Journal Vascular Surgery*, 52(3):81–91, 2010.

[100] Ricarda Rühl, Magdalena M. Wozniak, Michael Werk, François Laurent, Georg Mager, Michel Montaudon, Andreas Pattermann, Antoine Scherrer, Jean-Pierre Tasu, Maciej Pech, and Jens Ricke. Csi-detector-based dual-exposure dual energy in chest radiography for lung nodule detection: results of an international multicenter trial. *Eur Radiol*, 18(10):1831–1839, 2008.

[101] S. Richard and J. H. Siewerdsen. Optimization of dual-energy imaging systems using generalized neq and imaging task. *Med Phys*, 34(1):127–139, 2007.

[102] S. Richard and J. H. Siewerdsen. Optimization of dual-energy imaging systems using generalized neq and imaging task. *Medical Physics*, 31(1):127–139, 2007.

[103] S. Richard, J. H. Siewerdsen, and D. J. Tward. NEQ and task in dual-energy imaging: From cascaded systems analysis to human observer performance. *Society of Photographic Instrumentation Engineers medical imaging*, 6913(11):1–12, 2008.

[104] Siewerdsen JH. Richard S. Cascaded systems analysis of noise reduction algorithms in dual-energy imaging. *Med Phys*, 35(2):586–601, 2005.

[105] S. J. Riederer and C. A. Mistretta. Selective iodine imaging using k-edge energies in computerized x-ray tomography. *Med Phys*, 4(6):474–481, 1977.

[106] M. Rivera-Ruiz, C. Cajavilca, and J. Varon. Einthoven's string galvanometer: The first electrocardiograph. *Texas Heart Institute journal / from the Texas Heart Institute of St. Luke's Episcopal Hospital, Texas Children's Hospital*, 35(2):174–178, 1927.

[107] E. Roessl and R. Proksa. K-edge imaging in x-ray computed tomography using multi-bin photon counting detectors. *Physics Medical Biology*, 52(15):4679–4696, 2007.

[108] H. Sakuma. Coronary CT versus MR angiography: The role of MR angiography. *Radiology*, 258(2):340–349, 2011.

[109] Jeffrey H. Siewerdsen Samuel Richard and Daniel J. Tward. Neq and task in dual-energy imaging: From cascaded systems analysis to human observer performance. *SPIE*, 6913(691311-1):1–12, 2008.

[110] B. Schulz, K. Kuehling, W. Kromen, P. Siebenhandl, M. J. Kerl, T. J. Vogl, and R. Bauer. Automatic bone removal technique in whole-body dual-energy ct angiography: performance and image quality. *Am. J. Roentgenology*, 199(5):W646–650, 2012.

[111] A. J. Seibert. Characterization of the veiling glare psf in x-ray image intensified fluoroscopy. *Medical Physics*, 11(2):172–179, 1984.

[112] A. J. Seibert. Removal of image intensifier veiling glare by mathematical deconvolution techniques. *Medical Physics*, 12(3):281–288, 1985.

[113] Anthony J Seibert. Flat-panel detectors: how much better are they? *Pediatr Radiol*, 36(2):173–181, 2006.

[114] C. C. Shaw and D. Gur. Comparison of three different techniques for dual-energy subtraction imaging in digital radiography: A signal-to-noise analysis. *Journal of Digital Imaging*, 5(4):262–270, 1992.

[115] J. A. Sicard and G. Forestier. Intravasculature injections of iodine in radiology. *Comptes Rendus des Seances de la Societe de Biologie et des ses Filiales (Paris)*, 88:1200, 1923.

[116] J. H. Siewerdsen, D. J. Moseley, B. Bakhtiar, S. Richard, and D. A. Jaffray. The influence of antiscatter grids on soft-tissue detectability in cone-beam ct with flat-panel detectors. *Medical Physics*, 31(12):3506–3520, 2004.

[117] W. H. Sommer, T. R. Johnson, C. R. Becker, E. Arnoldi, H. Kramer, M. F. Reiser, and K. Nikolau. The value of dual-energy bone removal in maximum intensity projections of lower extremity computed tomography angiography. *Invest. Radiol.*, 44(5):285–292, 2009.

[118] F. M. Sones and E. K. Shirey. Cine coronary arteriography. *Modern concepts of cardiovascular disease*, 31:735–8, 1962.

[119] M. Spahn. Flat detectors and their clinical applications. *European Radiology*, 15(9):1934–1947, 2005.

[120] M. Spahn, V. Heer, and R. Freytag. Flat-panel detectors in x-ray systems. *Radiologe*, 43(5):340–350, 2003.

[121] B. K. Stewart and H. K. Huang. Single-exposure dual-energy computed radiography. *Medical Physics*, 17(5):866–875, 1990.

[122] P. Dawson. T. Albrecht. Gadolinium-dtpa as x-ray contrast medium in clinical studies. *Br J Radiol*, 73:878–882, 2000.

[123] T. Y. Tang, J. M. U-King-Im, S. R. Walsh, V. E. Young, U. Sadat, Z. Y. Li, A. J. Patterson, K. Varty, and J. H. Gillard. Invasive and non-invasive modalities of imaging carotid stenosis. *Journal Cardiovascular Surgery (Torino)*, 50:715–725, 2009.

[124] J. Tanguay, H. K. Kim, and I. A. Cunningham. A theoretical comparison of x-ray angiographic image quality using energy-dependent and conventional subtraction methods. *Medical Physics*, 39(1):132–142, 2012.

[125] C. Thomas, A. Korn, B. Krauss, D. Ketelsen, I. Tsiflikas, H. Brodoefel, C. D. Claussen, A. F. Kopp, U. Ernemann, and M. Heuschmid. Automatic bone and plaque removal using dual energy ct for head and neck angiography: Feasibility and initial performance evaluation. *Eur. J. Radiol.*, 76(1):61–67, 2010.

[126] S. K. Thompson, L. M. Boxt, and S. Abbara. *Cardiac Imaging*, volume 3. Mosby Inc. an affiliate of Elsevier Inc., 2009.

[127] D. N. Tran, M. Straka, J. E. Roos, S. Napel, and D. Fleischmann. Dual-energy ct discrimination of iodine and calcium. *Acad Radiol.*, 16(2):160–171, 2009.

[128] P. A. Turski, W. J. Zwiebel, C. M. Strother, A. B. Crummy, G. G. Celesia, and J. F. Sackett. Limitations of intravenous digital subtraction angiography. *AJNR Am. J. Neuroradiol.*, 4(3):271–273, 1983.

[129] PhD Barbara Elmståhl-MD Peter Leander MD PhD Mats Nilsson PhD Klaes Golman PhD Torsten AlmeŽn MD PhD Ulf Nyman, MD. Are gadolinium-based contrast media really safer than iodinated media for digital subtraction angiography in patients with azotemia? *Radiology*, 223:311–318, 2002.

[130] J. A. Clanton V. M. Runge, R. G. Stewart. Work in progress: potential oral and intravenous paramagnetic nmr contrast agents. *Radiology*, 147:789–791, 1983.

[131] E. Van deCasteele, D. Van Dyck, J. Sijbers, and E. Raman. An energy-based beam hardening model in tomography. *Physics Medical Biology*, 47(23):4181–4190, 2002.

[132] M. S. Van Lysel. Limitations of the lead oxide vidicon for dual-energy digital subtraction angiography. *Institute of Electrical and Electronics Engineers Transaction Medical Imaging*, 10(4):530–537, 1991.

[133] M. S. Van Lysel. Optimization of beam parameters for dual-energy digital subtraction angiography. *Medical Physics*, 21(2):219–226, 1994.

[134] M. S. Van Lysel, J. T. Dobbins, W. W. Peppler, B. H. Hasegawa, C. S. Lee, C. A. Mistretta, W. C. Zarnstorff, A. B. Crummy, W. Kubal, B. Bergsjordet, C. M. Strother, and J. F. Sackett. Work in progress: hybrid temporal-energy subtraction in digital fluoroscopy. *Radiology*, 147(3):869–874, 1983.

[135] M. S. Van Lysel, W. P. Miller, D. G. Senior, V. K. Gupta, D. J. Ende, and D. J. Albright. Left ventricular dual-energy digital subtraction angiography: A motion immune digital subtraction technique. *Medical Physics*, 7(1):55–65, 1991.

[136] M.S. Van Lysel, W. P. Miller, T. P. Fuerst, and D. J. Albright. Improved densitometric measurement of left ventricular ejection fraction using dual-energy digital subtraction angiography. *Int. J. Card. Imaging*, 10(2):113–121, 1994.

[137] L. Van Tran and J. Sklansky. Flexible mask subtraction for digital angiography. *Institute of Electrical and Electronics Engineers Transaction Medical Imaging*, 11(3):407–415, 1992.

[138] A. Venot, J. L. Golmard, J. F. Lebruchec, L. Pronzato, E. Walter, G. Frij, and J. C. Roucayrol. Digital methods for change detection in medical images. *Information Processing in Medical Imaging*, 28:1–16, 1984b.

[139] A. Venot, J. F. Lebruchec, and J. C. Roucayrol. A new class of similarity measures for robust image registration. *Computer Vision Graphic Image Processor*, 28:176–184, 1984.

[140] A. Venot and V. Leclerc. Automatedcorrection of patient motion andgray values prior to subtraction in digitizedangiography,. *Institute of Electrical and Electronics Engineers Transaction Medical Imaging*, 3:179–186, 1984.

[141] A. D. Waller. A demonstration on man of electromotive changes accompanying the heart's beat. *Journal Physiology*, 8(18):229–34, 1887.

[142] G. Walraven. Basic arrhythmias. *Basic arrhythmias*, 7:1–11, 2011.

[143] R. J. Warp and J. T. Dobbins. Quantitative evaluation of noise reduction strategies in dual-energy imaging. *Medical Physics*, 30(2):190–198, 2003.

[144] Y. Watanabe, K. Uotani, T. Nakazawa, M. Higashi, N. Yamada, Y. Hori, S. Kanzaki, T. Fuduka, T. Itoh, and H. Naito. Dual-energy direct bone removal ct angiography for evaluation of intracranial aneurysm or stenosis: comparison with conventional digital subtraction angiography. *Eur. J. Radiol.*, 19:1019–1024, 2009.

[145] WHO. Cardiovascular diseases (cvds): Key facts. Updated, January 2015.

[146] J. F. Williamson, S. Li, S. Devic, B. R. Whiting, and F. A. Lerma. On two-parameter model of photon cross sections: Application of dual-energy ct imaging. *Med. Phys.*, 33(11):4115–4129, 2006.

[147] T. Zhang, W. Lu, and J. Peng. Adaptive image matching via spatial varying gray-level correction. *Institute of Electrical and Electronics Engineers Transaction Communication*, 43(5):1970–1981, 1995.

[148] Z. Zhong, D. Chapman, R. Menk, J. Richardson, S. Theophanis, and W. Thomlinson. Monochromatic energy-subtraction radiography using a rotating anode source and a bent laue monochromator. *Physics Medical Biology*, 42(9):1751–1762, 1997.

[149] L. Zhu, Y. Xie, J. Wang, and L. Xing. Scatter correction for cone-beam ct in radiation therapy. *Medical Physics*, 36(6):2258–2268, 2009.

Chapter 2

Energy subtraction angiography is comparable to digital subtraction angiography in terms of iodine Rose SNR

This chapter is adapted from a manuscript entitled "Energy subtraction angiography is comparable to digital subtraction angiography in terms of iodine Rose SNR" by Christiane Sarah Burton, John R Mayo and I. A. Cunningham, Medical Physics, 43(11) 5925-5933 (2016).

2.1 Introduction

Cardiovascular disease (CVD) is the leading cause of mortality worldwide.[3] It was estimated that 17.5 million people died of CVD in 2012, representing 31% of all global deaths, and of these, an estimated 7.4 million were due to coronary artery disease.[73, 7]

Angiography is widely used in the assessment and treatment of CVD[230] and digital subtraction angiography (DSA)[65] remains the reference standard for most non-cardiac imaging. DSA requires the acquisition of a series of images acquired before, during and after injection of an iodinated contrast agent, with subtraction of selected mask (pre-injection) images from contrasted (post-injection) images to suppress non-iodinated structures. However, acquisition of mask and contrasted images may be separated by several seconds and patient motion can introduce artifacts that may render a study non-diagnostic.[78] Although many software tools have been developed to assist with image registration for in-plane translation and rotations,[71, 137, 40, 78, 214, 94] uncooperative patients and involuntary motions (e.g. respiratory, swallowing and bowel gas) remain the primary cause of poor image quality.[13, 17, 128] As a consequence, DSA remains largely unsuccessful for cardiac imaging[213] where non-subtracted angiography requiring higher radiation exposures and iodine concentrations remains the standard.

Dual-energy angiography was proposed in the 1970's[86, 59, 4, 105, 63, 46] as a method for suppressing non-iodinated vasculature by exploiting the energy-dependence of the iodine mass-attenuation coefficient relative to that of other tissues.[74, 91, 135, 177] When implemented using a fast kV-switching generator to acquire low and high energy images in rapid succession, dual-energy angiography has the potential of being less sensitive to motion artifacts by eliminating the need for a mask image.[37, 135] Early dual-energy cardiac images obtained by Molloi and Mistretta[90] and Van Lysel[135] were exciting and demonstrated reduced sensitivity to motion artifacts. However, energy subtraction showed poor image quality in comparison to conventional methods and was not generally adopted.

Instrumentation available to early investigators was based on image intensifiers with video cameras.[56, 74, 177] These systems suffered from veiling glare[111] and other limitations that provided few options for modifying exposure parameters and compromised the low-noise linear response required for dual-energy imaging. Even with the introduction of early flat-panel detectors,[5, 262, 26, 6] Molloi et al.[26] showed only modest improvements in dual energy image quality.

Image quality is determined by a combination of fundamental physics and technical considerations. While early studies identified an opportunity for dual-energy methods, they did not identify whether poor image quality resulted from the physics of x-ray interactions or from engineering limitations of the day.

There is reason to believe that dual-energy methods, called energy-subtraction angiography (ESA) in this article, can compete directly with DSA to produce high-quality angiographic images for the same patient exposure. For example, Tanguay [124] compared image quality using DSA, ESA, and photon-counting-based energy-resolving angiography (ERA) with a theoretical model that was validated using a Monte-Carlo simulation. They concluded that ESA and ERA could, in principle, produce comparable image quality in terms of iodine SNR relative to DSA at low iodine concentrations. Similar results were shown by Burton et al.[218] in our group with a theoretical model that was experimentally validated, showing that ESA could have image SNR similar to DSA with an ideal imaging system. Results from that work differ numerically from the present study due to the use of a sum-of-variances method to estimate image noise rather than the Rose SNR used in this study.

In this article we generalize these results to include the effects of detector readout noise, quantum efficiency and x-ray scatter in a comparison of signal and noise using ESA and DSA. We identify the key system-performance metrics required to achieve near-ideal SNR to show these would have been difficult or impossible to achieve a few years ago and remain a modest challenge today.

2.2 Theory

The success of ESA depends on its ability to produce high-SNR iodine-specific images while suppressing non-iodinated structures. In this section we describe a basic model of iodine signal and noise to compare image quality between ESA and DSA. We use the Rose SNR,[235, 236] normalized by the square-root of patient entrance exposure, as a figure of merit that is independent of exposure level. The model includes the effect of detector quantum efficiency and readout noise, and (patient) x-ray scatter.

2.2.1 Rose SNR

Rose described the minimal SNR required for visual detection of a uniform low-contrast object of area A in a uniform background with stationary noise. Assuming an "ideal picture device", he showed (with a change in variables) that[235, 236]

$$\text{SNR} \equiv C \frac{N_{\text{b}}}{\sigma_{N_{\text{b}}}} \tag{2.2.1}$$

must have a value of approximately five or greater for confident visual detection where $C = (q_o - q_b)/q_{\text{b}}$ is the object contrast (relative incremental change in scene brightness), q_o and q_{b} are the mean numbers of quanta per unit area (image brightness) in object and background regions respectively, and N_{b} and σ_{N_b} are the mean and standard deviation in the number of background quanta measured in area A. For direct detection of independent Poisson-distributed quanta, $\sigma_{N_b} = \sqrt{N_{\text{b}}}$ and Eq. (2.2.1) simplifies to the familiar form:[215, 252]

$$\text{SNR} = C\sqrt{Aq_b}. \tag{2.2.2}$$

Burgess[215] showed the Rose model to be a good approximation of the Bayesian ideal observer assuming the number of quanta detected is sufficiently large that N_b has Gaussian statistics.

In this article we use the Rose SNR in Eq. (2.2.1) to describe visual detection of an iodinated region having area A in a uniform water-only background. This is valid when A is sufficiently large that all such non-overlapping regions are statistically uncorrelated. Since in practice finite spatial resolution generally introduces correlations between pixels, we sum $N_A \times N_A$ pixel values to create non-overlapping "binned pixels" of area A (described below). This results in smaller images having (nearly) uncorrelated pixels of area A and the Rose SNR can therefore be applied to each binned pixel.

We define d_I and d_W as binned-pixel values in iodinated and background regions, respectively. Working with linear images where pixel values are proportional to q, Eq. (2.2.1) gives

$$\text{SNR} = \frac{d_\text{I} - d_\text{W}}{\sigma_{d_\text{W}}}, \tag{2.2.3}$$

and assuming stationary noise, the discrete auto-covariance function of background regions in binned images is

$$\text{K}_d[\Delta] = \text{K}_d[i-j] = \left\langle (d_i - d)(d_j - d) \right\rangle \tag{2.2.4}$$

where d_i is the value of the ith binned pixel and $\Delta = i - j$. Since $\text{K}_d[\Delta] = \sigma_d^2$ for $\Delta = 0$ and zero otherwise for uncorrelated pixels (only), we define the following condition as our test of pixel independence:

$$\text{R}(N_A) \quad \equiv \frac{\text{K}_d[0]}{\sum_\Delta \text{K}_d[\Delta]} \begin{cases} = 1 & \text{uncorrelated} \\ < 1 & \text{correlated} \end{cases} \tag{2.2.5}$$

and use this condition to determine a value of N_A that gives uncorrelated binned pixels.

It should be mentioned that negative correlations may exist between material-specific images generated using dual-energy methods, such as between water and aluminum basis images in bone-canceling applications.[56, 107] These are unrelated to the issue of pixel-to-
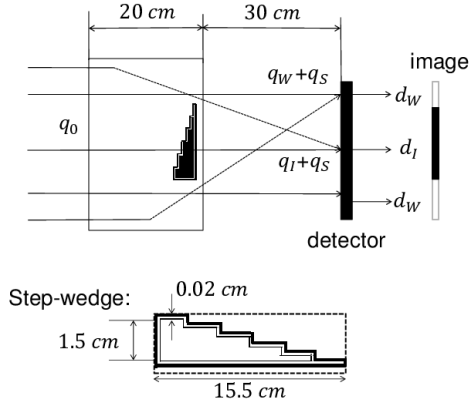
Figure 2.2.1: Schematic illustration of iodine-filled step-wedge immersed in 20 cm of water with incident quanta q_o, transmitted quanta q_W and q_I in non-iodinated and iodinated regions, respectively, and scattered quanta q_S. Corresponding average binned pixel values are d_W and d_I.

pixel correlations in our application of the Rose SNR to individual iodine-specific images.

2.2.2   Rose SNR/$\sqrt{}$KERMA

Our figure-of-merit (FOM) is the Rose SNR comparing binned pixels in iodinated and background regions, normalized by the square-root of air KERMA incident on the test phantom illustrated in Fig. 2.2.1. Background regions have only water along the x-ray path with associated transmission $T_W(E)$ and iodinated regions have additional iodine with transmission $T_I(E)$. The corresponding average x-ray spectral distributions (mm^{-2} keV^{-1}), projected onto the image plane, are given by

$$q_W(E) \;=\; q_o(E)T_W(E)(1+s) \qquad (2.2.6)$$

$$q_I(E) \;=\; q_o(E)T_W(E)(T_I(E)+s) \qquad (2.2.7)$$

respectively where $q_o(E)$ is the unattenuated spectrum and s is the scatter-to-primary ratio. For simplicity, we assume s is not a function of energy and scatter photons have the same

43
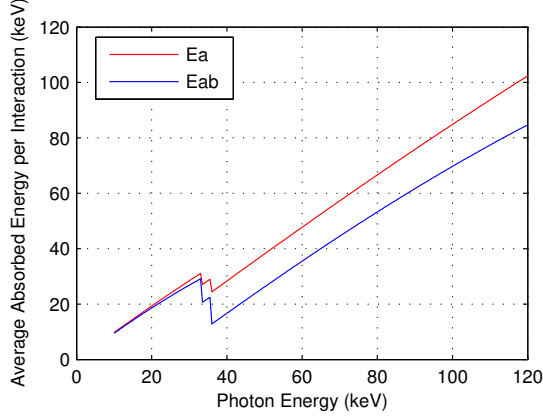
Figure 2.2.2: Average energy absorbed in binned pixel per interacting photon, $E_a(E) = (E_{ab}(E) + E)/2$ where E_{ab} is the tabulated absorbed energy.[161]

energy as primary photons. We accept this simplification since our interesting results are obtained when s is small. We are also evaluating scatter for a patient thickness of 20 cm. The average binned-pixel value and corresponding variance in background water regions for an energy-integrating detector are then given by

$$d_{\mathrm{w}} = kA \int_0^{kV} q_{\mathrm{W}}(E)\alpha(E)E_a(E)\mathrm{d}E \tag{2.2.8}$$

$$\sigma_{d_{\mathrm{w}}}^2 = k^2A \int_0^{kV} q_{\mathrm{W}}(E)\alpha(E)E_a^2(E)\mathrm{d}E + \sigma_{\mathrm{R}}^2 \tag{2.2.9}$$

respectively, where k is a constant of proportionality, α is the detector quantum efficiency, E_a is the average energy absorbed in the binned pixel with each interaction and σ_{R}^2 is the detector additive readout noise. The value of E_a differs to E primarily due to escape of characteristic emissions from the CsI. We make the assumption that, due to partial reabsorption of scatter photons, only half of this energy escapes the binned pixel area and use $E_a(E) = (E_{ab}(E) + E)/2$ as illustrated in Fig. 2.2.2 using tabulated values of E_{ab}, the energy absorbed in CsI.[161] Corresponding expressions exist for d_{I} and $\sigma_{d_{\mathrm{I}}}^2$ in iodinated regions.

Detector noise σ_{R}^2 in detector-signal units is dependent on the detector gain factor k. A

hardware-independent method to quantify noise is in terms of the detector quantum-limit exposure, $\mathcal{K}_L$, defined as the exposure (air KERMA) at which readout variance equals quantum-noise variance. Thus, at the quantum limit,

$$
\begin{aligned}
\sigma_R^2 &= k^2 A \int q_W(E)\alpha(E)E_a^2(E)\mathrm{d}E \\
&= k^2 \mathcal{K}_L A \int Q_o(E)\alpha(E)E_a^2(E)\mathrm{d}E
\end{aligned}
\tag{2.2.10}
$$

where the integration limits are dropped for simplicity, Q_o is the number of quanta/mm^2/Gy and the gain term k cancels when these equations are used to calculate the Rose SNR for evaluating DSA and ESA.

2.2.2.1 DSA Rose SNR

The Rose signal in a DSA image, $\triangle D_D$, is the difference between binned pixel values in iodinated and non-iodinated regions of a log-subtracted image, D_I and D_W respectively, giving

$$
\begin{aligned}
\triangle D_D &\equiv \{D_I - D_W\}_{\mathrm{DSA}} \\
&= \left[\ln(d_I)|_{\mathrm{m}} - \ln(d_I)|_{\mathrm{c}}\right] - \left[\ln(d_w)|_{\mathrm{m}} - \ln(d_w)|_{\mathrm{c}}\right] \\
&= \left[\ln(d_I) - \ln(d_w)\right]_{\mathrm{m}} - \left[\ln(d_I) - \ln(d_w)\right]_{\mathrm{c}}
\end{aligned}
\tag{2.2.11}
$$

where m and c identify mask and contrast images. Noting that $d_I = d_W$ in the mask image gives

$$
\begin{aligned}
\triangle D_D &= \ln\left(\frac{\int q_o(E)\,T_W(E)(1+s)\alpha(E)E_a(E)\mathrm{d}E}{\int q_o(E)\,T_W(E)(T_I(E)+s)\alpha(E)E_a(E)\mathrm{d}E}\right) \tag{2.2.12} \\
&\approx -\ln\langle T_I(E)\rangle_{\alpha q E} \tag{2.2.13}
\end{aligned}
$$

where the last line shows $\triangle D_D$ is approximately equal to the log of the inverse of iodine transmission T_I weighted by the spectral distribution of deposited energy when scatter is

negligible. In this study the more accurate result in Eq. (2.2.12) was used rather than the approximation. Since binned-pixel values are uncorrelated, the background Rose noise, $\sigma^2_{D_W}$, is obtained by differentiating D_W with respect to d_w in Eq. (2.2.11) combined with Eq. (2.2.9):

$$
\sigma^2_{D_W} = 2 \left| \frac{\partial D_W}{\partial d_W} \right|^2 \sigma^2_{d_W} = 2 \frac{1}{d_W^2} \sigma^2_{d_W} \tag{2.2.14}
$$

$$
= \frac{2 \int q_o(E) T_W(E) (1+s) \alpha(E) E_a^2(E) \mathrm{d}E}{A \left| \int q_o(E) T_W(E) (1+s) \alpha(E) E_a(E) \mathrm{d}E \right|^2}
$$

$$
+ \frac{2\sigma_R^2}{k^2 A^2 \left| \int q_o(E) T_W(E) (1+s) \alpha(E) E_a(E) \mathrm{d}E \right|^2}. \tag{2.2.15}
$$

The factor of 2 is a consequence of assuming equal detector exposures (kV, mAs) for mask and contrasted images and the DSA Rose SNR is therefore given by $\mathrm{SNR_D} = \Delta D_D / \sqrt{\sigma^2_{D_W}}$. Use of methods to reduce mask-image exposures (for example Erik et al.[165]) may alter a comparison of DSA with ESA.

2.2.2.2 ESA Rose SNR

ESA imaging uses low and high-energy images acquired at different kV settings in addition to calibration images at each energy. In this case, the iodine signal is given by[4]

$$
\begin{aligned}
\triangle D_E &\equiv \{D_I - D_W\}_{\mathrm{ESA}} \\
&= \left[w \ln(d_{l,ca}) - w \ln(d_l) + \ln(d_{h,ca}) - \ln(d_h) \right]_I \\
&\quad - \left[w \ln(d_{l,ca}) - w \ln(d_l) + \ln(d_{h,ca}) - \ln(d_h) \right]_W \\
&= w \left[\ln(d_{ca}) - \ln(d_I) - \ln(d_{ca}) + \ln(d_w) \right]_l \\
&\quad - \left[\ln(d_{ca}) - \ln(d_I) - \ln(d_{ca}) + \ln(d_w) \right]_h \\
&= w \left[\ln(d_w) - \ln(d_I) \right]_l - \left[\ln(d_w) - \ln(d_I) \right]_h \tag{2.2.16}
\end{aligned}
$$

where l and h indicate low and high kV spectra, and ca indicates a calibration image at each energy based on an average of many images with 20 cm of water and scaled to match the mAs of the low and high energy images. The calibration images are part of the Alvarez algorithm[4] to obtain approximate transmission factors. The weighting factor w is the ratio between mass attenuation coefficients of water at effective energies E_l and E_h, chosen to suppress image contrast due to water (soft tissue):[4]

$$w = \frac{\left(\frac{\mu}{\rho}\right)_W (E_h)}{\left(\frac{\mu}{\rho}\right)_W (E_l)}. \qquad (2.2.17)$$

Thus:

$$
\begin{aligned}
\triangle D_E &= w \ln \left(\frac{\int q_o(E) T_W(E)(1+s)\alpha(E)E_a(E)dE}{\int q_o(E) T_W(E)(T_I(E)+s)\alpha(E)E_a(E)dE} \right)_l \\
&\quad - \ln \left(\frac{\int q_o(E) T_W(E)(1+s)\alpha(E)E_a(E)dE}{\int q_o(E) T_W(E)(T_I(E)+s)\alpha(E)E_a(E)dE} \right)_h \qquad (2.2.18) \\
&\approx \ln \langle T_I \rangle_{\alpha qE,h} - w \ln \langle T_I \rangle_{\alpha qE,l} \qquad (2.2.19)
\end{aligned}
$$

and

$$
\begin{aligned}
\sigma_{D_W}^2 &= \left[\left| \frac{\partial D_W}{\partial d_w} \right|^2 \sigma_{d_w}^2 \right]_l + \left[\left| \frac{\partial D_W}{\partial d_w} \right|^2 \sigma_{d_w}^2 \right]_h \qquad (2.2.20) \\
&= \left[\frac{w^2}{d_W^2}\sigma_{d_w}^2 \right]_l + \left[\frac{1}{d_W^2}\sigma_{d_w}^2 \right]_h \qquad (2.2.21) \\
&= w^2 \left[\frac{\int q_o(E) T_W(E)(1+s)\alpha(E)E_a^2(E)dE}{A|\int q_o(E) T_W(E)(1+s)\alpha(E)E_a(E)dE|^2} \right]_l \\
&\quad + \left[\frac{\int q_o(E) T_W(E)(1+s)\alpha(E)E_a^2(E)dE}{A|\int q_o(E) T_W(E)(1+s)\alpha(E)E_a(E)dE|^2} \right]_h \\
&\quad + \frac{w^2 \sigma_R^2}{k^2 A^2 |\int q_o(E) T_W(E)(1+s)\alpha(E)E_a(E)dE|_l^2} \\
&\quad + \frac{\sigma_R^2}{k^2 A^2 |\int q_o(E) T_W(E)(1+s)\alpha(E)E_a(E)dE|_h^2} \qquad (2.2.22)
\end{aligned}
$$

showing that ESA signal and noise are simply weighted combinations of DSA signal and noise for the two spectra, as expected. As with DSA, the more accurate Eq. (2.2.18) was used, not the approximation.

2.2.3 Patient Entrance Air KERMA

Patient entrance air KERMA $\mathscr{K}_q$ [μGy] associated with a distribution of x-ray photons incident on the patient $q(E)$ (mm^{-2} keV^{-1}) is given by:[151]

$$\mathscr{K}_q = 1.6022 \times 10^{-11} \int_0^{kV} q(E) \frac{\mu_{en}}{\rho}_{air} (E) E \mathrm{d}E \qquad (2.2.23)$$

where $\frac{\mu_{en}}{\rho}_{air}(E)$ [cm^{2}g^{-1}] is the mass energy-transfer coefficient for air and the scaling factor is required to match units. We use SNR/$\sqrt{\mathscr{K}}$, the Rose SNR per root-KERMA, as our exposure-independent figure-of-merit (FOM) where $\mathscr{K}$ is the sum of mask and contrast exposures for DSA and the sum of low and high-energy exposures for ESA. The FOM is used to compare expected image quality for a given exposure using DSA and ESA, and to estimate the impact each parameter has on the FOM to determine conditions necessary for near-optimal Rose SNR with each.

2.3 Methods and materials

Experimental validation of the theoretical model of SNR/$\sqrt{\mathscr{K}}$ for each method was performed by replicating the model conditions using exposure techniques suggested by previous investigators and summarized in Table 2.1.[135, 262, 171, 162] No effort was made to optimize exposure conditions or maximize the FOM.

The spectra of interacting photons used to calculate air KERMA are illustrated in Fig. 2.3.1, generated using an in-house MATLAB library that implements the Tucker-Barnes algorithm for tungsten-target tubes.[253] Experiments were performed using the
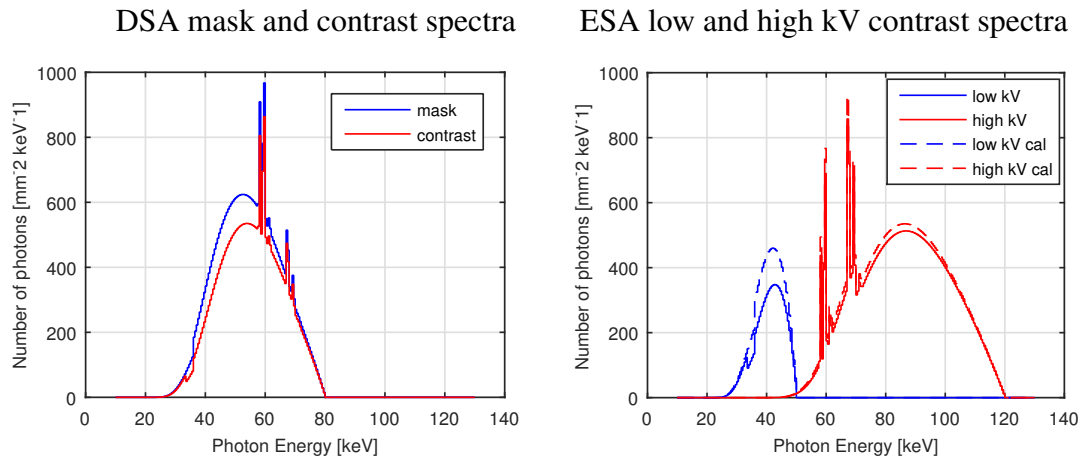
Figure 2.3.1: Energy spectra of x-ray photons interacting in detector used for DSA and ESA calculations (20-cm water, 0.01-g cm^{-2} iodine, 0.5-mm CsI) corresponding to exposure techniques in Table 2.1.

	DSA mask	DSA contrast	ESA low	ESA high
kV	80	80	50	120
mAs	5	5	20	20
Added Filter (material, mm)	-	-	-	Cu, 2.5
Phantom air KERMA (μGy)	165	165	189	104
Detector air KERMA (μGy)	0.63	0.63	0.35	2.29

Table 2.1: Exposure techniques used in an experimental comparison of DSA and ESA. The phantom KERMA was measured with the phantom removed and does not include scatter. The detector KERMA was measured with a large air gap and does not include scatter.
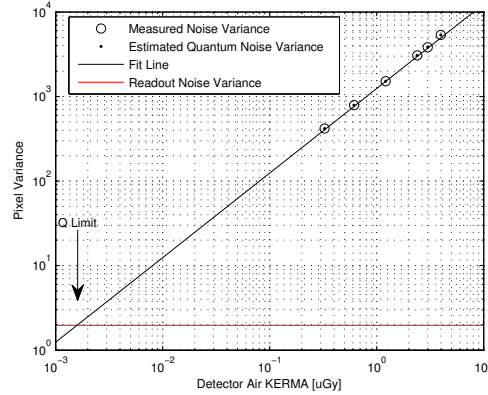
Figure 2.3.2: The quantum-limit exposure is the detector exposure at which readout noise variance (horizontal line) and quantum noise variance (sloped line with data points) intersect. Quantum noise was estimated as measured noise minus readout noise. By changing the mAs setting, it was determined to be approximately 0.0016 μGy at 80 kV as illustrated, although this determination was rather imprecise due to difficulties in achieving a sufficiently low detector exposure without substantial changes in spectral shape from additional filtration.

phantom illustrated in Fig. 4.3.1 consisting of a 20-cm water tank with a sealed and hollow immersible step-wedge with 0.2 mm PMMA walls and containing a liquid contrast agent (0.24 g/cm^3 iodine). The source-image and source-phantom distances were 148 and 98 cm, respectively. Our lab uses a low-noise CsI/CMOS detector (Xmaru 1215CF-MPTM, Rayence Co., Ltd., Korea) with square 49.5-μm elements and 0.5 mm thick CsI, and fast kV-switching generator (EMD Technologies, Montreal Canada) with a custom electronic interface to carefully synchronize image acquisition with x-ray exposure. Images were acquired in single-exposure mode with an interval of several minutes between mask and contrast exposures for DSA while the iodine step wedge was inserted into the water phantom, and several seconds between high and low-energy exposures for ESA. Background noise σ_{D_W} in DSA and ESA images was determined by subtracting two similar images to detrend the data and scaling by $1/\sqrt{2}$. Detector readout noise was measured using DQE*Pro* (DQE Inst., London Canada), expressed as the detector quantum-limit exposure, $\mathscr{K}_L$, and determined to be approximately 0.0016 μGy (Fig. 2.3.2). This is much lower than the detector exposure used in all experiments, confirming that experimental results are not affected by

50
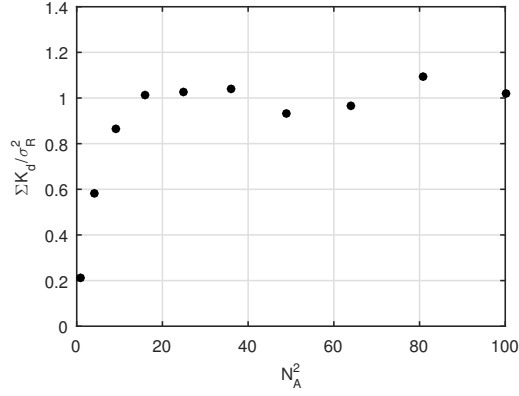
Figure 2.3.3: Average of measured ratio of summed discrete auto-covariance $\sum K_d$ to variance σ_R^2 of binned pixels as a function of number of pixels binned in a square ROI.

readout noise.

The required number of detector elements that must be summed to create statistically independent binned pixels was determined experimentally using Eq. (2.2.5). A detrended noise-only image was obtained as the difference of two 80-kV images of the water phantom, scaled by $1/\sqrt{2}$. The covariance, calculated as N_A, was increased from 1 to 10, illustrated in Fig. 2.3.3. At low values of N_A, the ratio R in Eq. (2.2.5) is low due to correlations between binned pixels caused by system blur. As N_A increases, the area A increases and R increases as blur between binned pixels becomes less significant. When R plateaus at unity, the binned pixels are uncorrelated. Based on Fig. 2.3.3, it is concluded that binning $N_A \times N_A$ with $N_A = 8$ is sufficient to achieve near-independent binned pixels, corresponding to $A = 0.4 \times 0.4$ mm^2.

The scatter/primary ratio s was estimated by measuring exposure at the detector plane as a function of air gap between the detector and water phantom as the phantom was moved. Since the x-ray beam was fully within the phantom for all measurements, the total number of scatter photons generated was not expected to change appreciably, and it was assumed that with a very large air gap of 105 cm, exposure at the detector plane would correspond to primary-beam only. The scatter-to-primary ratio for a specified air gap shown in Fig. 2.3.4
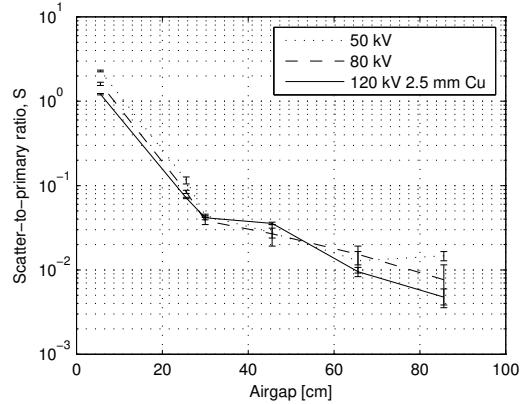
Figure 2.3.4: Measured scatter-to-primary ratio as a function of air gap for 50, 80, and 120 kV spectra.

was then estimated as the relative exposure increase as a function of air gap. The assumption was justified by noting the resulting scatter ratio was less than 0.01 at 85 cm. An air gap of 30 cm was used for all experiments, corresponding to $s \approx 0.04$.

2.4 Results

2.4.1 Experimental validation of Rose SNR model

Figure 2.4.1 shows ESA and DSA images of the iodinated step wedge for phantom entrance air KERMA values of 293 and 331 μGy respectively. Figure 2.4.2 shows excellent agreement between measured values of iodine $SNR/\sqrt{\mathscr{K}}$ determined from these images with theoretical calculations over a range of iodine thicknesses for both DSA and ESA. The close agreement gives confidence in accuracy of the model. In this section the model is used to determine acceptable limits on the model parameters required to ensure near-optimal $SNR/\sqrt{\mathscr{K}}$ values.

2.4.2 Acceptable detector quantum efficiency

Figure 2.4.3 shows iodine $SNR/\sqrt{\mathscr{K}}$ as a function of CsI thickness for ESA and DSA

DSA Iodine Image

ESA Iodine Image
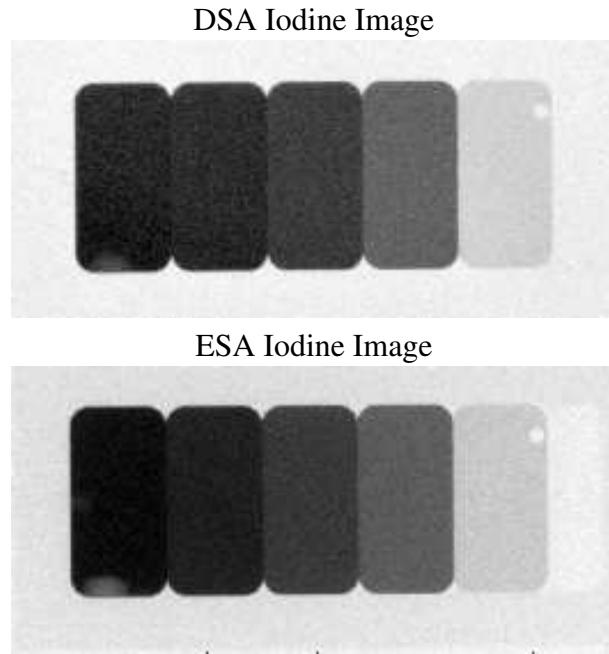
Figure 2.4.1: DSA and ESA images of iodinated step wedge immersed in 20 cm of water with 0.024, 0.096, 0.22, 0.29, and 0.36 g cm^{-2} of iodine for total patient entrance exposures of 331 and 293 μGy, respectively.
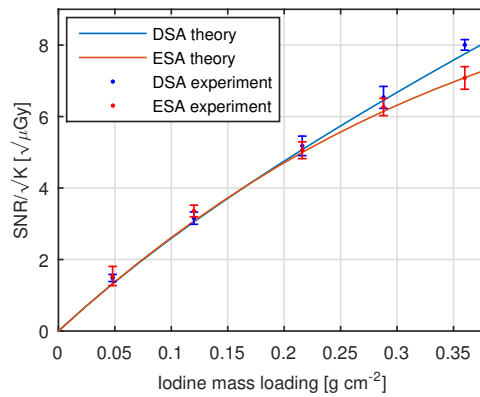
Figure 2.4.2: Comparison of theoretical (lines) of DSA and ESA iodine SNR per root patient air KERMA with experiment (points).
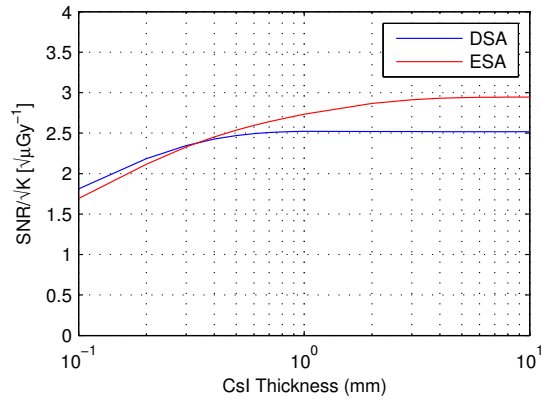
Figure 2.4.3: Theoretical calculation of iodine SNR per root patient air KERMA as a function of detector CsI thickness (0.1 g/cm^2 iodine, no scatter, no readout noise).
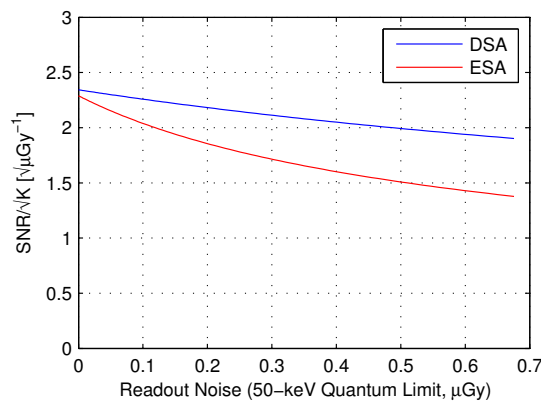
Figure 2.4.4: Theoretical calculation of iodine SNR per root detector air KERMA as a function of detector read noise expressed as the detector quantum-limit exposure at 50 keV (no scatter, 0.3 mm CsI).

assuming no scatter and no readout noise. In general, the two curves are similar although the DSA curve is within 5% of its maximum at 0.4 mm while ESA requires approximately 2 mm. The benefit of increasing from 0.5 mm to 2 mm for ESA is approximately 18%, it is concluded ESA requires at least 0.5 mm, and more if possible to increase the quantum efficiency of the detector for the high-energy spectrum.

2.4.3 Acceptable detector readout noise

Detector (additive) readout noise plays an important role in achieving optimal image quality for both ESA and DSA, but the requirements are more severe with ESA. Figure 2.4.4 shows $SNR/\sqrt{\mathscr{K}}$ as a function of readout noise expressed as the quantum-limit exposure of the detector for 50-keV photons assuming no scatter and 0.3 mm CsI. Results are similar for ESA and DSA for a noise-free detector, but decrease more quickly for ESA than DSA with increasing readout noise. For a given reduction in $SNR/\sqrt{\mathscr{K}}$, detector noise for ESA must be one quarter that for DSA. The acceptable quantum limit to prevent reduced $SNR/\sqrt{\mathscr{K}}$ for ESA is estimated to be approximately 0.05 μGy. However, this applies to normally-exposed regions of the image and a patient entrance air KERMA of 293 μGy. In more-attenuating parts of a patient, or lower patient exposures, the quantum limit must be lower.

2.4.4 Acceptable scatter

Figure 2.4.5 shows iodine $SNR/\sqrt{\mathscr{K}}$ as a function of scatter/primary ratio s for DSA and ESA. For a given reduction in $SNR/\sqrt{\mathscr{K}}$, the scatter ratio for ESA must be one third that for DSA. The largest acceptable scatter ratio to prevent degradation is estimated to be 0.05 for ESA.
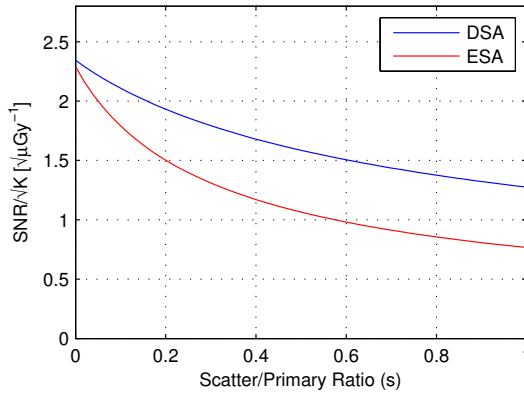
Figure 2.4.5: Theoretical calculation of acceptable scatter-to-primary ratio as a function of iodine mass loading for iodine signal and variance (0.3 mm CsI, no readout noise).

2.5   Discussion

We have demonstrated experimentally that ESA can provide similar image quality to DSA in terms of iodine Rose SNR for angiographic imaging for the same patient-entrance exposure. While this may appear contradictory to early experience with dual-energy angiography,[135] our model of iodine SNR identifies minimal technical requirements to achieve near-optimal ESA that were almost certainly not achieved in the past. For example, it is shown that it is important to maximize CsI thickness to achieve the best possible quantum efficiency for the high-energy spectrum. However, this effect is not dramatic, and while a thickness of at least 0.5 mm is preferable, any thickness greater than 0.3 mm is likely adequate.

Detector readout noise, expressed as a quantum-limit exposure, is a critical consideration. The necessary quantum limit for ESA is one quarter that for DSA, primarily due to the need for a low-energy image. The acceptable value depends on the exposure technique and is 0.05 μGy air KERMA in nominally exposed regions for a patient entrance exposure of 293 μGy as used in the calculation. Van Lysel used a combined exposure of 65 μGy. At this level, the necessary detector quantum limit would be closer to 0.005 μGy. This was not attainable in the past and even today is a challenge to achieve. Our own testing has shown that state-of-the-art CsI-based aSi flat-panel detectors in use in our hospital have

a quantum limit of 0.1 - 0.2 μGy, and this is not sufficient to achieve high-quality ESA imaging. Our laboratory CsI/CMOS detector has a measured quantum limit of 0.0016 μGy which is sufficient.

X-ray scatter also has a dramatic effect on image quality, and the maximum acceptable scatter/primary ratio for ESA is one third that for DSA. High-quality images will be achieved only for scatter-ratio values of approximately 0.05 or less and anti-scatter grids may not provide this level of scatter rejection. We were able to achieve adequate scatter rejection using a 30 cm air gap. The practicality of large air gaps is an issue that must be addressed in some environments and requires larger detectors with lower readout noise. While this is a technical challenge, the benefits are clear and extend beyond dual-energy applications. Soderman et al.[172] used a 30 cm air gap in fluoroscopy rather than an anti-scatter grid and obtained a 70% reduction in patient skin dose with unchanged or slightly improved image quality. Patridge et al. al[166] and Axelsson[152] have proposed replacing grids with a larger air gap as a default technique for children and all but large adults.

While not addressed in this study, the detector must also have a very linear response to ensure adequate contrast suppression with ESA methods, and this is more important with ESA than DSA. We also did not address additional heat-capacity requirements on the x-ray tube for ESA that may be an important consideration. Considerations of scintillator lag are also important with fast kV-switching systems.

Previous investigators have shown that using 50 kV for the low-energy image is close to optimal for an average-size adult (20 cm) and gives the best SNR for a given patient exposure, and this technique was used in this study without further optimization. However, this may be too low for large patients, and places heavy demands on x-ray tube heat loading due to low x-ray production efficiency. Increasing this energy is expected to reduce ESA image quality and is currently being addressed in an ESA optimization study.

While ESA is less susceptible to motion than DSA, it is not immune. We imagine high and low images acquired in approximately 50 ms each, with 50 ms between exposures

to allow for the Cu filter (placed as close to the source as possible) to be removed or inserted. However, slight motion may result in miss-registration between acquisitions and create image artifacts. It may be necessary to investigate methods to re-register images, or use gating methods and acquire both images during diastole when the heart is moving less. It is expected that any such artifacts will become less significant as the time between acquisitions is reduced. An alternative may be to use a fast continuous detector readout at 60 - 90 frames/second (achievable with state-of-the-art low-noise CMOS detectors) with synchronized x-ray exposures that alternate energies and skip every second frame to allow for a rotating filter assembly to transition the filter through the beam. Relative x-ray exposure control could be achieved by modulating exposure times. This would be similar to Van Lysel[177] who acquired low and high-kV images sequentially at 15 frames/second in a dog. More recently, Dean-Ben et al.[158] operated at 50 frames/second without gating or other motion-reduction methods.

2.6   Conclusions

A Rose model analysis was developed to compare the iodine SNR in images obtained using DSA (80 kV) and ESA (energy subtraction, 50 and 120 kV with 2.5 mm Cu filtration with the high energy beam) methods. Excellent agreement was obtained between theoretical and experimental iodine Rose SNR in both DSA and ESA images over a range of iodine concentrations. It is shown that ESA and DSA can produce images with similar iodine SNR for the same phantom entrance exposure, but ESA requires a higher-performing detector to produce near-optimal images. The following specific conclusions are made from this work.

1. ESA imaging requires a detector with good quantum efficiency at a higher energy (120 kV) than DSA. This generally means a thicker absorption layer. For a CsI detector, the CsI should be 0.5 mm or more to achieve near-optimal images.

2. ESA imaging requires a detector with much lower readout noise than DSA, expressed

here as a quantum-limit exposure (where readout noise variance equals quantum noise variance). It is shown that near-optimal results are obtained only with a detector having a 50-keV quantum-limit exposure of 0.05 μGy (detector air KERMA) or lower for the exposure conditions used in this study, and 0.005 μGy or lower for exposure conditions used by early investigators who have studies dual-energy angiography previously. These are both substantially lower than many state-of-the-art aSi panels in use today.

3. ESA imaging is more susceptible to x-ray scatter than DSA. The scatter-to-primary ratio must be 0.05 or less to achieve near optimal results.

While other considerations have not been addressed including imperfect background suppression and tube heat loading considerations, we conclude that ESA can provide images with similar SNR to DSA with the same patient exposure. With implementation of fast kV-switching x-ray machine ESA may reduce motion artifacts for vascular imaging. We believe the challenging technical requirements outlined here may be the reason that early investigations of dual-energy angiography were less successful.

2.7   Acknowledgements

2.8 References

[150] T Albrecht and P Dawson. Gadolinium-dtpa as x-ray contrast medium in clinical studies. *The British Journal of Radiology*, 73:878–882, 2000.

[151] F. H. Attix. *Introduction to Radiological Physics and Radiation Dosimetry*. John Wiley & Sons, 1986.

[152] B. Axelsson. Optimisation in fluoroscopy. *Biomedical Imaging Interventional J.*, 3(2):47, 2007.

[153] Y. Bentoutou, N. Taleb, A. Bounoua, and C. Serief. A results recapitulation of image registration techniques in digital subtraction angiography. *IEEE Nucl. Sci. Symposium Conference Record*, pages 4403–4408, 2008.

[154] Y. Bentoutou, N. Taleb, M. Chikr El Mezouar, M. Taleb, and L. Jetto. An invariant approach for image registration in digital subtraction angiography. *Pattern Recognition in Inf. Sys.*, 35(12):2853– 2865, 2002.

[155] A. E. Burgess. The Rose model, revisited. *J. Opt. Soc. Am.*, 16(3):633–646, 1999.

[156] C. S. Burton, J. R. Mayo, and I. A. Cunningham. Theoretical and experimental comparison of image signal and noise for dual-energy subtraction angiography and conventional x-ray angiography. *Proc. in International Society for Optics and Photonics*, 9412(941219):14, 2015.

[157] I. A. Cunningham and R. Shaw. Signal-to-noise optimization of medical imaging systems. *J. Opt. Soc. Am.*, 16(3):621–632, 1999.

[158] X. L. Dean-Ben, S. J. Ford, and D. Razansky. High-frame rate four dimensional optoacoustic tomography enables visualization of cardiovascular dynamics and mouse heart perfusion. *Scientific Reports*, 5:10133, 2015.

[159] P M Joseph F Kelcz and S K Hilal. Noise considerations in dual energy ct scanning. *Med Phys*, 6(5):418–426, 1979.

[160] P. Hua and I. Fram. Feature-basedimage registration for digital subtraction angiography. *International Society for Optics and Photonics*, 1898:24–31, 1993.

[161] J. S. Hubbell and S. M. Seltzer. Tables of x-ray mass attenuation coefficients and mass energy-absorption coefficients from 1 keV to 20 MeV for elements Z = 1 to 92 and 48 additional substances of dosimetric interest. *Radiat. Research*, 136:147, 1993 (http://www.nist.gov/pml/data/xraycoef/).

[162] T. R. C. Johnson. Dual-energy CT. *Am. J. Roentgenology*, 199:S3–S8, 2012.

[163] Andoh K Kinno Y, Odagiri K. Gadopentetate dimeglumine as an alternative contrast material for use in angiography. *Am J Radiol*, 160:1293–1294, 1993.

Stephen Wilmot Miller, Lawrence M. Boxt, and Suhny Abbara. Cardiac imaging.

[164] B. K. Nallamothu, E. R. Bates, Y. Wang, E. H. Bradley, and H. M. Krumholz. Driving times and distances to hospitals with percutaneous coronary intervention in the united states: implications for prehospital triage of patients with ST-elevation myocardial infarction. *Circulation*, 7(1):1189–1195, 2006.

[165] E. L. Oberstar, M. A. Speidel, B. J. Davis, C. Strotherc, and C. Mistretta, editors. *Feasibility of reduced-dose 3D/4D-DSA using a weighted edge preserving filter*, volume 9783. Proceedings of SPIE, 2016.

[166] J. Partridge, G. McGahan, S. Causton, M. Bowers, M. Mason, M. Dalby, and A. Mitchell. Radiation dose reduction without compromise of image quality in cardiac angiography and intervention with the use of a flat panel detector without an antiscatter grid. *Interventional cardiology and surgery*, 92(4):507–510, 2006.

[167] S. Richard and J. H. Siewerdsen. Optimization of dual-energy imaging systems using generalized NEQ and imaging task. *Med. Phys.*, 31(1):127–139, 2007.

[168] A. Rose. A unified approach to the performance of photographic film, television pickup tube, and the human eye. *J. Soc. of Motion Picture Eng.*, 47(4):272–294, 1946.

[169] A. Rose. The sensitivity performance of the human eye on an absolute scale. *J. Opt. Soc. Am.*, 38(2):196–208, 1948.

[170] John M. Sabol, Gopal B. Avinash, Francois Nicolas, Bernhart Claus, Jianguo Zhao, and James T. Dobbins. The development and characterization of a dual-energy subtraction imaging system for chest radiography based on csi:ti amorphous silicon flat-panel technology. *SPIE.Medical Imaging*, 4320:399–409, 2001.

[171] N. A. Shkumat, J. H. Siewerdsen, D. B. Dhanantwari, A. C. Williams, S. Richard, N. S. Paul, J. Yorkston, and R. Van Metter. Optimization of image acquisition techniques for dual-energy imaging of the chest. *Med. Phys.*, 34(10):3904–3915, 2007.

[172] M. Soderman, B. Hansson, and B. Axelsson. Radiation dose and image quality in neuroangiography: effects of increased tube voltage, added x-ray filtration and antiscatter grid removal. *Interventional Neuroraiology*, 40(4):199–207, 1998.

[173] W. H. Sommer, T. R. Johnson, C. R. Becker, E. Arnoldi, H. Kramer, M. F. Reiser, and K. Nikolau. The value of dual-energy bone removal in maximum intensity projections of lower extremity computed tomography angiography. *Invest. Radiol.*, 44(5):285–292, 2009.

[174] M. Spahn, V. Heer, and R. Freytag. Flat-panel detectors in x-ray systems. *Radiology*, 43(3):340–350, 2003.

[175] D. M. Tucker, G. T. Barnes, and D. P. Chakraborty. Semiempirical model for generating tungsten target x-ray spectra. *Med. Phys.*, 18(2):211–218, 1991.

[176] PhD-Barbara Elmståhl MD Peter Leander MD PhD Mats Nilsson PhD Klaes Golman PhD Torsten AlmeŽn MD PhD Ulf Nyman, MD. Are gadolinium-based contrast media really safer than iodinated media for digital subtraction angiography in patients with azotemia? *Radiology*, 223:311–318, 2002.

[177] M. S. Van Lysel. Optimization of beam parameters for dual-energy digital subtraction angiography. *Med. Phys.*, 21(2):219–226, 1994.

[178] Y. Watanabe, K. Uotani, T. Nakazawa, M. Higashi, N. Yamada, Y. Hori, S. Kanzaki, T. Fuduka, T. Itoh, and H. Naito. Dual-energy direct bone removal ct angiography for evaluation of intracranial aneurysm or stenosis: comparison with conventional digital subtraction angiography. *Eur. J. Radiol.*, 19(4):1019–1024, 2009.

Chapter 3

Optimizing iodine SNR per root air KERMA for energy subtraction methods

This chapter is adapted from a manuscript entitled "Optimizing iodine SNR per root air KERMA for energy subtraction methods" by Christiane Sarah Burton, John R Mayo and Ian A. Cunningham. It has been submitted for consideration for publication in Medical Physics.

3.1   Introduction

The World Health Organization reports cardiovascular diseases (CVDs) as the leading causes of death worldwide and estimated that 17.5 million people died from CVDs in 2012, representing 31% of all global deaths.[3] While x-ray angiography is commonly used in the assessment and management of CVDs,[230] digital subtraction angiography (DSA),[65] the reference standard for most non-cardiac applications, is rarely used. DSA suppresses background and overlying soft-tissue to enhance iodinated vasculature by subtracting a mask image from a series of contrast images.[74, 133, 143, 104, 262, 109] However, the time interval between mask and contrast exposures may result in motion artifacts when imaging moving structures or uncooperative patients. A potential alternative ap-

proach described in the 1990's is dual-energy angiography using a pair of contrast images acquired with low and high kV exposures in rapid succession to produce iodine-specific images.[135] However, early studies showed poor image quality in comparison to conventional DSA and the method was largely abandoned.[46, 13, 37, 90, 135]

We have recently shown that dual-energy methods, called energy-subtraction angiography (ESA) in this article, are able to compete directly with DSA to produce high-quality angiographic images for the same patient exposure. For example, a previous study showed that iodine SNR for ESA can be similar to that of DSA for similar patient entrance exposures using a sum-of-variance[124, 251] and Rose model[216] approach in a theoretical analysis validated by laboratory experiments. However, this can be achieved only when using a very low-noise detector with excellent scatter rejection. We have shown these conditions can be satisfied with modern high-performance detectors but likely not with instrumentation available when dual-energy methods were first investigated.[216]

There have been several optimization studies of iodine SNR for ESA in the past and key studies have shown the need for good spectral separation, normally using a beam-hardening filter with the high-kV exposure.[254, 133, 101] The relative exposure ratio between low and high exposures is also particularly important to achieve optimal image quality. For example, an early study by Van Lysel[133] looked at optimizing iodine SNR in terms of the ratio in the number of interacting photons and found that for a technique using 72 kV for the low-energy exposure and 120 kV with 2.3 mm copper for high-energy exposure, the optimal low:high ratio in number of interacting photons was 1:3. He also showed that near-optimal iodine SNR is achieved using a low-kV setting between 50 and 55 kV with the highest possible high-kV setting, coupled with a 1.5 to 2.0 mm beam-hardening filter on the high-energy spectrum to increase spectral separation. Kelcz et al.[254] confirmed the importance of kV separation and a high-kV beam-hardening filter. Despite these early attempts, iodine SNR for ESA was still deemed inferior to DSA, even with the introduction of early flat-panel detectors.[258, 5, 104, 113, 101, 26, 109, 100, 6, 124]

More recently, Alvarez *et al.*[5] studied performance of a dual-energy detector system using a relative dose allocation optimization described by Sabol *et al.*[255]. Subsequent studies looked at developing an iodine detectability index (DI)[179] that depends on the system modulation transfer function (MTF) and image noise power spectrum (NPS) with a task based function[246] and optimized the DI with respect to the weighting and ratio of low-energy dose to total dose.[101, 109, 249, 248] Richard and Siewerdsen[262] defined an ROC curve in terms of the DI to optimize true-positive and true-negative fractions for an ideal observer for lung nodule applications, and found the optimal entrance dose ratio for an average adult patient to be 1:2 (low:high). Shkumat *et al.*[241] looked at a bone-only image and found the signal-difference-to-noise ratio (SDNR) was optimal for a relative dose ratio of 1:1. Fukao *et al.*[224] optimized dual-energy subtraction chest radiography using a direct-conversion flat-panel detector system and still found the optimal energies were 60 and 120 kV with a dose ratio of 1:2. Ducote and Molloi[222] performed a simulation study to quantify breast density with dual-energy mammography and found the optimal dose ratio to be 1.5:1 using 32 and 96 kV. Carton *et al.*[220] showed an optimal dose ratio for dual-energy photon-counting breast tomosynthesis imaging to be 1:1 and Samei and Saunders[240] found an optimal dose distribution from low to total dose for breast tomosynthesis to be between 0.46 and 0.51, similar to a 1:1 ratio.

Yu *et al.*[249] optimized the contrast-to-noise ratio (CNR) with respect to the dose fraction and found that dose fractions between 0.3 and 0.6 (dose ratios between 1:4 and 1:1.16) are generally acceptable and 0.5 (1:3) is optimal. In a study in 2011, Yu *et al.*[248] looked at optimizing the CNR with respect to dose fraction with monochromatic dual-source dual-energy and found that with 80 and 120 kV the optimal low:high energy dose ratio was 1:2. Yao *et al.*[247] looked at mAs ratio for the efficacy of fixed filtration for rapid kVp-switching dual energy x-ray systems to minimize the noise in dual-energy and found the optimal dose ratio to be 1:3. Saito[239] derived an equation for low to high mAs ratio in terms of electrion density and optimizated the mAs ratio for dual-energy computed tomog-

raphy coupled with balanced filter method. Primak[232] looked at different mAs ratios, however, did not optimize the SNR with respect to the mAs ratio. Atak[212] optimized the CNR with respect to the dose ratio from low kV to total dose for different for cadmium-based photon counting detectors and found that optimal dose ratio is 1:3 for dual-energy.

Many of these studies have shown consistency between (theoretical) numerical calculations and experimental measurements. However, numerical calculations involving many parameters, some of which may be poorly known for individual patient procedures, make it difficult to propose general guidelines and technique recommendations. In this article we look at the key physical parameters that determine iodine SNR in ESA images and their relationships with image quality. A simple relationship is developed that can be used as a guide to determine near-optimal image quality under a wide range of conditions. Results are validated experimentally and then applied in an optimization study to make technique recommendations that maximize iodine SNR-per-root-patient-exposure under various conditions and compared with digital subtraction angiography (DSA) for similar patient exposures.

3.2 Theory

In previous studies we have used both a sum-of-variances (SOV)[251] and Rose model[216] approach to compare iodine SNR per square-root patient-entrance air KERMA (SNR/$\sqrt{\mathscr{K}}$) obtained with ESA and DSA to determine the feasibility of using ESA as an alternative to DSA. The Rose model assumes stationary noise across the image which is generally valid for low-contrast iodine signals. The SOV model looks at the sum of noise variance in both iodinated and background regions. Using a 20-cm water thickness, we showed that ESA could have similar iodine SNR for the same exposure but only when using a very low noise detector, sufficiently thick CsI to achieve high quantum efficiency with the high-energy spectrum, and effective scatter rejection such as a 30 cm air gap. These conditions can be

Independent	Dependent
Iodine mass loading (g/cm^2)	kV$_l$
Water thickness (cm)	mAs$_l$, mAs$_h$
kV$_h$	
Detector material (CsI, Se, ...)	
Filter thickness (mm)	

Table 3.1: Summary of parameters affecting iodine SNR and patient exposure in dual-energy imaging. Only dependent parameters can be optimized on an individual patient basis.

achived with some modern systems, but not easily. In particular, an extremely low-noise detector is required due to the low-level signal acquired with the low-energy exposure. In this study we use a laboratory CsI-CMOS based detector with negligible noise compared to the measured image signals. The theoretical model assumes no additive noise and no scatter.

Table 3.1 shows a summary of parameters that will affect iodine SNR and patient exposure. For purposes of optmization, parameters that cannot be modified during a particular patient study to maximize image quality are considered independent, including vessel thickness (iodine mass loading), patient thickness (water thickness) and detector material and filter thickness. Parameters that can be modified are classified as dependent, including high and low kV, high and low mAs, and filter thickness. However, it is always desireable to set the high kV as high as possible to maximize spectral separattion,[133] and hence this is considered an independent parameter. Iodine SNR/$\sqrt{\mathscr{K}}$ is therefore optimized with respect to kV$_l$, mAs$_l$ and mAs$_h$.

3.2.1 Optimal mAs ratio

A simple monoenergetic model of x-ray signal and noise is developed to describe the important parameters affecting ESA image signal and noise as illustrated in Fig. 3.2.1 assuming parallel beam geometry. A distribution of x-ray quanta q_o [mm^{-2}] is incident on the phantom (water tank). If the transmission factors through water and iodine are T_W and T_I,
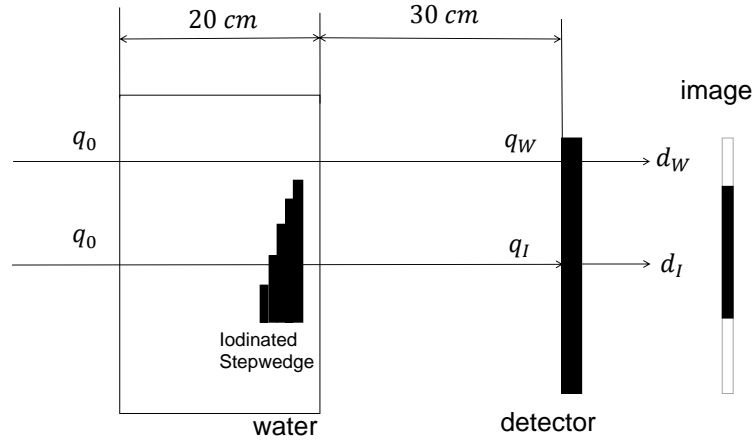
Figure 3.2.1: Schematic illustration of iodine-filled step-wedge immersed in 20 cm of water with incident quanta q_0, transmitted quanta q_W and q_I in non-iodinated and iodinated regions, respectively. Corresponding average binned pixel values are d_W and d_I.

α is the detector quantum efficiency, E is the x-ray quanta energy and k is a constant of proportionality, the detector signals from water-only and iodinated regions of the image are given by:

$$d_W = kAq_0T_W\alpha E \tag{3.2.1}$$

$$d_I = d_WT_I \tag{3.2.2}$$

respectively, where A is an image region of interest large enough to be statistically independent of other such regions. The high h and low l kV pixel values are therefore given by:

$$d_{W,l} = kAq_{0,l,}T_{W,l}\alpha_lE_l \tag{3.2.3}$$

$$d_{W,h} = kAq_{0,h,}T_{W,h}\alpha_hE_hT_{Cu} \tag{3.2.4}$$

$$d_{I,l} = kAq_{0,l}T_{W,l}\alpha_lE_lT_{I,l} \tag{3.2.5}$$

$$d_{I,h} = kAq_{0,h}T_{W,h}\alpha_hE_hT_{I,h}T_{Cu} \tag{3.2.6}$$

where T_{Cu} is the transmission factor of the copper filter in the high-kV exposure. The variance of the background signal is given by

$$\sigma_{dW}^2 \quad = \quad k^2 A q_0 T_W \alpha E^2. \tag{3.2.7}$$

The iodine-specific signal in the ESA image is given by ΔD_E where

$$\begin{aligned} \triangle D_{\mathrm{E}} \quad &\equiv \quad \{D_{\mathrm{I}} - D_{\mathrm{W}}\}_{\mathrm{ESA}} \\ &\quad w\left[\ln\left(d_{W,l}\right) - \ln\left(d_{I,l}\right)\right]_l \\ &\quad - \left[\ln\left(d_{W,h}\right) - \ln\left(d_{I,h}\right)\right]_{\mathrm{h}} \end{aligned} \tag{3.2.8}$$

and therefore

$$\triangle D_{\mathrm{E}} \quad \equiv \quad \ln\left\langle T_{\mathrm{I,h}}\right\rangle_{\alpha qE,\mathrm{h}} - w \ln\left\langle T_{\mathrm{I,l}}\right\rangle_{\alpha qE,\mathrm{l}}, \tag{3.2.9}$$

showing that $\triangle D_{\mathrm{E}}$ does not depend on the dependent parameters being optimized and therefore does not affect the optimization calculation.

The noise variances in ΔD_W and ΔD_I are given by:

$$\sigma_{D_{\mathrm{W}}}^2 \quad = \quad \frac{w^2}{A q_{0,l} T_{W,l} \alpha_l} + \frac{1}{A q_{0,h} T_{Cu} T_{W,h} \alpha_h} \tag{3.2.10}$$

and

$$\sigma_{D_{\mathrm{I}}}^2 \quad = \quad \sigma_{D_{\mathrm{W}}}^2 + \frac{w^2}{A q_{0,l} T_{W,l} \alpha_l T_{I,l}} + \frac{1}{A q_{0,h} T_{Cu} T_{W,h} \alpha_h T_{I,h}} \tag{3.2.11}$$

respectively. Similar to previous work,[216] we normalize the iodine SNR by the patient entrance air KERMA, $\mathscr{K}$, where:

$$\mathscr{K} \quad \propto \quad q_{0,l} E_l + q_{0,h} T_{Cu} E_h. \tag{3.2.12}$$

3.2.1.1 Rose Model

The Rose model considers background noise only. The Rose figure-of-merit (FOM$_R$) is therefore given by FOM$_R$ = SNR$^2/\mathscr{K} \propto \triangle D_E^2/\left(\sigma_{D_W}^2\mathscr{K}\right)$. Since only the denominator can be optimized, the FOM is maximized by minimizing the product $\sigma_{D_W}^2\mathscr{K}$, where:

$$\sigma_{D_W}^2\mathscr{K} \quad \propto \quad \frac{w^2 E_l}{AT_{W,l}\alpha_l} + \frac{w^2 q_{0,h}E_h T_{Cu}}{Aq_{0,l}T_{W,l}\alpha_l}$$
$$+ \frac{q_{0,l}E_l}{Aq_{0,h}T_{W,h}\alpha_h T_{Cu}} + \frac{E_h}{AT_{W,h}\alpha_h}.$$

The optimal ratio in number of low:high energy x-ray quanta incident on the phantom, γ, is obtained by substituting

$$\gamma = \frac{q_{0,l}}{q_{0,h}}$$

and differentiating:

$$\frac{\partial}{\partial\gamma}\left(\sigma_{D_W}^2\mathscr{K}\right) \quad = \quad -\frac{1}{\gamma^2}\frac{w^2 E_h T_{Cu}}{AT_{W,l}\alpha_l} + \frac{E_l}{AT_{Cu}T_{W,h}\alpha_h}. \qquad (3.2.13)$$

Setting the result to zero gives the low:high ratio in the number of quanta incident on the phantom that maximizes FOM$_R$ as:

$$\gamma = \frac{q_{0,l}}{q_{0,h}} = wT_{Cu}\sqrt{\frac{E_h T_{W,h}\alpha_h}{E_l T_{W,l}\alpha_l}}. \qquad (3.2.14)$$

Similarly, for a given low and high energy the optimal mAs ratio for low and high energy spectra is given by

$$\frac{mAs_l}{mAs_h} = wT_{Cu}\sqrt{\frac{E_h}{E_l}\frac{T_{W,h}}{T_{W,l}}\frac{\alpha_h}{\alpha_l}}. \qquad (3.2.15)$$

3.2.1.2 Sum of Variances

The SOV model considers background and iodinated region noise separately, and is a more accurate description of detectability when image noise is different in background and iodi-

nated regions. This is expected with higher iodine mass loadings. The SOV FOM is given by $\text{FOM}_S = \text{SNR}^2/\mathcal{K} \propto \triangle D_E^2 / \left((\sigma_{D_W}^2 + \sigma_{D_I}^2)\mathcal{K} \right)$. Extending the above analysis gives:

$$
\begin{aligned}
\sigma_{D_I}^2 \mathcal{K} \quad \propto \quad & \frac{w^2 E_l}{A T_{W,l} \alpha_l T_{I,l}} + \frac{w^2 q_{0,h} E_h T_{Cu}}{A q_{0,l} T_{W,l} \alpha_l T_{I,l}} \\
& + \frac{q_{0,l} E_l}{A q_{0,h} T_{W,h} \alpha_h T_{Cu} T_{I,h}} + \frac{E_h}{A T_{W,h} \alpha_h T_{I,h}} \\
& + \frac{w^2 E_l}{A T_{W,l} \alpha_l} + \frac{w^2 q_{0,h} E_h T_{Cu}}{A q_{0,l} T_{W,l} \alpha_l} \\
& + \frac{q_{0,l} E_l}{A q_{0,h} T_{W,h} \alpha_h T_{Cu}} + \frac{E_h}{A T_{W,h} \alpha_h}.
\end{aligned}
\tag{3.2.16}
$$

Differentiating with respect to γ gives

$$
\begin{aligned}
\frac{\partial}{\partial \gamma} \left((\sigma_{D_W}^2 + \sigma_{D_I}^2)\mathcal{K} \right) \quad = \quad & -\frac{1}{\gamma^2} \frac{w^2 E_h T_{Cu}}{A T_{W,l} \alpha_l} + \frac{E_l}{A T_{Cu} T_{W,h} \alpha_h} \\
& -\frac{1}{\gamma^2} \frac{w^2 E_h T_{Cu}}{A T_{W,l} \alpha_l T_{I,l}} + \frac{E_l}{A T_{Cu} T_{W,h} \alpha_h T_{I,h}}
\end{aligned}
\tag{3.2.17}
$$

and setting to zero gives

$$
\frac{mAs_l}{mAs_h} = w T_{Cu} \sqrt{\frac{E_h}{E_l} \frac{T_{W,h}}{T_{W,l}} \frac{\alpha_h}{\alpha_l} \frac{\left(1 + \frac{1}{T_{I,l}}\right)}{\left(1 + \frac{1}{T_{I,h}}\right)}}.
\tag{3.2.18}
$$

Equations (3.2.15) and (3.2.18) give similar conditions for optimal results and can be used as a guide for determining optimal mAs ratio as a function of ratios in average energies, water transmission through the phantom (patient) and detector quantum efficiencies, as well as iodine transmission and copper filter transmission. For low iodine concentrations ($T_I \approx 1$) the Rose model and SOV model are nearly equivalent as expected.

Detector Type	Compound Density
Cesium Iodide[228], CsI	4.51 $\frac{g}{cm^3}$
Gadolinium(III) Oxisulphide[231], Gd_2O_2S	7.41 $\frac{g}{cm^3}$
Selenium, Se	4.81 $\frac{g}{cm^3}$

Table 3.2: Density of elements that are used in detectors

3.2.2 Heat units

Production of x rays at lower kV settings is less efficient, and tube heat loading can be an important consideration with large patients.[133] Heat produced at the target x-ray tube, measured in radiographic heat units may be calculated using the following formula:[223]

$$H = kV \times mAs \qquad (3.2.19)$$

where H is the number of heat units per exposure, kV is the peak kilo-voltage, and mAs is the product of current (mA) and time (s). The quantity H is used to compare expected heat units for a similar patient entrance air KERMA for DSA and ESA, and to estimate the impact each parameter has on the quantity to determine conditions necessary for optimal or near-optimal ESA.

3.2.3 Detector type

The detector quantum efficiencies in Eqs. (3.2.15) and (3.2.18) are determined by the detector converter material, density and thickness. Table 3.2 shows converter materials and compound density for detectors in common use.

3.3 Methods and materials

We examined each component of eq. 3.2.14 and eq. 3.2.18 separately and used mass-attenuation coefficients provided from the National Institute of Standards and Technology where applicable. For each component examined we used low kVs of 50, 60, and 70 kV,
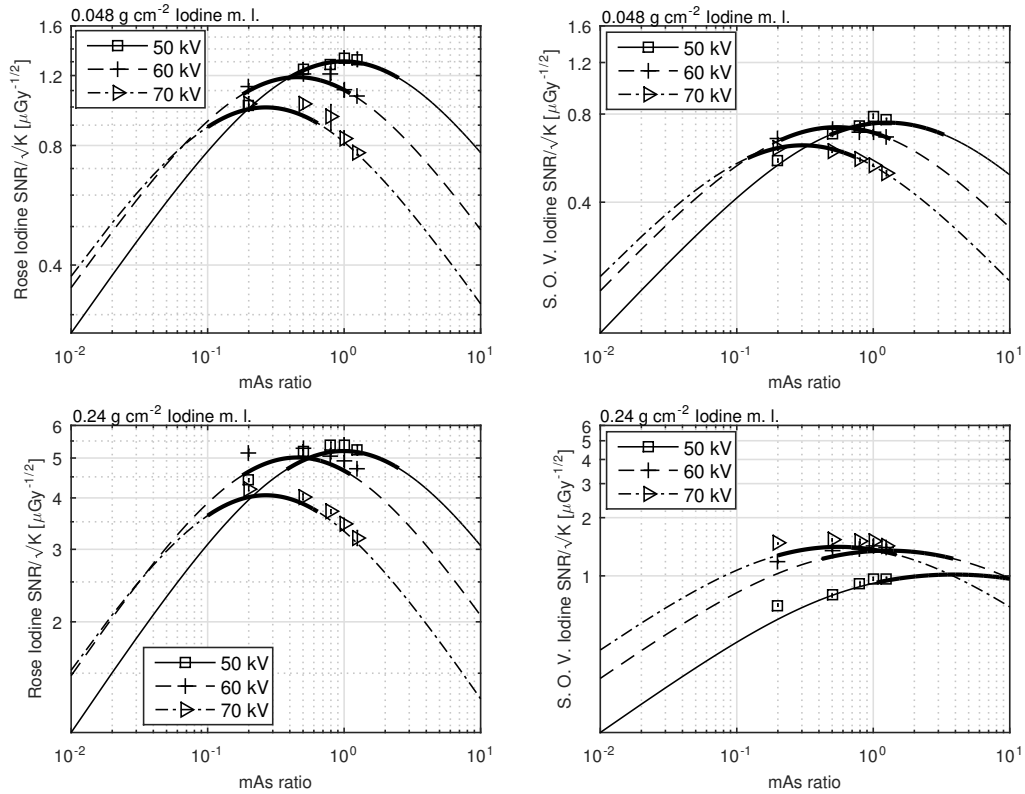
Figure 3.3.1: Plot showing theoretical (line) polyenergetic Rose (left) and SOV (right) calculations for iodine $SNR/\sqrt{\mathscr{K}}$ (no scatter, no read noise) as a function of mAs ratio with corresponding experimental validation (points) for water thicknesses of 20 cm for a fixed high kV of 120 kV with 2.5 mm copper filtration and low kV of 50, 60, and 70 kV, for iodine mass loading 0.048 (upper) and 0.24 g cm^{-2}(lower). The bold line segments show iodine $SNR/\sqrt{\mathscr{K}}$ values that are within 10% of the optimal iodine $SNR/\sqrt{\mathscr{K}}$.

and kept the high kV at 120 kV with additional 2.5 mm copper, and with 2.0 mm aluminum for low and high kV. The phantom used for this study is described in Fig. 2.2.1.[251, 216] Using our theoretical model for iodine $SNR/\sqrt{\mathscr{K}}$ we varied the mAs ratio for low kV of 50, 60, and 70 kV, and with a fixed high kV of 120 kV (2.5 mm copper) each for water thicknesses of 10, 20, and 30 cm and experimentally validated results for water thickness of 20 cm. For a water thickness of 20 cm we varied the mAs ratio for different flat panel detector each with a thickness of 500 μm. Using our theoretical model for iodine $SNR/\sqrt{\mathscr{K}}$ we varied the mAs ratio for 50 and 60 kV using different detector materials each with a thickness of 500 μm.
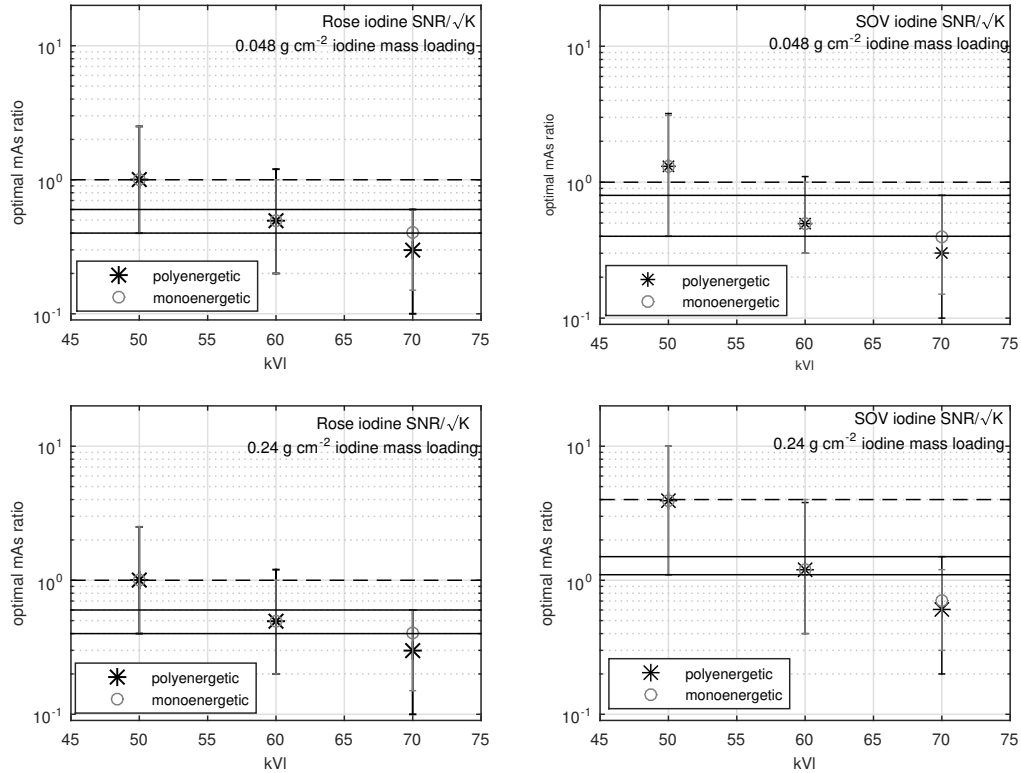
Figure 3.4.1: Optimal mAs ratio as a function of low kV that produces a maximum FOM (SNR/$\sqrt{\mathcal{K}}$) for Rose (left) and SOV (right) methods using iodine mass loadings of 0.048 g cm^{-2}(upper) and 0.24 g cm^{-2} (lower). The dashed line gives a near-optimal mAs ratio that is within 10% of the peak FOM at a low-kV setting of both 50 and 60 kV. The two solid lines bound a range in mAs ratio values in which the FOM is within 10% of the peak FOM for 50, 60 and 70 kV.

3.4   Results

3.4.1   Optimal mAs ratio

Figure 3.3.1 shows excellent agreement between theoretical calculations and experimentally measured Rose and SOV iodine SNR/$\sqrt{\mathcal{K}}$ values. The close agreement gives confidence in the theoretical model. Experimental uncertainties (standard deviation of multiple measurements) are indicated as error bars on each symbol.

Several other observations can be made from these results. For example, the Rose model FOM values depend on iodine mass loading, but the optimal mAs ratio does not. This is expected as the Rose model result is based on noise in water background only and

iodine loading does not appear in the simple optimal mAs ratio expression in Eq. (3.2.15).

The Rose optimal mAs ratio decreases with increasing low kV setting, although the FOM curve has a relatively broad peak. With low iodine mass loadings (0.048 g/cm^2) the SOV and Rose methods give the same optimal mAs ratio. As iodine loading increases (0.24 g cm^{-2}), the SOV optimal mAs ratio is dependent on the low kV setting. These results are all consistent with Eqs. (3.2.15) and (3.2.18).

Figure 3.4.1 shows the mAs ratio that gives an optimal FOM using both Rose and SOV methods as a function of low kV using iodine mass loadings of 0.048 g cm^{-2} and 0.24 g cm^{-2}. The error bars give the range of mAs ratio values that will produce a FOM within 10% of the peak FOM. The 10% threshold was chosen arbitrarily as an indication in the range of mAs values that will have minimal impact on image quality and FOM. The dashed line gives a near-optimal mAs ratio that is within 10% of the peak FOM at a low-kV setting of both 50 and 60 kV. This gives an optimal mAs ratio of 1:1 for all iodine loadings using the Rose method, and increases from 1:1 at low iodine loadings to 3:1 at high iodine loadings with the SOV method. The two solid lines bound a range in mAs ratio values in which the FOM is within 10% of the peak FOM for 50, 60 and 70 kV. It gives a range of 0.4:1 to 0.6:1 for all iodine loadings using the Rose method.

Technique optimization to maximize image SNR is most critical for imaging low-contrast iodinated structures. A more complete picture of low-contrast optimization is obtained from the contour plots in Fig. 3.4.1 showing both Rose and SOV FOM values as a function of phantom thickness and mAs ratio. For 50 and 60 kV, an mAs ratio of 1:1 gives optimal or near optimal iodine SNR for water thicknesses of 10-30 cm and above, correponding to average and thick patient thicknesses. For a limb or patient thicknesses less than 10 cm, an mAs ratio of 0.6:1 to 0.8:1 gives optimal or near optimal iodine SNR.

Similar results are obtained using the average energy of both low and high energy spectra in a mono-energetic model as illustrated in Fig. 3.4.3.

As illustrated in Fig. 3.4.5, the optimal mAs ratio for 50/120 and 60/120 kV does not
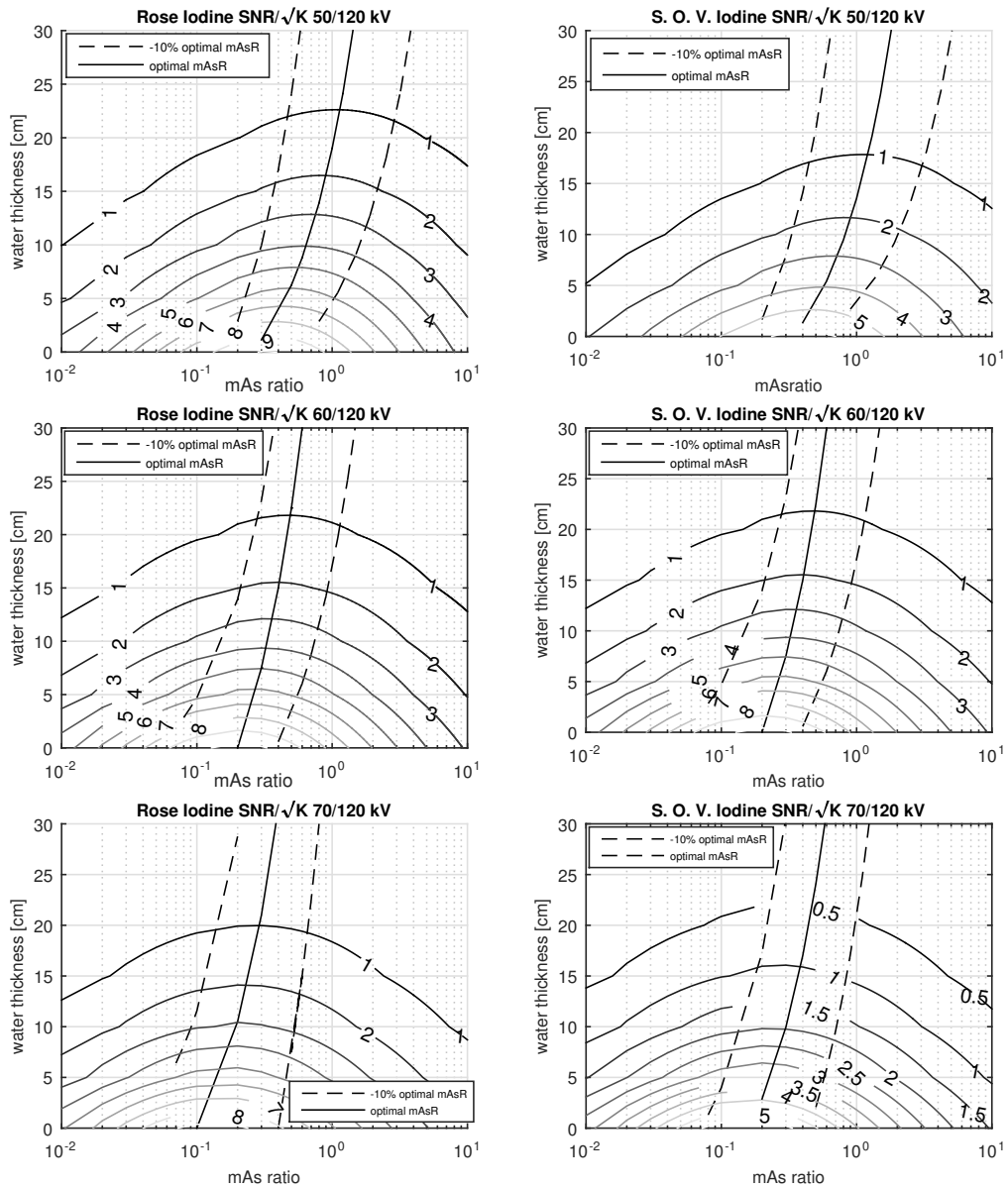
Figure 3.4.2: Contour plots showing polyenergetic calculations for Rose (left column) and SOV (right column) iodine $SNR/\sqrt{\mathscr{K}}$ as a function of water thickness (cm) and mAs ratio using low kV values of 50, 60, and 70 kV for iodine mass loading of 0.048 g cm^{-2} with lines of best fits through optimal iodine $SNR/\sqrt{\mathscr{K}}$ values and values that is 10% to that of optimal iodine $SNR/\sqrt{\mathscr{K}}$.
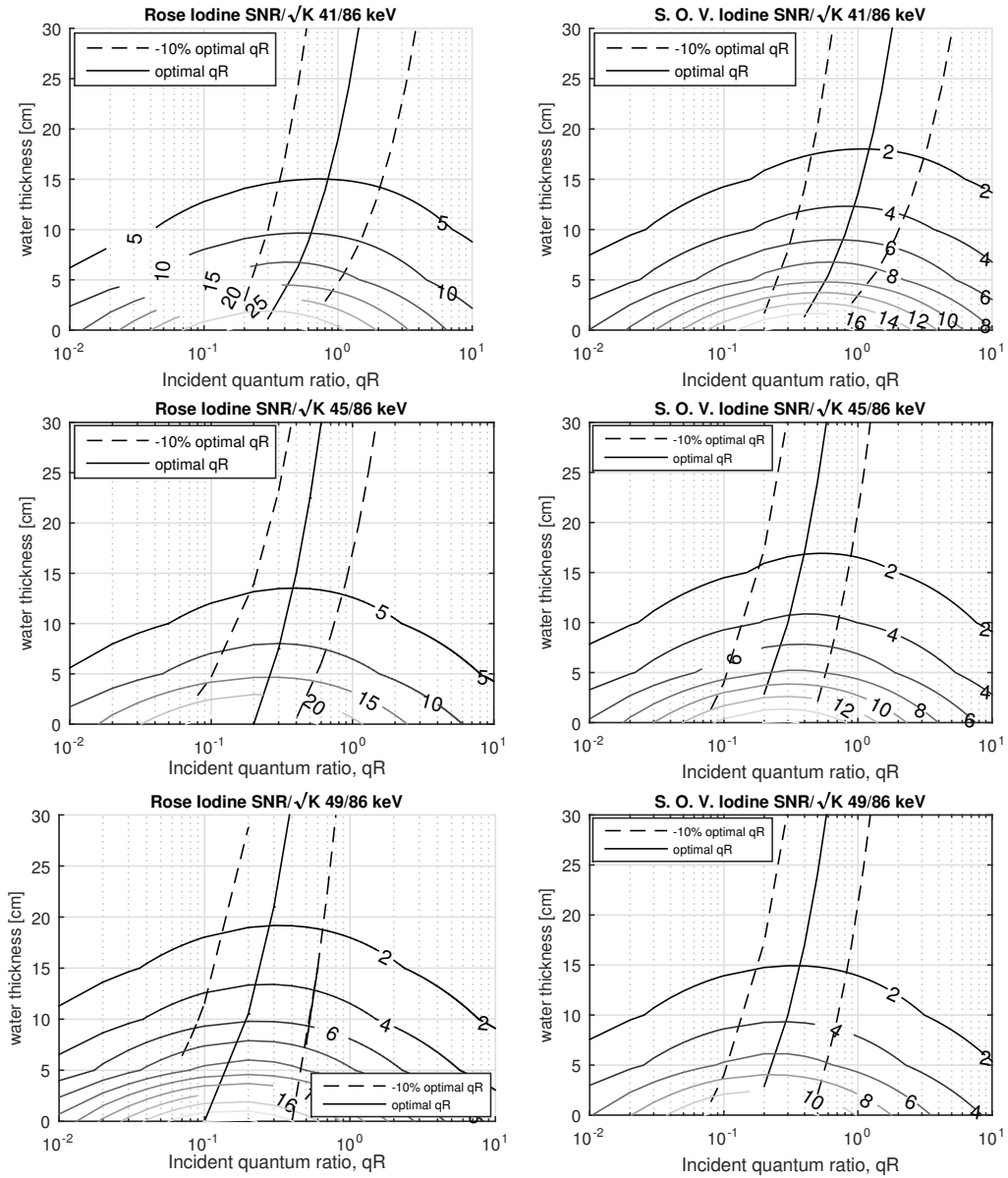
Figure 3.4.3: Contour plots showing monoenergetic calculations for Rose (left column) and SOV (right column) iodine SNR/$\sqrt{\mathscr{K}}$ as a function of water thickness (cm) and mAs ratio using low kV of 50, 60, and 70 kV for iodine mass loading of 0.048 g cm^{-2} with lines of best fits through optimal iodine SNR/$\sqrt{\mathscr{K}}$ values and values that is 10% to that of optimal iodine SNR/$\sqrt{\mathscr{K}}$.
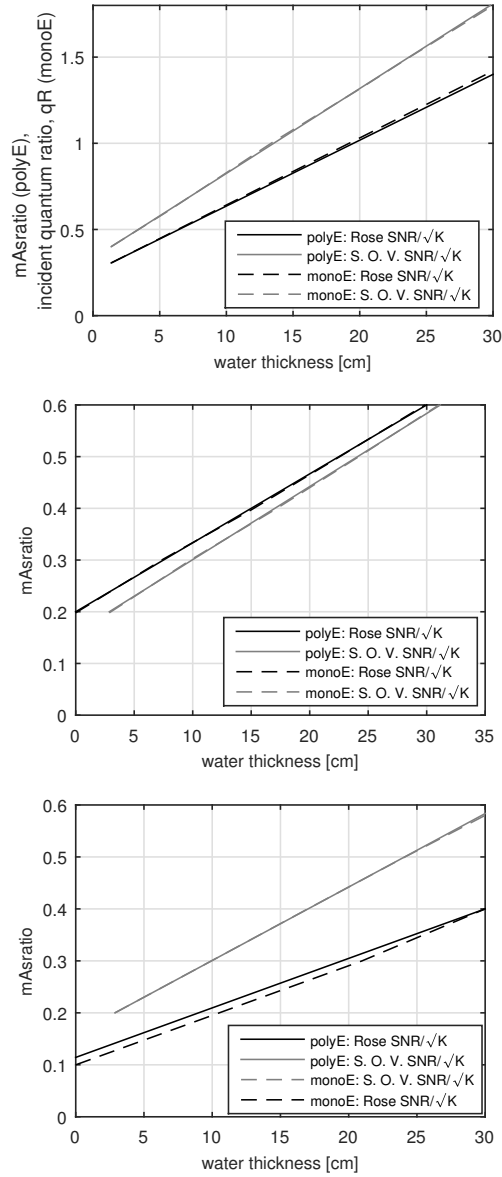
Figure 3.4.4: Comparion lines of best fits through optimal iodine SNR/$\sqrt{\mathcal{K}}$ values and values that is 10% to that of optimal iodine SNR/$\sqrt{\mathcal{K}}$ between polyenergetic and monoenergetic calculations.
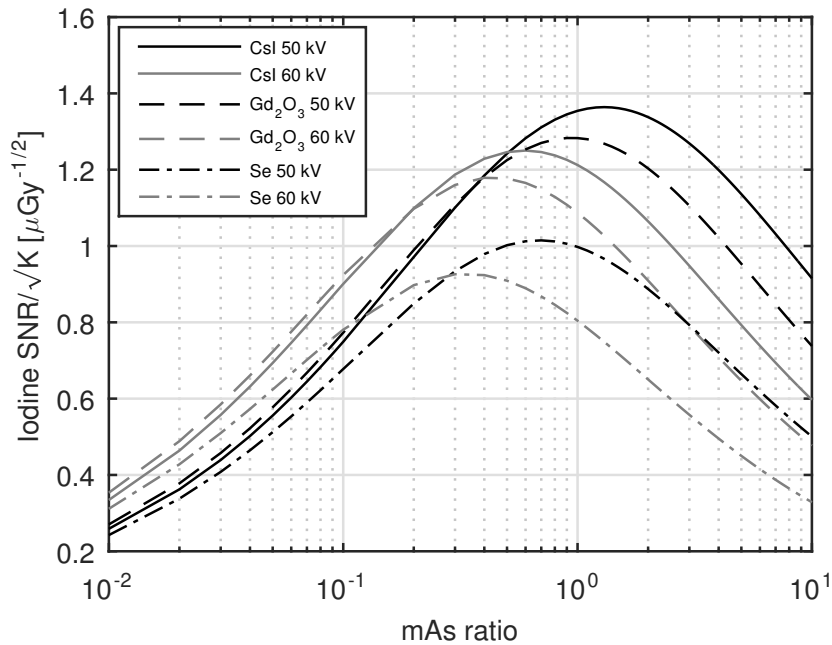
Figure 3.4.5: Theoretical polyenergetic iodine $SNR/\sqrt{\mathscr{K}}$ as a function of mAs ratio for CsI, Se and Gd_2O_2S detector converter materials for an iodine mass loading of 0.048 g cm^{-2} for 20 cm of water for a fixed high kV (120 kV) and low kV of 50 and 60 kV.

depend on detector material, suggesting the recommendations from this study apply to CsI, Se and Gd_2O_2S based detector systems.

Figure 3.4.6 shows the Rose and SOV iodine FOM as a function of iodine mass loading. The Rose result increases monotonically as the iodine mass loading increases since noise does not change and iodine signal increases with increasing iodine attenuation. However, the SOV result increases to approximately 0.1 gcm^{-2} and decreases above this due to the increase in image noise in high-iodine attenuation regions of the image. In general, the SOV method is more correct for describing detectability but the Rose method is fine for optimization of low iodine signals where optimization is generally more important.

Table 3.3 shows a comparison of tube heat loading associated with the optimal mAs ratio compared with DSA for the same Rose FOM.
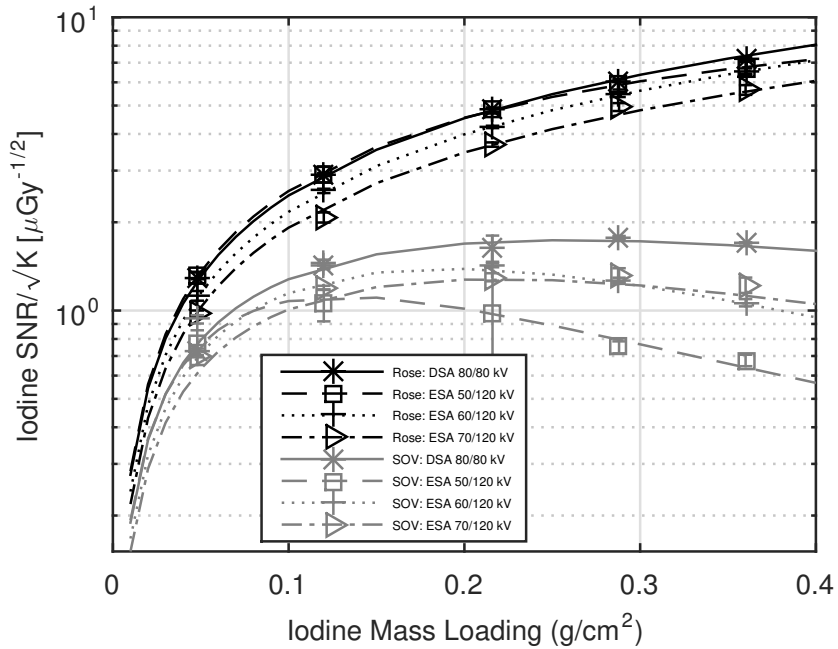
Figure 3.4.6: Optimal mAs ratio as a function of water thickness for low kVs of 50, 60, and 70 kV with fixed high kVp of 120 kV with 2.5 mm copper filtration for monoenergetic spectra.

Method	kV combination	mAs combination	mAs Ratio	heat units
ESA	50/120	20/20	1:1	3400
ESA	60/120	16/20	0.8:1	3360
ESA	70/120	6/20	0.3:1	2820
DSA	80/80	10/10	1:1	1600

Table 3.3: The kV and mAs combination used to calculate heat units for ESA and DSA exposures with the same Rose FOM.

3.5 Discussion

The optimization results presented here are in general agreement with previous studies where directly comparable. We have shown optimal and near-optimal conditions for the iodine $SNR/\sqrt{\mathscr{K}}$ for low and high iodine mass loadings 0.048 g cm^{-2}and 0.24 g cm^{-2}, respectively. We show the Rose and sum-of-variance iodine $SNR/\sqrt{\mathscr{K}}$ as a function of mAs ratio (polyenergetic) and incident quanta ratio (monoenergetic), with experimental validation for the polyenergetic calculation, for low and high iodine mass loadings of 0.048 g cm^{-2}and 0.24 g cm^{-2}using low kVs of 50, 60, and 70, a high kV of 120 kV (2.5 mm copper), and 20 cm of water. We show that the optimal mAs ratio depends on the low kV for a high kV of 120 kV (2.5 mm of copper filter) and for different thicknesses of water and that the bracket for mAs ratio is being within 10% of optimal iodine $SNR/\sqrt{\mathscr{K}}$ is wide. For 50 kV, mAs ratios of 0.6-1.0 give optimal or within 10% of optimal iodine $SNR/\sqrt{\mathscr{K}}$ for water thicknesses between 2-30 cm. For 60 kV mAs ratios of 0.4-0.8 gives optimal or within 10% of optimal iodine $SNR/\sqrt{\mathscr{K}}$ for water thicknesses between 2-30 cm. For 70 kV mAs ratios of 0.2-0.5 gives optimal or within 10% of optimal iodine $SNR/\sqrt{\mathscr{K}}$ for water thicknesses between 2-30 cm.

We have shown that spectral separation is necessary to achieve relatively good image quality for the same patient entrance air KERMA. This is confirmed by showing that the best iodine $SNR/\sqrt{\mathscr{K}}$ is achieved with low kV values of 50-60 kV for a fixed high kV and for a copper thickness of 2.5 mm for the high kV beam. A few past studies have used kV pairs like 60/120 (2.5 mm copper) kV[89] and 70/120 (1.5-2.0 mm copper) kV[133] with sub-optimal mAs ratios for those kVs. We also confirmed but did not show that varying the high kV from 90-120 kV does not have a significant effect on the iodine SNR, however varying the low kV between 50-90 kV does have a more significant effect on the iodine $SNR/\sqrt{\mathscr{K}}$.[262]

We show that detectors materials, CsI and Gd_2O_2S, with thicknesses of 0.5-mm give better iodine $SNR/\sqrt{\mathscr{K}}$ by a factor of 1.36 and 1.27, respectively, compared to Se detec-

tors. There is a small dependency of detector material with optimal mAs ratio, for CsI and Gd_2O_2S, the optimal ratio is 1.05 and 1.0, respectively, and 0.8 for a-Se using 50 and 120 kV (2.5 mm copper for 120 kV).

We have shown that the heat units per unit detector air KERMA for ESA are a factor of 2 greater than DSA. This might be a limitation, however, we anticipate that fewer images would be required with ESA compared to DSA. With implementation of a fast kV-switching machine motion artifacts may be reduced in addition to providing image quality similar to DSA and ESA may be a viable alternative to DSA when there is patient motion present.

3.6   Conclusion

The optimization of our Rose and sum-of-variance models to maximize the iodine SNR per root incident air KERMA ($\mathrm{SNR}/\sqrt{\mathscr{K}}$) was developed for ESA imaging for fixed high kV of 120 kV with 2.5 mm Cu filtration and low kV values of 50, 60, and 70 kV for water phantom thicknesses between 2 and 30 cm. Excellent agreement was obtained between theoretical and experimental iodine Rose SNR over a range of mAs ratios for a water phantom thickness of 20 cm. We identified the impact of detector material for detectors that are readily available at present that will yield the best possible iodine SNR. We have also identified that heat loading may be a minor limitation. The following specific conclusions are made from this work.

1. A simple expression for the optimal mAs ratio was developed in terms of low and high ratios of: average spectral energies; water transmission factor through a test phantom (representing patient thickness) and detector quantum efficiencies, given by Eq. (3.2.15). The expression was validated experimentally and gave results consistent with a more comprehensive poly-energetic calculation.

2. For water thickness of 2 to 30 cm, optimal ESA images are produced with mAs ratios

(low Energy : high energy) of 1:1 for 50/120 and 60/120 kV settings and 0.3:1 for 70/120 with 2.5 mm copper filtration the high kV spectrum. The low kV settings that give the best possible iodine $\text{SNR}/\sqrt{\mathscr{K}}$ range from 50 to 60 kV for a fixed high kV of 120 kV.

3. Heat units for ESA were estimated to be a factor of 2 greater than DSA for the same iodine $\text{SNR}/\sqrt{\mathscr{K}}$. If heat loading is a limitation with DSA, this could restrict the number of images acquired during an ESA procedure.

4. Best ESA results will be obtained using a CsI-based detector, with an improvement of 30% over Se and 20% over Gd_2O_2S based detectors for the same $\text{SNR}/\sqrt{\mathscr{K}}$.

3.7 Acknowledgements

3.8 References

[179] Medical imaging - the assessment of image quality. ICRU 54, International Commission of Radiation Units and Measurements, 1996.

[180] H. Atak and P. M. Shikhaliev. Dual energy CT with photon counting and dual source systems comparative evaluation. *Institute of Phys. and Eng. in Med.*, 60(23):8949–8975, 2015.

[181] Y. Bentoutou, N. Taleb, A. Bounoua, and C. Serief. A results recapitulation of image registration techniques in digital subtraction angiography. *Institute of Electrical and Electronics Engineers Nuclear Science Symposium Conference Record*, 2008.

[182] Y. Bentoutou, N. Taleb, M. Chikr El Mezouar, M. Taleb, and L. Jetto. An invariant approach for image registration in digital subtraction angiography. *Pattern Recognition in Information Systems*, 35:2853– 2865, 2002.

[183] A. E. Burgess. The rose model, revisited. *J Opt Soc Am A*, 16(3):633–646, 1999.

[184] C. S. Burton, J. R. Mayo, and I. A. Cunningham. Energy subtraction angiography can compete with digital subtraction angiography in terms of image SNR. *Medical Physics*, 43(11), 2016.

[185] Christiane S. Burton, John R. Mayo, and Ian A. Cunningham. Theoretical and experimental comparison of image signal and noise for dual-energy subtraction angiography and conventional x-ray angiography. 9412(19), 2015.

[186] A.-K. Carton, C. Ullberg, K. Lindman, R. Acciavatti, T. Francke, and A. D. A. Maidment. Optimization of a dual-energy contrast-enhanced technique for a photon-counting digital breast tomosynthesis system: I. a theoretical model. *Med. Phys.*, 37(11):5896–5907, 2010.

[187] I. A. Cunningham and R. Shaw. Signal-to-noise optimization of medical imaging systems. *The Journal of the Optical Society of America*, 16(3):621–632, 1999.

[188] J. L. Ducote and S. Molloi. Quantification of breast density with dual energy mammography a simulation study. *Med. Phys.*, 35(12):5411–5418, 2008.

[189] E. Forster. *Equipment for Diagnostic Radiography*. MTP Press Limited Falcon House Lancaster, England, 1985.

[190] M. Fukao, K. Kawamoto, H. Matsuzawa, O. Honda, T. Iwaki, and T. Doi. Optimization of dual-energy subtraction chest radiography by use of a direct-conversion flat-panel detector system. *Radiol. Phys. Technol.*, 8(1):46–52, 2015.

[191] P. Hua and I. Fram. Feature-basedimage registration for digital subtraction angiography. *International Society for Optics and Photonics*, 1898:24–31, 1993.

[192] F. Kelcz, P. M. Joseph, and S. K. Hilal. Noise considerations in dual energy ct scanning. *Med. Phys.*, 6(5):418–426, 1979.

[193] Andoh K Kinno Y, Odagiri K. Gadopentetate dimeglumine as an alternative contrast material for use in angiography. *Am J Radiol*, 160:1293–1294, 1993.

[194] M. P. Kowalski, G. G. Fritz, R. G. Cruddace, A. E. Unzicker, and N. Swanson. Quantum efficiency of cesium iodide photocathodes at soft x-ray and extreme ultraviolet wavelengths. *Appl. Opt.*, 25(14):2440, 1986.

[195] B. K. Nallamothu, E. R. Bates, Y. Wang, E. H. Bradley, and H. M. Krumholz. Driving times and distances to hospitals with percutaneous coronary intervention in the united states: implications for prehospital triage of patients with st-elevation myocardial infarction. *Circulation*, 7(1):1189–1195, 2006.

[196] P. Patnaik. *Handbook of Inorganic Chemicals*. McGraw-Hill, 2002.

[197] A. N. Primak, J. C. R. Giraldo, X. Liu, L. Yu, and C. H. McCollough. Improved dual-energy material discrimination for dual-source CT by means of additional spectral filtration. *Med. Phys.*, 36(4):1359–1369, 2009.

[198] S. Richard and J. H. Siewerdsen. Optimization of dual-energy imaging systems using generalized NEQ and imaging task. *Med. Phys.*, 31(1):127–139, 2007.

[199] A. Rose. A unified approach to the performance of photographic film, television pickup tube, and the human eye. *Journal of the Society of Motion Picture Engineers*, 1946.

[200] A. Rose. The sensitivity performance of the human eye on an absolute scale. *Journal of the Optical Society of America*, 1948.

[201] J. M. Sabol, G. B. Avinash, F. Nicolas, B. Claus, J. Zhao, and J. T. Dobbins. The development and characterization of a dual-energy subtraction imaging system for chest radiography based on CsI:TI amorphous silicon flat-panel technology. *SPIE Med. Imag.*, 4320:399–409, 2001.

[202] M. Saito. Spectral optimization for measuring electron density by the dual-energy computed tomography coupled with balanced filter method. *Med. Phys.*, 36(8):3631–3642, 2009.

[203] E. Samei and R. S. Saunders Jr. Dual-energy contrast-enhanced breast tomosynthesis optimization of beam quality for dose and image quality. *Phys. Med. Biol.*, 56(19):6359–6378, 2011.

[204] N. A. Shkumat, J. H. Siewerdsen, S. Richard, N. S. Paul, J. Yorkston, and R. Van Metter. Dual-energy imaging of the chest: Optimization of image acquisition techniques for the bone-only image. *Med. Phys.*, 35(2):629–632, 2008.

[205] M. Spahn, V. Heer, and R. Freytag. Flat-panel detectors in x-ray systems. *Radiology*, 43:340–350, 2003.

Lawrence M. Boxt Stephen Wilmot Miller and Suhny Abbara. Cardiac imaging.

[206] FRCR T Albrecht, MD and FRCR P Dawson, PhD. Gadolinium-dtpa as x-ray contrast medium in clinical studies. *The British Journal of Radiology*, 73:878–882, 2000.

[207] D. M. Tucker, G. T. Barnes, and D. P. Chakraborty. Semiempirical model for generating tungsten target x-ray spectra. *Medical Physics*, 18(2):211–218, 1991.

[208] R. F. Wagner and D. G. Brown. Overview of a unified SNR analysis of medical imaging systems. *IEEE Trans. Med. Imaging*, 1:210–213, 1982.

[209] Y. Yao, A. S. Wang, and N. J. Pelc. Efficacy of fixed filtration for rapid kVp-switching dual energy x-ray systems. *Med. Phys.*, 41(3):1–12, 2014.

[210] L. Yu, J. A. Christner, S. Leng, J. Wang, J. G. Fletcher, and C. H. McCollough. Virtual monochromatic imaging in dual-source dual-energy CT: radiation dose and image quality. *Med. Phys.*, 38(12):6371–6379, 2011.

[211] L. Yu, A. N. Primak, X. Liu, and C. H. McCollough. Image quality optimization and evaluation of linearly mixed images in dual-source, dual-energy CT. *Med. Phys.*, 36(3):1019–1024, 2009.

Chapter 4

Energy-subtraction method in RANDO anthropomorphic phantom

This chapter consists of a manuscript "Evaluation of an energy subtraction method of angiography in a RANDO anthropomorphic phantom" by Christiane S. Burton, John R. Mayo and Ian A. Cunningham that is being prepared for submission to Medical Physics for consideration as a research article.

4.1   Introduction

Cardiovascular diseases (CVDs) are the leading causes of death globally. It is estimated that 17.5 million people died from CVDs in 2012, representing 31% of all global deaths.[3] X-ray angiography is used to asses CVD, however, in order to increase conspicuity of vessels from soft-tissue and bone in an image, a higher patient entrance exposure is needed. Digital subtraction angiography (DSA) is a technique used in vascular imaging to remove background structures such as bone and lung to enhance iodine filled blood vessels. The problem with DSA is motion artifacts arise between the several seconds between the mask and contrast image acquisition.

Although key previous studies from our laboratory addressed iodine signal-to-noise ratio (SNR) for a given patient entrance exposure for ESA. Tanguay et al.[124] developed a theoretical model for iodine SNR and compared ESA with DSA, and validated the model with Monte Carlo calculations using a Cd-Te based photon counting detector with quantum efficiency is unity. This led into the next few studies where we developed a theoretical model for iodine SNR per root air KERMA but this time with experimental validation using CsI based detectors of thickness 0.05 cm. We concluded that for a technique of 50 and 120 (2.5 mm copper filtration) kVp iodine SNR for ESA to be similar to DSA for similar exposure the scatter-to-primary ratio needs to be less than 0.05 achievable with an air gap of 30 cm and a detector with a quantum-limit on the order of 0.05 μGy.[218, 216] Subsequently we optimized the iodine SNR per root air KERMA with respect to the number of interacting quanta for low and high kV exposures and concluded that an mAs ratio of 1.0 is optimal or near-optimal for low kV of 50-60 kVp.[217] These studies were performed using a two-material composition of water and iodine, however, sometimes in vascular images there is bone, and therefore a two-material decomposition will remove one material (water) and partially suppress two other materials (bone, iodine).

A key study by Liu et al.[229] looked at dual-energy for a three material decomposition where they used mass conservation to express the third material in terms of total mass

and found that the three material decomposition produced more accurate hounsfield units for CT compared to a two-material decompositon for a three-material composition. Other studies looked at differentiating iodine from other material such as calcified plaque in the arteries in CT.[53, 36, 127, 24, 173, 178, 57, 125, 110, 79, 96] However, little has been done to address removing bone for dual-energy for a three material composition of iodine, water, and bone.

The purpose of this study is to show what parameters are needed for suppressing bone from a dual-energy image and show the effect bone suppression has on the iodine signal.

4.2 Theory

The distributions of x-ray quanta (mm^{-2} keV^{-1}) incident on the detector corresponding to non-iodinated and bone regions (Fig. 4.3.1) are given by

$$q_W(E) = q_0(E)T_W(E) \tag{4.2.1}$$

$$q_B(E) = q_W(E)T_B(E) \tag{4.2.2}$$

respectively, where the overhead indicates a random variable (RV), the subscript W denotes water and B denotes cortical bone. The corresponding signals from ideal energy-integrating detectors are given by

$$d_W = k \int_A \int_0^{kV} q_W(E)\alpha(E)E\,dA \tag{4.2.3}$$

$$d_B = k \int_A \int_0^{kV} q_B(E)\alpha(E)ET_I(E)\,dA \tag{4.2.4}$$

where k is a constant of proportionality, α is the quantum efficiency of the detector, E is the energy of the photon, and A is a small region of interest (for example, a single pixel).

ESA imaging uses low and high energy images acquired at different kV settings in addition to calibration images at each energy. It is assumed they can be determined by

averaging many exposures and hence noise from calibration images is assumed negligible. In this case, the iodine signal is given by

$$
\begin{aligned}
\Delta D_{\text{ESA}} &= \{D_{\text{B}} - D_{\text{W}}\}_{\text{ESA}} \\
&= w \left[\ln(d_{\text{W}}) - \ln(d_{\text{B}})\right]_{\text{l}} - \left[\ln(d_{\text{W}}) - \ln(d_{\text{B}})\right]_{\text{h}}
\end{aligned}
\tag{4.2.5}
$$

where l and h indicate low and high kV spectra and the weighting factor w is the ratio between mass attenuation coefficients of water at effective energies E_{l} and E_{h}, chosen to suppress image contrast due to water (soft tissue) and cortical bone:

$$
w_{\text{W}} = \frac{\left(\frac{\mu}{\rho}\right)_{\text{W}}(E_{\text{h}})}{\left(\frac{\mu}{\rho}\right)_{\text{W}}(E_{\text{l}})}.
\tag{4.2.6}
$$

$$
w_{\text{B}} = \frac{\left(\frac{\mu}{\rho}\right)_{\text{B}}(E_{\text{h}})}{\left(\frac{\mu}{\rho}\right)_{\text{B}}(E_{\text{l}})}.
\tag{4.2.7}
$$

Therefore,

$$
\begin{aligned}
\Delta D_{\text{ESA}} &= w \ln \left(\frac{\int_0^{kV_{\text{l}}} q_{\text{W}}(E)\,\alpha(E)E\mathrm{d}E}{\int_0^{kV_{\text{l}}} q_{\text{B}}(E)\,\alpha(E)E\mathrm{d}E} \right) \\
&\quad - \ln \left(\frac{\int_0^{kV_{\text{h}}} q_{\text{W}}(E)\,\alpha(E)E\mathrm{d}E}{\int_0^{kV_{\text{h}}} q_{\text{B}}(E)\,\alpha(E)E\mathrm{d}E} \right).
\end{aligned}
\tag{4.2.8}
$$

Our objective is to find out whether we should be removing bone or soft-tissue from the ESA image.

4.3   Methods and Materials

Figure 4.3.1 shows the first phantom used for this study which consists of iodinated step-wedge submerged in 20 cm thickness of water and bone-mimicking DEXA wedge material (SB3; Gammex-RMI, Middleton, WI, U.S.A.)[35, 45, 77, 33] attached to the outside sur-
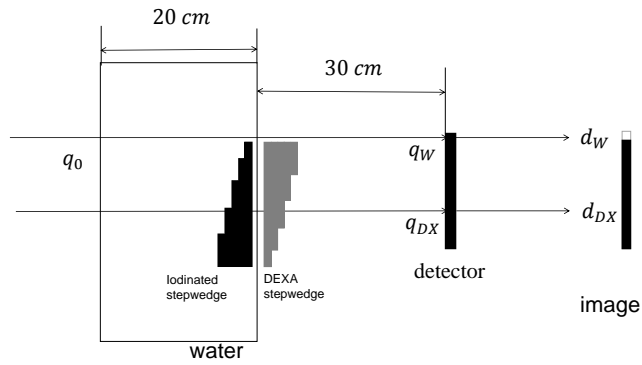
Figure 4.3.1: Phantom setup with DEXA wedge material. Iodine stepwedge not shown.
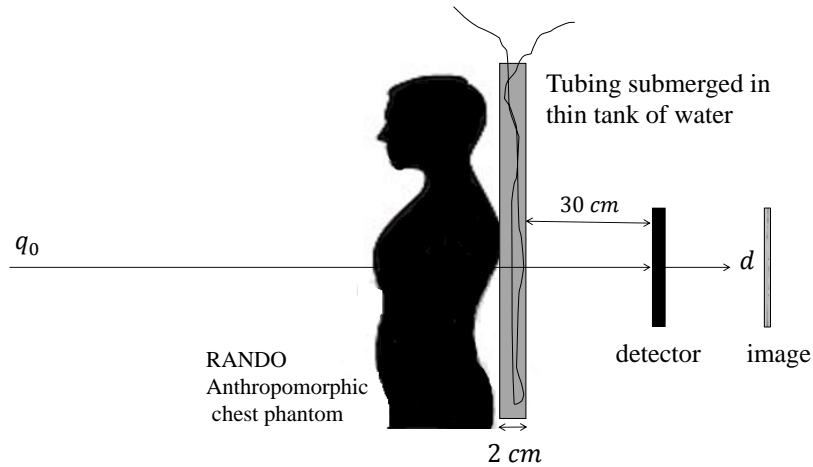
Figure 4.3.2: RANDO anthropomorphic phantom setup with DEXA wedge material. Iodine stepwedge not shown.

face of the tank. We acquired images of the iodine stepwedge and DEXA wedge together, and we took images of each wedge separately to calculate the trasmission factor of iodine and DEXA material for each thickness.

Figure 4.3.2 shows the RANDO anthropomorphic vascular phantom[2] used for this study which also included a thin 2 cm thickness tank of water and water-equivalent iodine-filled tubing submerged in the thin tank of water placed right up against the back of the RANDO phantom. In both cases we used a 30 cm air gap between the surface of the phantom and the surface of the detector. We used a very-low noise CsI/CMOS detec-
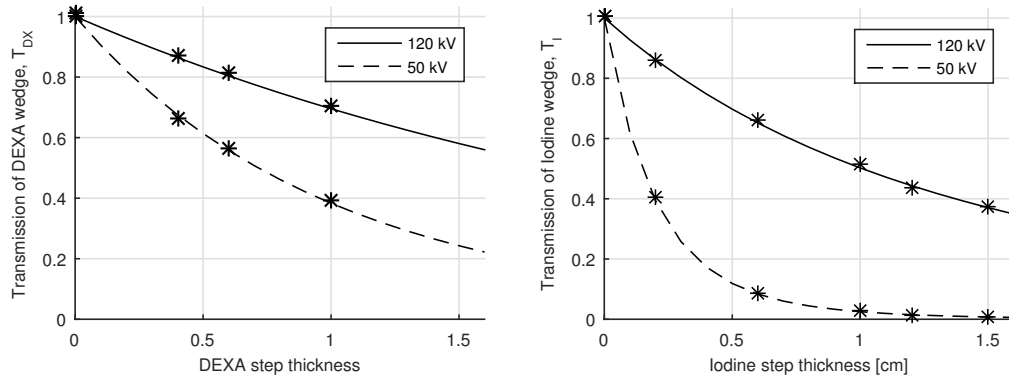
Figure 4.4.1: Transmission of DEXA wedge as a function of DEXA wedge thickness (left).

tor (Xmaru1215CF-MPTM, Rayence Co., Ltd., Korea) with square 49.5 μm elements and 0.5 mm CsI. ESA images were acquired using a fast kV-switching generator (EMD Technologies, Montreal Canada) operating in single-exposure mode with several seconds between high and low-energy exposures. The ESA images were acquired using low kV of 50, 60, and 70 kV and a fixed high kV of 120 kV with 2.5 mm of copper filtration.

We assess the tubing used is water equivalent by filling the tube with water, then submerging the tube in water and acquiring images of the tubing at 50, 80, and 110 kV. We excluded the tubing that was visible compared to the background in the image. We attached small lead pieces to the end of each tube. For the tubes that we could not see we took an image profile in the x-direction of the image near the lead strip and plot it against the pixel values of the image. We used Amber Natural Latex Tubing with 1/8" inner diameter (I. D.) and wall thickness of 1/32".

4.4 Results

Fig. 4.4.1 on the left shows the DEXA wedge transmission factor as a function of DEXA wedge thickness and, similarly, the iodine transmission factor as a function of iodine-filled wedge thickness. The purpose was to confirm the mass loading of the DEXA wedge material and show that the theoretical calculation agrees with our experiment. We also con-
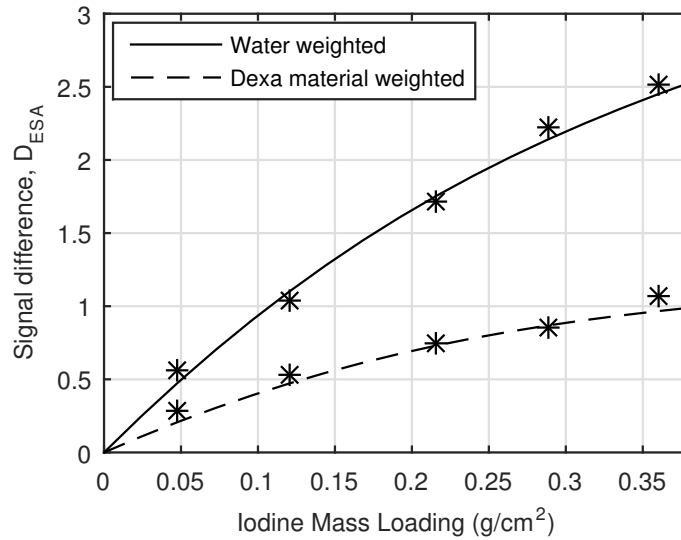
Figure 4.4.2: ESA signal as a function of the iodine mass loading using water weighted and DEXA material weighted with 0 bone thickness.

firmed the mass loading of iodine for different thicknesses of iodine-filled stepwedge.

Fig. 4.4.2 shows the difference of iodine signal with soft tissue removal is a factor of 2.6 compared to that with cortical bone removal. This suggests that in order to achieve the best contrast for iodine, soft-tissue must be removed from the image. Our experimental points show excellent agreement with our theoretical calculation.

Fig. 4.4.3 shows an example of ESA images with iodine stepwedge superimposed on DEXA stepwedge for optimal soft-tissue weighted removal and weighted for cortical bone removal. This shows that removing soft-tissue has preserved the iodine signal but kept the DEXA wedge signal in the image, while the DEXA wedge cancellation only cancels out thin DEXA material, increases image noise, and improperly subtracts low iodine signal. This confirms that soft-tissue suppression is best to preserve iodine signal with partial subtraction of DEXA material.

Figure 4.4.4a) shows a conventional (single kV at 80 kV, 330 μGy) angiographic image of the RANDO anthropomorthic phantom with a 2-cm thick water overlay containing iodine-filled tubing similar to what would be acquired in a coronary angiographic examination. The three horizontal lines that cross the image are part of the phantom layered

60/120 kV

$w = 0.71$

$w = 0.30$
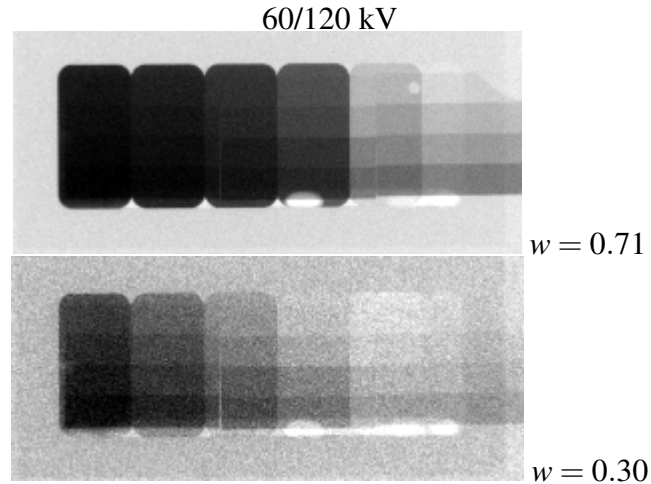
Figure 4.4.3: Images showing DEXA stepwedge superimposed on iodine stepwedge for optimal soft-tissue cancellation (top) and thin DEXA wedge cancellation (bottom).

construction and may be ignored for this study.

For comparison, ESA images of the same phantom are shown in Fig. 4.4.4b) to f). We used similar exposures of 293 μGy to make this comparison and calculated using different weighting factors. The lower weight of 0.2 suppresses bone-mimicking material from the dual-energy image, but also suppresses the iodine signal. The weights 0.5 and 0.55 partially suppress the bone material well while preserving the iodine signal, and weights 0.60 and 0.80 preserve the iodine signal, although less than weights of 0.5 and 0.55. Despite 0.71 being the optimal weight for the iodine SNR at 60 and 120 kV with 2.5 mm copper, for imaging a three material composition of iodine, water, and bone, a weight of 0.5 is a good compromise in preserving iodine signal and partially suppressing bone. Having bone in the image may be beneficial for landmarking.

4.5   Discussion

We confirmed that the DEXA material has a density of 1.82 g cm^{-3} and we show the experimental calculation of transmission factor for DEXA is in excellent (close) agreement theoretical calculations for all thicknesses. Similarly with iodine we confirmed that the

Figure 4.4.4: a) Conventional single-kV (80 kV) contrast image of RANDO anthropomorphic phantom and thin slab of water containing iodine-filled tubing. b)...f) ESA images at 60/120 kV with 2.5 mm copper for 120 kV using different weighting factors. The optimal weight appears to be approximately 0.55.

mass attenuation coefficient is 0.24 g cm^{-3}and we show the experimental calculation of transmission factor for iodine is in excellent agreement theoretical calculations for all step-wedge thicknesses.

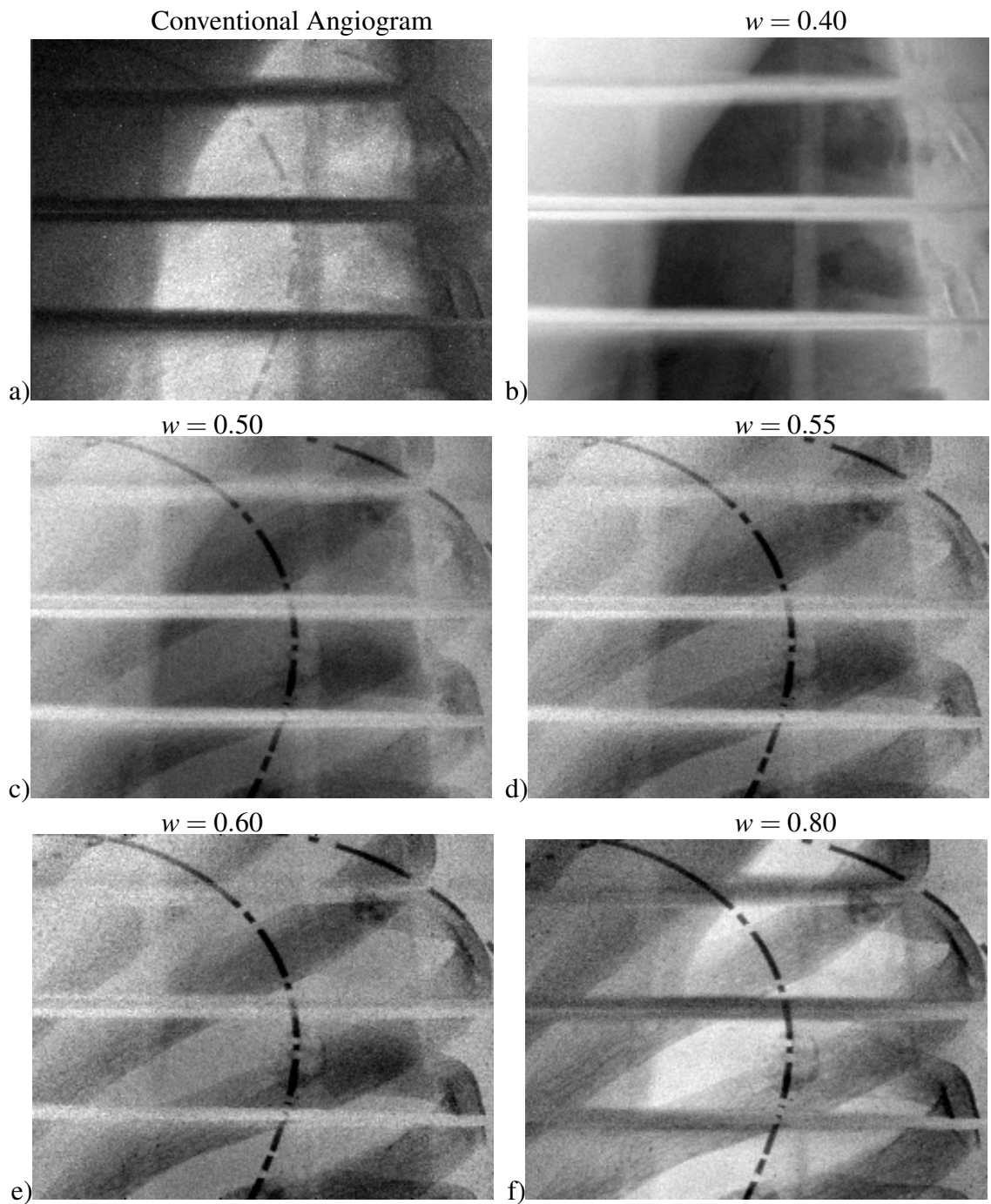We show that soft-tissue suppression will preserve the iodine signal while weighting to remove cortical bone will suppress the thin DEXA steps only and increase image noise. Removing soft-tissue rather than bone would be better for iodine signal.

We have shown with the RANDO phantom that different weights affect how well iodine and bone-mimicking material can be visually seen in the image. With a weight of 0.2 the iodine signal appears to be completely suppressed along with the bone-mimicking material, but as the weight increases both iodine and bone signal appear in the image. Weights of 0.5 and 0.55 preserve the iodine signal and show better suppression of bone compared to images with weights of 0.6 and 0.8. We suggest that for 60 and 120 kV that a weight of 0.5 or 0.55 be used for imaging a three material composition. We show the benefits of dual-energy imaging compared to a single kV image of the RANDO vascular phantom where in the single kV image the iodine signal shows little contrast to the background.

The next step in this project is to implement our fast-kV switching x-ray machine to demonstrate ESA in real-time.

4.6   Conclusion

We show excellent agreement was obtained between theoretical and experimental calculation of transmission factor for DEXA wedge material at different thicknesses. We show that when using bone weighted ESA images the iodine signal decreases compared to soft-tissue subtraction. We show that iodine signal is very low with DEXA wedge signal cancellation for thin DEXA wedge thicknesses of 0.1 and 0.4 cm, and in practice we show that these ESA images will appear quite noisy compared to soft-tissue weighted ESA images. We show that with an anthropomorphic phantom that ESA removes soft-tissue and partially

removes bone-mimicking material compared to a conventional single kV image. We made the following conclusions:

1. The soft-tissue weighted image is optimal for preserving iodine signal, partial bone removal (particularly thin bone), and ESA image noise.

2. Optimal image weights - ratio of high to low water mass attenuation coefficients - for low kV of 50, 60, and 70 kV is 0.67, 0.71, 0.74, respectively.

We conclude that for a 3 material composition of iodine, water, and bone, water is the material that needs to be removed. In a future study we plan to consider addressing performing ESA in real-time similar to fluoroscopy for cardiac imaging. With implementation of fast kVp-switching x-ray machine ESA may reduce motion artifacts for vascular imaging. We have already shown in previous studies[218, 216] that technical requirements may be the reason that early investigations of dual-energy angiography were less successful and now that we have optimized those parameters.

4.7 References

[212] H. Atak and P. M. Shikhaliev. Dual energy ct with photon counting and dual source systems comparative evaluation. *Institute of Phys. and Eng. in Med.*, 60:8949–8975, 2015.

[213] Y. Bentoutou, N. Taleb, A. Bounoua, and C. Serief. A results recapitulation of image registration techniques in digital subtraction angiography. *Institute of Electrical and Electronics Engineers Nuclear Science Symposium Conference Record*, 2008.

[214] Y. Bentoutou, N. Taleb, M. Chikr El Mezouar, M. Taleb, and L. Jetto. An invariant approach for image registration in digital subtraction angiography. *Pattern Recognition in Information Systems*, 35:2853– 2865, 2002.

[215] A. E. Burgess. The rose model, revisited. *J Opt Soc Am A*, 16(3):633–646, 1999.

[216] C. S. Burton, J. R. Mayo, and I. A. Cunningham. Energy subtraction angiography can compete with digital subtraction angiography in terms of image snr. Submitted.

[217] C. S. Burton, J. R. Mayo, and I. A. Cunningham. Optimizing iodine snr for a given exposure in terms of the ratio of number of interacting photons to determine parameters needed for dual-energy subtraction methods. Submitted.

[218] C. S. Burton, J. R. Mayo, and I. A. Cunningham. Theoretical and experimental comparison of image signal and noise for dual-energy subtraction angiography and conventional x-ray angiography. *SPIE Med. Imag.*, 9412(19), 2015.

[219] C. S. Burton, J. R. Mayo, and I. A. Cunningham. Theoretical comparison of image signal and noise for dual-energy subtraction angiography and conventional x-ray angiography. *Medical Imaging*, 2015.

[220] A.-K. Carton, C. Ullberg, K. Lindman, R. Acciavatti, T. Francke, and A. D. A. Maidment. Optimization of a dual-energy contrast-enhanced technique for a photon-counting digital breast tomosynthesis system: I. a theoretical model. *Med. Phys.*, 37(11):5896–5907, 2010.

[221] I. A. Cunningham and R. Shaw. Signal-to-noise optimization of medical imaging systems. *The Journal of the Optical Society of America*, 16(3):621–632, 1999.

[222] J. L. Ducote and S. Molloi. Quantification of breast density with dual energy mammography a simulation study. *Med. Phys.*, 35(12):5411–5418, 2008.

[223] E. Forster. *Equipment for Diagnostic Radiography*. MTP Press Limited Falcon House Lancaster, England, 1985.

[224] M. Fukao, K. Kawamoto, H. Matsuzawa, O. Honda, T. Iwaki, and T. Doi. Optimization of dual-energy subtraction chest radiography by use of a direct-conversion flat-panel detector system. *Radiol. Phys. Technol.*, 8(1):46–52, 2015.

[225] P. Hua and I. Fram. Feature-basedimage registration for digital subtraction angiography. *International Society for Optics and Photonics*, 1898:24–31, 1993.

[226] F. Kelcz, P. M. Joseph, and S. K. Hilal. Noise considerations in dual energy ct scanning. *Med. Phys.*, 6(5):418–426, 1979.

[227] Andoh K Kinno Y, Odagiri K. Gadopentetate dimeglumine as an alternative contrast material for use in angiography. *Am J Roentgenology*, 160:1293–1294, 1993.

[228] M. P. Kowalski, G. G. Fritz, R. G. Cruddace, A. E. Unzicker, and N. Swanson. Quantum efficiency of cesium iodide photocathodes at soft x-ray and extreme ultraviolet wavelengths. *Appl. Opt.*, 25(14):2440, 1986.

[229] X. Liu, L. Yu, A. N. Primak, and C. H. McCollough. Quantitative imaging of element composition and mass fraction using dual-energy ct: Three-material decomposition. *Med. Phys.*, 35(5):1602–1609, 2009.

[230] B. K. Nallamothu, E. R. Bates, Y. Wang, E. H. Bradley, and H. M. Krumholz. Driving times and distances to hospitals with percutaneous coronary intervention in the united states: implications for prehospital triage of patients with st-elevation myocardial infarction. *Circulation*, 7(1):1189–1195, 2006.

[231] P. Patnaik. *Handbook of Inorganic Chemicals*. McGraw-Hill, 2002.

[232] A. N. Primak, J. C. R. Giraldo, X. Liu, L. Yu, and C. H. McCollough. Improved dual-energy material discrimination for dual-source ct by means of additional spectral filtration. *Med. Phys.*, 36(4):1359–1369, 2009.

[233] M. Remy-Jardin, J. Bahepar, J. J. Lafitte, P. Dequiedt, O. Ertzbischoff, J. Bruzzi, V. Delannoy-Deken, A. Duhamal, and J. Remy. Multi-detector row ct angiography of pulmonary circulation with gadolinium-based contrast agents: prospective evaluation in 60 patients. *Radiology*, 238(3):1022–1035, 2006.

[234] S. Richard and J. H. Siewerdsen. Optimization of dual-energy imaging systems using generalized neq and imaging task. *Med. Phys.*, 31(1):127–139, 2007.

[235] A. Rose. A unified approach to the performance of photographic film, television pickup tube, and the human eye. *Journal of the Society of Motion Picture Engineers*, 1946.

[236] A. Rose. The sensitivity performance of the human eye on an absolute scale. *Journal of the Optical Society of America*, 1948.

[237] V. M. Runge, J. A. Clanton, C. M. Lukehart, C. L. Partain, and A. E. James. Paramagnetic agents for contrast-enhanced nmr imaging: a review. *Am J Roentgenol*, 141(6):1209–1215, 1983.

[238] J. M. Sabol, G. B. Avinash, F. Nicolas, B. Claus, J. Zhao, and J. T. Dobbins. The development and characterization of a dual-energy subtraction imaging system for chest radiography based on csi:ti amorphous silicon flat-panel technology. *SPIE Med. Imag.*, 4320:399–409, 2001.

[239] M. Saito. Spectral optimization for measuring electron density by the dual-energy computed tomography coupled with balanced filter method. *Med. Phys.*, 36(8):3631–3642, 2009.

[240] E. Samei and R. S. Saunders Jr. Dual-energy contrast-enhanced breast tomosynthesis optimization of beam quality for dose and image quality. *Phys. Med. Biol.*, 56(19):6359–6378, 2011.

[241] N. A. Shkumat, J. H. Siewerdsen, S. Richard, N. S. Paul, J. Yorkston, and R. Van Metter. Dual-energy imaging of the chest: Optimization of image acquisition techniques for the bone-only image. *Med. Phys.*, 35(2):629–632, 2008.

[242] M. Spahn, V. Heer, and R. Freytag. Flat-panel detectors in x-ray systems. *Radiology*, 43:340–350, 2003.

Lawrence M. Boxt Stephen Wilmot Miller and Suhny Abbara. Cardiac imaging.

[243] FRCR T Albrecht, MD and FRCR P Dawson, PhD. Gadolinium-dtpa as x-ray contrast medium in clinical studies. *The British Journal of Radiology*, 73:878–882, 2000.

[244] D. M. Tucker, G. T. Barnes, and D. P. Chakraborty. Semiempirical model for generating tungsten target x-ray spectra. *Medical Physics*, 18(2):211–218, 1991.

[245] PhD Barbara ElmstÃ¥hl-MD-Peter Leander MD PhD Mats Nilsson PhD Klaes Golman PhD Torsten AlmeÂŽn MD PhD Ulf Nyman, MD. Are gadolinium-based contrast media really safer than iodinated media for digital subtraction angiography in patients with azotemia? *Radiology*, 223:311–318, 2002.

[246] R. F. Wagner and D. G. Brown. Overview of a unified snr analysis of medical imaging systems. *IEEE Trans. Med. Imaging*, 1:210–213, 1982.

[247] Y. Yao, A. S. Wang, and N. J. Pelc. Efficacy of fixed filtration for rapid kvp-switching dual energy x-ray systems. *Med. Phys.*, 41(3):1–12, 2014.

[248] L. Yu, J. A. Christner, S. Leng, J. Wang, J. G. Fletcher, and C. H. McCollough. Virtual monochromatic imaging in dual-source dual-energy ct: radiation dose and image quality. *Med. Phys.*, 38(12):6371–6379, 2011.

[249] L. Yu, A. N. Primak, X. Liu, and C. H. McCollough. Image quality optimization and evaluation of linearly mixed images in dual-source, dual-energy ct. *Med. Phys.*, 36(3):1019–1024, 2009.

Chapter 5

Conclusions

A Rose model analysis was developed to compare the iodine $\mathrm{SNR}/\sqrt{\mathscr{K}}$ in images obtained using DSA (80 kV) and ESA (energy subtraction, 50 and 120 kV with 2.5 mm Cu filtration with the high energy beam) methods. Excellent agreement was obtained between theoretical and experimental iodine Rose $\mathrm{SNR}/\sqrt{\mathscr{K}}$ in both DSA and ESA images over a range of iodine concentrations. It is shown that ESA and DSA can produce images with similar iodine SNR for the same phantom entrance exposure, but ESA requires a higher-performing detector to produce near-optimal images. There are specific conclusions made from our first study. First, ESA imaging requires a detector with good quantum efficiency at a higher energy (120 kV) than DSA. This generally means a thicker absorption layer. For a CsI detector, the CsI should be 0.5 mm or more to achieve near-optimal images, although the benefits above 0.3 mm are modest for both DSA and ESA. Second, ESA imaging requires a detector with much lower readout noise than DSA, expressed here as a quantum-limit exposure (where readout noise variance equals quantum noise variance). It is shown that near-optimal results are obtained only with a detector having a 50-keV quantum-limit exposure of 0.05 μGy (detector air KERMA) or lower for the exposure conditions used in this study, and 0.005 μGy or lower for exposure conditions used by early investigators who have studies dual-energy angiography previously. These are both substantially lower than

many state-of-the-art aSi panels in use today. Lastly, ESA imaging is more susceptible to x-ray scatter than DSA. The scatter-to-primary ratio must be 0.05 or less to achieve near optimal results. Overall we conclude that ESA can provide images with similar SNR to DSA with the same patient exposure today. The limitations in this study were not considering noise in the iodine region (sum-of-variance iodine SNR/$\sqrt{\mathscr{K}}$ model), tube heat loading considerations, and addressing imperfect background suppression. We believe the challenging technical requirements outlined here may be the reason that early investigations of dual-energy angiography were less successful.

In a subsequent study we added noise in the iodine signal to the total noise component part of the image into our theoretical and experimental calculations. The optimization of our Rose and sum-of-variance model for ESA for fixed high kV of 120 kVp (2.5 mm Cu filtration) and for low kVps of 50, 60, and 70 kV and for patient thicknesses of 2-30 cm. Excellent agreement was obtained between theoretical and experimental iodine Rose SNR/$\sqrt{\mathscr{K}}$ for ESA images over a range of mAs ratios for a patient thickness of 20 cm. We identified the detector material, from detectors that are currently available, that will yield the best possible iodine SNR/$\sqrt{\mathscr{K}}$. We have also identified that heat loading may be a minor limitation. There are specific conclusions made from this study. First, for each water thickness of 2-30 cm, ESA can produce images with similar iodine SNR/$\sqrt{\mathscr{K}}$ for mAs ratio of 1.0 for 50/120 and 60/120 and 0.3 for 70/120 with 2.5 mm copper. The low kVps that will give the best possible iodine SNR/$\sqrt{\mathscr{K}}$ range from 50-60 kVp for a fixed high kVp of 120 kV (2.5 mm copper filter). Second, heat units for ESA were estimated to be a factor of 2 greater than DSA, therefore the number of images acquired during an ESA procedure is estimated to be half that of DSA. This limitation may only be minor or may be overcome with implementation of fast kVp-switching x-ray system where, unlike a DSA procedure, the motion artifacts may be removed and therefore the procedure would not need to be redone. We expect that ESA in real-time will eliminate motion artifacts and therefore the number of images needed for a procedure will be significantly less than that of

DSA. Third, ESA requires detector materials, like CsI and GdO, for example, to achieve the best possible of iodine Rose $\text{SNR}/\sqrt{\mathscr{K}}$ with thicknesses of 300-500 μm. Current detector technology may be used to achieve optimal iodine $\text{SNR}/\sqrt{\mathscr{K}}$.

We conclude that ESA can provide images with similar $\text{SNR}/\sqrt{\mathscr{K}}$ to DSA with the same patient exposure. With implementation of fast kVp-switching x-ray machine ESA may reduce motion artifacts for cardiac application and other applications of vascular imaging. We believe the challenging technical requirements outlined here may be the reason that early investigations of dual-energy angiography were less successful.

The transmission factor of DEXA material was added to our ESA signal. Excellent agreement was obtained between theoretical and experimental calculation of transmission factor for DEXA wedge material at different thicknesses. We show that when using bone weighted ESA images the iodine signal decreases compared to soft-tissue subtraction. We show that iodine signal is very low with DEXA wedge signal cancellation for thin DEXA wedge thicknesses of 0.1 and 0.4 cm, and in practice we show that these ESA images will appear quite noisy compared to soft-tissue weighted ESA images. We show that with an anthropomorphic phantom that ESA removes soft-tissue and partially removes bone-mimicking material compared to conventional single kV image. We made the following conclusions from the final study in this thesis. First, the soft-tissue weighted image is optimal for preserving iodine signal, partial bone removal (particularly thin bone), and ESA image noise. Second, optimal image weights - ratio of high to low water mass attenuation coefficients - for low kV of 50, 60, and 70 kV is 0.67, 0.71, 0.74, respectively. Third, ESA has the potential to improve visibility of diseased coronary arteries compared to conventional non-subtraction approaches

We conclude that for a three material composition of iodine, water, and bone, water is the material that needs to be removed. In a future study we plan to consider addressing performing ESA in real-time similar to fluoroscopy for cardiac imaging. With implementation of fast kVp-switching x-ray machine ESA may reduce motion artifacts for vascular

imaging. We have already shown in a previous studies that technical requirements may be the reason that early investigations of dual-energy angiography were less successful and now that we have optimized those parameters.

The long term goal for our work for cardiac imaging is a form of subtraction imaging of the coronary arteries and the results of this thesis suggest that this is possible experimentally. This method has the potential to improve the visibility of arterial stenosis compared to the non-subtraction methods which require higher iodine concentration and high x-ray patient entrance exposure. The next step in this story is to show that ESA images can be acquired in real-time. As discussed in the Future Work section we discuss the possibility of implementing a fast kV-switching x-ray machine.

Chapter 6

Future Work with Preliminary Results

6.1 Implementation of fast kV-switching x-ray system

The next step in this project is to implement ESA in real-time. In this chapter we show preliminary design for this fast kV-switching x-ray machine with fast switching filter design.

In this chapter we show the design of a fast kV-switching machine for demonstrating ESA in real-time. It has been shown that ESA will work with a 2.5 mm copper filter in the high kV beam therefore it is necessary to build a device that will put a copper filter in front of the source aparture. Mistretta[90] and Van Lysel[135] have implemented a fast-kV switcher in the past for cardiac imaging in real time using a spinning disk to filter the high kV beam. However, it was never clear as to how the system was designed or implemented. The goal of this chapter is to describe in detail the design and implementation of the fast kV switching x-ray machine and two designs of fast switching copper filter system.

6.1.1 Solenoid system and filter design

Figure 6.1.1 shows the system design for the fast kV-switching x-ray machine. There is a master-slave dynamic between the PC-generator complex to the filter. The one way and two way arrows indicate a 1 bit and 2 bit connection, respectively. The PC sends instructions
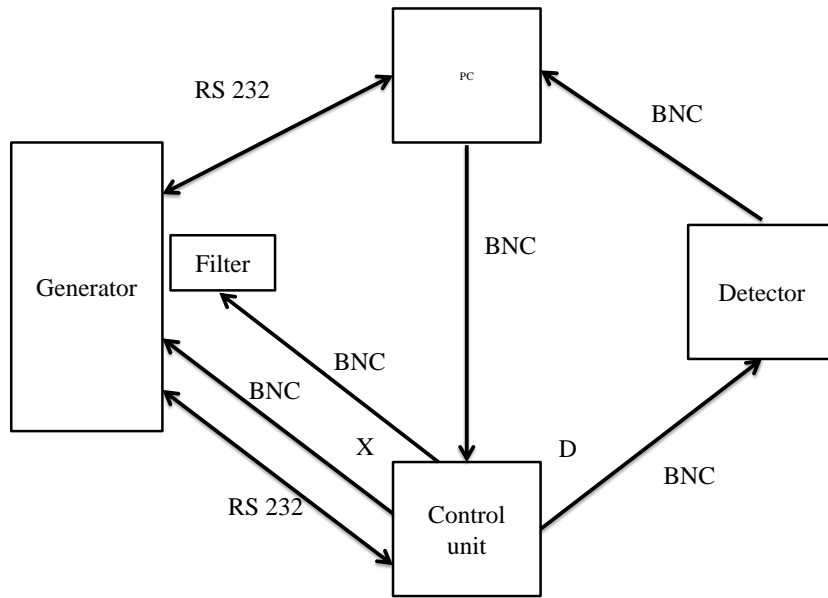
Figure 6.1.1: X-ray system design and setup showing the connection between different components and type of connection between

to the control unit (CU) to send a pulse "D" to the detector to start detector read out. The PC also sends instructions to the CU to send a pulse "X" to trigger the x-rays to turn on and this follows 10 D pulses have been sent to the detector. Software on the PC contains information regarding the time between the kV switch and sends instructions to switch the kV to the generator. The information is sent directly from the PC to the generator to switch the kV settings during the x-ray on time. Because the PC contains information regarding the time of the kV switch, it sends information to the CU to send a pulse "F" to the filter to move into a "ready" position. Fig 6.1.2 shows the timing diagram for our system design. We selected a solenoid to move the filter bi-directionally. Fig 6.1.3 shows the filter design with solenoid. We calculate the mass as follows:

$$m_{Cu} = \rho_{Cu}V_{Cu} \tag{6.1.1}$$
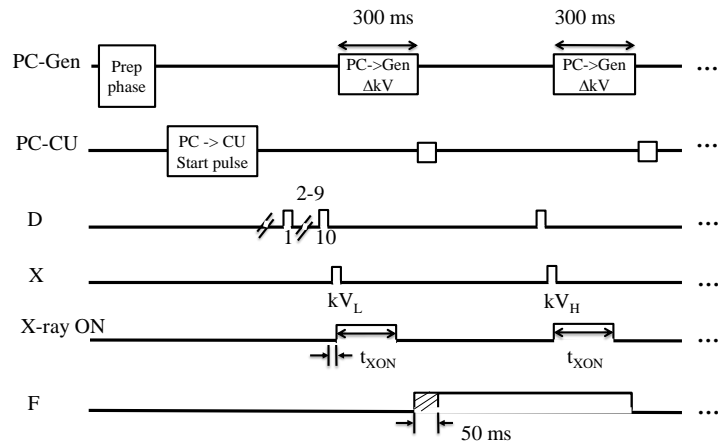
$$= \rho_{Cu}A_{Cu}x_{Cu} \tag{6.1.2}$$

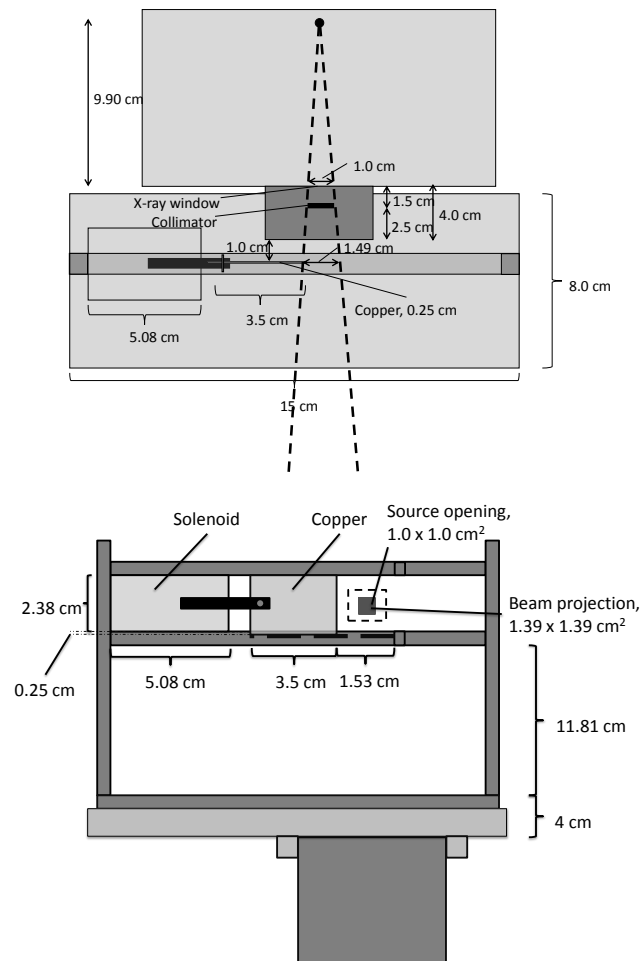Figure 6.1.2: Timing diagram for solenoid filter design

Figure 6.1.3: Solenoid filter design (top) top view and (bottom) front view.

We calculate the acceleration using simple kinematics as follows:

$$d = \frac{1}{2}at^2 \tag{6.1.3}$$

$$a = \frac{2d}{t^2} \tag{6.1.4}$$

We then calculate the force as follows:

$$F = m_{Cu}a \tag{6.1.5}$$

$$= \rho_{Cu}A_{Cu}x_{Cu}a \tag{6.1.6}$$

Our filter is attached to the bars.

6.1.2 Spinning disk system and filter design

Using the same setup as fig. 6.1.1 we can design the spinning disk filter.

Figure 6.1.4 shows the timing diagram for our system design. We turn on the PC and "set phase" indicated that the PC is connected to the generator. The PC then sends a pulse to the CU, and the CU sends a pulse D to the detector. The detector reads out 10 dark images (10 D pulses) and right after the 10th pulse the CU sends pulse X to the generator to start the exposures. The x-rays come on right after the x-ray trigger. During this time the filter is ramping up speed to get to the rpm required and the IR pulse is received at the PC.

Figure 6.1.5 shows the time needed for the kV to change from low to high kV. First the x-rays are triggered and the low kV is turned on, and at the same time instructions are sent from the PC to the generator to switch from low to high kV. The same thing occurs after the second high kV x-ray trigger, the instructions are sent from the PC to the generator to switch from high kV to low kV. The filter is ready when the high kV exposures are on and
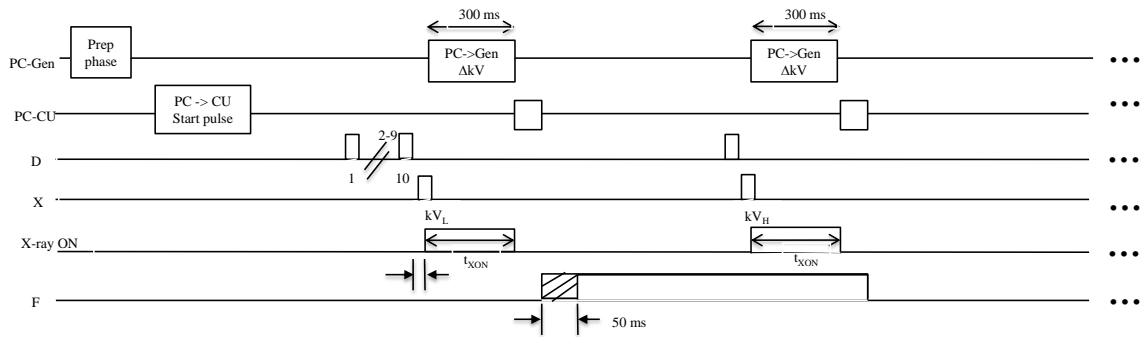
Figure 6.1.4: Timing diagram for system design
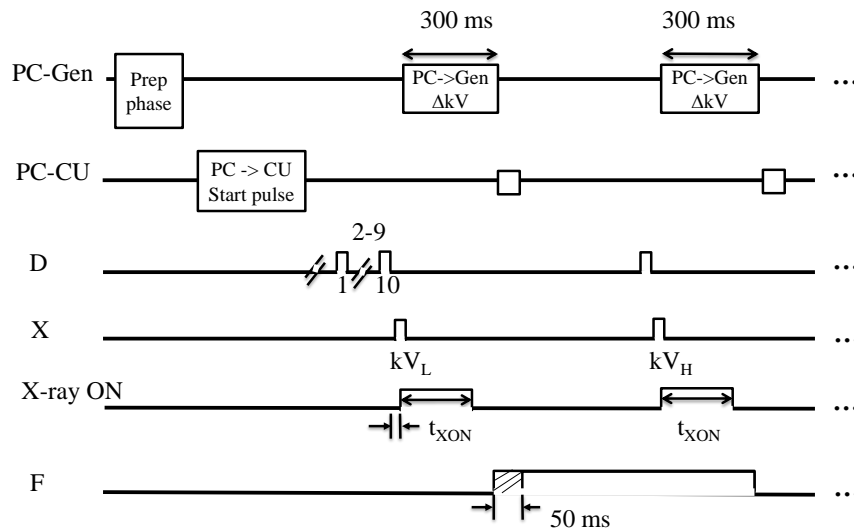
Figure 6.1.5: Timing diagram for filter design

113
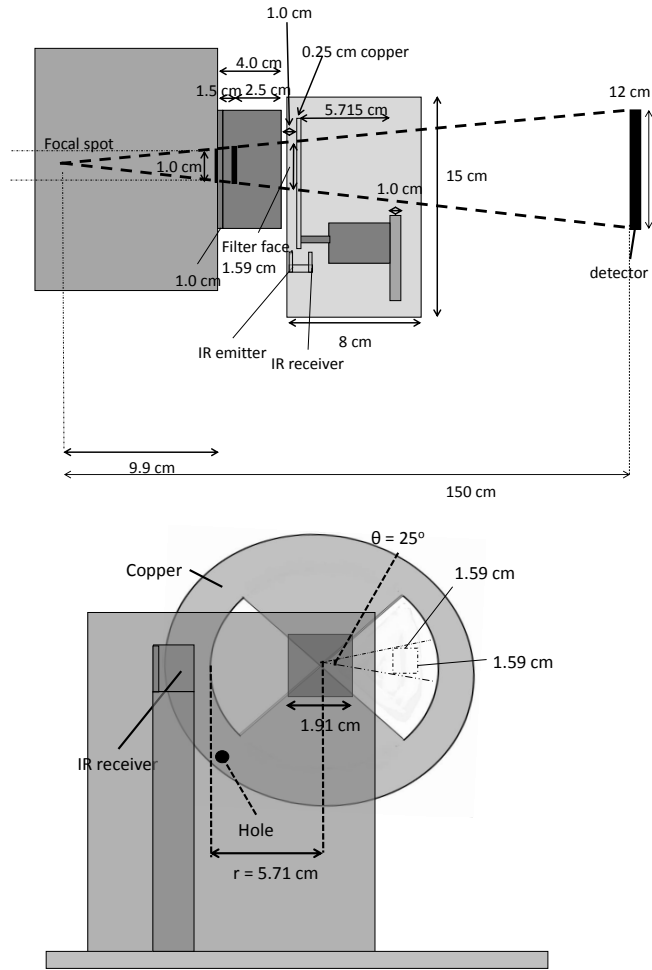
Figure 6.1.6: Sideview and topview of filter design for spinning disk.

transitions from ready to not ready position during the time the two kV are switching.

Figure 6.1.6 shows the side and front view of the filter design. The filter is synchronized to the entire x-ray system. The filter speed is limited by the transition time, the time between the filter in ready vs not read positon,

$$\tau = t_{\triangle kV} - t_{XON} \tag{6.1.7}$$

where τ [ms] is the transition time (indicated in Fig), $t_{\triangle kV}$ [ms] is the time it takes to and t_{XON} [ms] is the x-ray on time. The frame rate is limited to the following,

114

$$FR = \frac{1 \, \text{frame}}{\tau} \tag{6.1.8}$$

where F_R is the frame rate and τ is the transition time. We round down to the next integer to get the limiting frame rate at which our system can operate relative to. There are a few steps to calculating the transition time also limits the angular frequency,

$$r = \frac{S}{\theta} \tag{6.1.9}$$

$$C = 2\pi r \tag{6.1.10}$$

$$N_{\text{slices}} = \frac{C}{z} \tag{6.1.11}$$

$$\theta_{\text{slice}} = \frac{S}{r} \tag{6.1.12}$$

$$\omega_{\text{avg}} = \frac{\theta_{\text{slice}}}{\tau} \tag{6.1.13}$$

The ON and OFF time of the filter is calculated as follows,

$$\triangle t_{\text{OFF}} = \triangle t_{\text{ON}} = \frac{2\theta_{\text{slice}}}{\omega_{\text{avg}}} \tag{6.1.14}$$

The transition time was calculated by subtracting the time for the kV change and the x-ray ON time. Currently our system can change kVp from 50-110 kV in approximately 0.300 sec and therefore the calculations are limited by this time. For a chosen x-ray ON time of 0.0167 sec, our transition time τ can be calculated as follows,

115

$$\tau = 0.300 - 0.0167$$

$$= 0.283 \, \text{s} \qquad (6.1.15)$$

Therefore, our frame rate F_R is calculated as the following,

$$
\begin{aligned}
F_R &= \frac{1 \, \text{frame}}{0.283 \, \text{s}} \\
&= 3.53 \frac{\text{frame}}{\text{s}} \\
&= 3 \frac{\text{frames}}{\text{s}}, \; (\text{rounded down}) \qquad (6.1.16)
\end{aligned}
$$

Therefore the transition time is now limited to 0.33 s. The source aperture dimensions in our case is 1.0×1.0 cm^2 and we have the copper filter surface set up at 1.0 cm from the source opening. Using like triangles we take into account the beam divergence as it reaches the surface of the copper filter, 1.1×1.1 cm^2. These parameters can be used to calculate z using the Pythagorean theorem to find the minimum distance that needs to be accounted for when calculating the arc length of the two copper areas.

$$z = \sqrt{2} \times 1.59 \qquad (6.1.17)$$

$$\approx 2.24 \, \text{cm}$$

We design for the arc length to be a bit larger than 1.6 cm, and we add 0.2 cm to ensure full coverage. Each copper area has an angular displacement of $\frac{\pi}{2}$ therefore we can calculate radius of the filter as the following,

$$r = \frac{4 \times 2.24}{\frac{\pi}{2}} \tag{6.1.18}$$

$$= 5.71 \, \text{cm} \tag{6.1.19}$$

Therefore the circumference of the circle is calculated as,

$$C = 2\pi (5.71) \tag{6.1.20}$$

$$= 28.8 \, \text{cm} \tag{6.1.21}$$

If the calculations are correct then the number of equal slices is 16.

$$N_{\text{slice}} = \frac{28.8 \, \text{cm}}{1.8 \, \text{cm}}$$

$$= 16 \tag{6.1.22}$$

and the angle of each slice should be $\frac{\pi}{8}$

$$\begin{aligned} \theta_{\text{slice}} &= \frac{S_{\text{slice}}}{r} \\ &= \frac{\frac{2\pi r}{N_{\text{slice}}}}{r} \\ &= \frac{2\pi}{N_{\text{slice}}} \\ &= \frac{\pi}{8} \, \text{rad} \end{aligned} \tag{6.1.23}$$

Based on the transition time we can now calculate the angular frequency of the filter as the following,
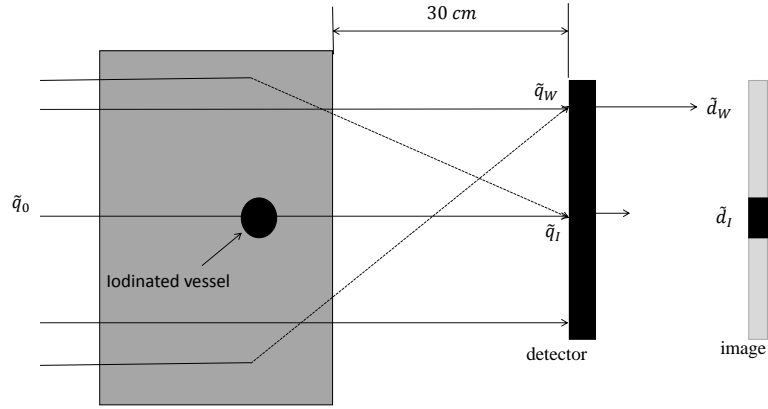
Figure 6.1.7: Schematic illustration of iodine-filled step-wedge immersed in 20 cm of water with an incident spectrum $\widetilde{q}_o$ [quanta mm^{-2}], and interacting spectra $\widetilde{q}_W$ and $\widetilde{q}_I$, and pixel values $\widetilde{d}_W$ and $\widetilde{d}_I$, in water and iodinated regions of the image respectively.

$$
\begin{aligned}
\omega_{\text{avg}} &= \frac{\theta_{\text{slice}}}{\tau} \\
&= \frac{\frac{\pi}{8}\,\text{rad}}{0.33\,\text{s}} \\
&= 1.19\,\frac{\text{rad}}{\text{s}} \\
&= 11.4\,\text{rpm}
\end{aligned}
\tag{6.1.24}
$$

The ready ON and ready OFF times of the filter are used to check the calculation as follows,

$$
\begin{aligned}
\triangle t_{\text{OFF}} &= \triangle t_{\text{ON}} = \frac{\triangle \theta}{\omega_{\text{avg}}} \\
&= \frac{\frac{\pi}{4}\,\text{rad}}{1.19\,\frac{\text{rad}}{\text{s}}} \\
&= 0.66\,\text{s}
\end{aligned}
\tag{6.1.25}
$$

Our phantom set up is shown in fig 6.1.7. We attach the water-equivalent tubing to the

Copper	
ρ_{Cu}	8.96 g cm^{-3}
A_{Cu}	3x3 cm^2
x_{Cu}	0.25 cm

Table 6.1: Specifications for copper

Parameters	
d	1.6 cm
t	0.050 s

Table 6.2: Stroke length and transition time

pulsatile pump. We pump the iodine through the tubing at the same frame rate. We fill the tubing with water and then inject iodine in the tube and acquire images at that frame rate. We validate that the tubing used is water equivalent by filling the tube with water, then submerging the tube in water and acquiring images of the tubing at 50, 80 and 110 kV. We tested several types of tubing and if the tubing does not show up in the images then we can conclude that the tubing is water equivalent. We attached little pieces of lead onto each tube and took the contrast between the tubing and the background. If the tubing did not show up in the image then the small lead strip would indicate where the tubing would be.

6.1.3 Future filter design and experiment setup

Table 6.1 shows the specifications for the copper filter.

Table 6.2 shows the parameters for the stroke length and transition time of the copper filter.

Fig 6.1.7 illustrates the experiment setup to simulate a real patient. We attach tubing to the pulsatile pump where the iodine is pumped through the tubing at less than the frame rate. We fill the tubing with water and then inject iodine and gadolinium in the tube and acquire images with a frame rate of 3 frames/s. For iodine we acquired images of the vascular phantom at 50 and 110 kV, and the high kV was filtered with 2.5 mm of copper.

We assess the tubing used is water equivalent by filling the tube with water, then submerging the tube in water and acquiring images of the tubing at 50, 80 and 110 kV. We excluded the tubing that was visible compared to the background in the image. We attached small lead pieces to the end of each tube. For the tubes that we could not see we took an image profile in the x-direction of the image near the lead strip and plot it against the pixel values of the image. We used Amber Natural Latex Tubing with 1/8 inner diameter (I. D.) and wall thickness of 1/32". Once the device has been tested on a phantom, the next step would be to do animal testing.

6.2 Gadolinium as an ESA Contrast Agent

We have shown iodine SNR per root air KERMA for ESA is comparable to that of DSA and we have shown that ESA images have partial bone suppression. Since the purpose of dual-energy is to exploit the k-edge of the iodine contrast agent, an alternative solution is to use a contrast agent with similar characteristics to iodine but with a k-edge that occurs at a higher kV. Gadolinium that was introduced in the early 1980's to the clinic as a contrast agent in the form of chelates for MR imaging.[263] It was also noticed that gadolinium's radiodensity allows the chelates to be used as radiographic contrast agents. [256, 250] Gadolinium chelates offer an alternative to iodinated contrast in patients with anaphylactic responses or requiring subsequent administration of radioiodide in the setting of thyroid disease. However, there are several significant drawbacks to gadolinium usage as a radiographic contrast agent, including nephrotoxicity at clinically relevant doses, cost and relatively poor x-ray attenuation at 'safe doses'.[259] Recent reports regarding nephrogenic systemic fibrosis also limit the routine use of gadolinium in patients with renal insufficiency.[261] Gadolinium chelates contain one gadolinium atom per molecule, whereas low-osmolality, non-ionic iodinated contrast agents contain three iodine atoms per monomer. At the photon energies used for DSA, the attenuation produced by a single atom
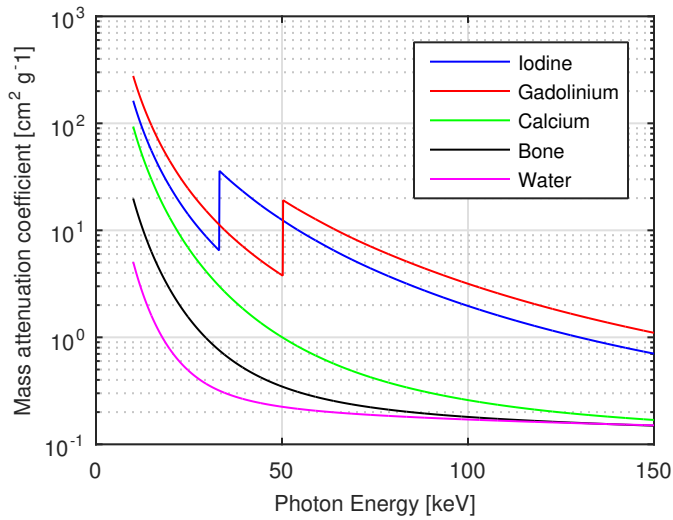
Figure 6.2.1: Mass attenuation coefficients

of gadolinium is roughly half that of an atom of iodine.[257] In this chapter we analyze gadolinium SNR per root air KERMA and compare it to iodine SNR per root air KERMA.

Fig 6.2.1 shows the mass attenuation coefficient for iodine, gadolinium, calcium, corticol bone, and soft-tissue (water). The k-edge for gadolinium is at 50 keV and it is a factor of 2 lower than iodine.

Fig. 6.2.2 shows the gadolinium $SNR/\sqrt{K}$ as a function of low kV for a fixed high kV of 120 kV and low gadolinium mass loading of 0.048 g cm^{-2}. Selecting a low kV of 75-90 kV will yield optimal or near optimal image quality.

Fig. 6.2.3 shows the gadolinium $SNR/\sqrt{K}$ as a function of mAs ratio for fixed low and high kV of 70 and 120 kV, respectively, and low gadolinium mass loading of 0.048 g cm^{-2}. Selecting an mAs ratio of 0.3 will yield optimal or near optimal image quality.

Fig. 6.2.4 shows the spectra used in our theoretical calculations.

6.2.1 Results

Fig. 6.2.5 shows the gadolinium and iodine $SNR/\sqrt{K}$ as a function of mass loading and found that iodine Rose $SNR/\sqrt{K}$ is a factor of 6 greater than gadolinium Rose $SNR/\sqrt{K}$,
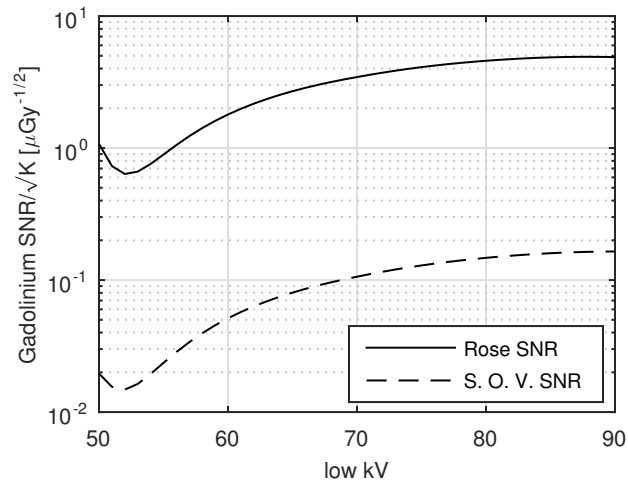
Figure 6.2.2: Gadolinium$SNR/\sqrt{K}$ as a function of low kV for a gadolinium mass loading of 0.048 g cm^{-2}for a fixed high kV of 120 kV.

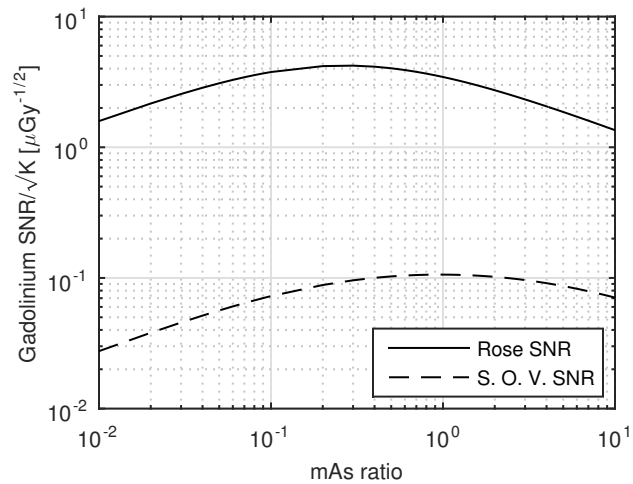

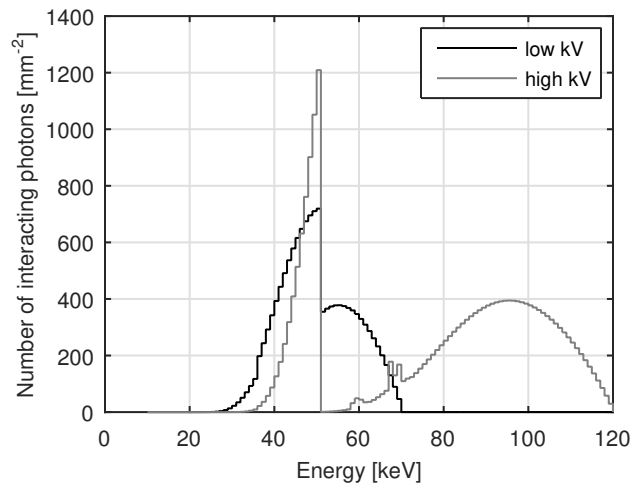Figure 6.2.3: Gadolinium SNR as a function of mAs ratio (low/high)

Figure 6.2.4: Energy spectra of x-ray photons interacting in detector used for ESA calculations (0.5-mm CsI, 20-cm water, 150-cm source-image distance). with low and high-kV spectra (50 and 120 kV, 20 mAs each, 2.5 mm Cu high-kV filter).
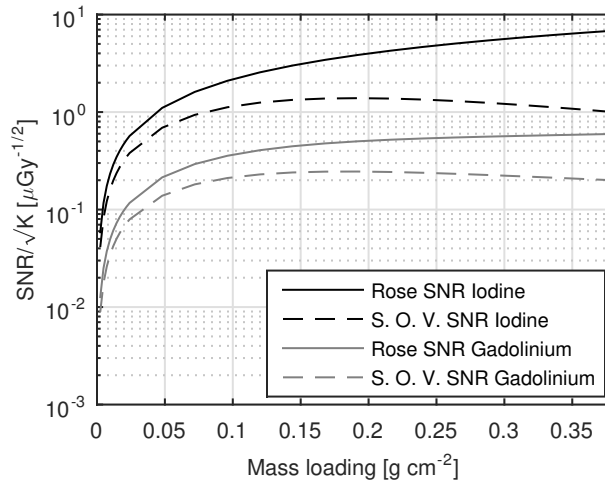

Figure 6.2.5: Plot showing the iodine and gadolinium SNR as a function of mass loading
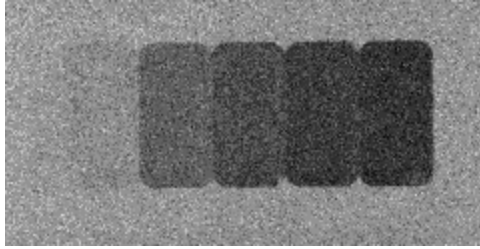
Figure 6.2.6: Image of gadolinium-filled stepwedge with uniform background
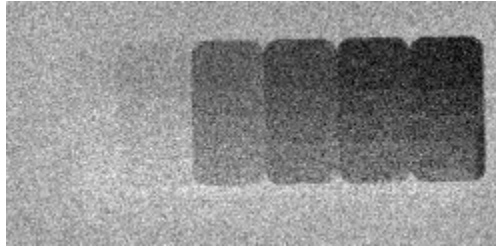
Figure 6.2.7: Image of gadolinium-filled stepwedge with non-uniform background

and iodine S. O. V. $\mathrm{SNR}/\sqrt{K}$ is also a factor of 6 greater than gadolinium S. O. V. $\mathrm{SNR}/\sqrt{K}$ for the same mass loadings.

Fig. 6.2.6 show gadolinium-filled stepwedge showing that signal from low gadolinium mass loading does not have good contrast with the background, and the image is quite noisy.

Fig. 6.2.7 show gadolinium-filled stepwedge showing removal of PMMA stepwedge in the background, and again this image shows poor contrast between signal of low gadolinium mass loading and the background.

Figure 6.2.8: Dual-energy images of gadolinium-filled stepwedge each next to a cylinder of calcium with a 3 cm radius with soft-tissue removal (left) and bone-removal (right).

Fig. 6.2.8 shows dual-energy image of gadolinium stepwedge next to a cylinder of calcium with a 3 cm radius. The soft-tissue weighted ($w = 0.74$) image partially subtracts the calcium cylinder and the bone-weigh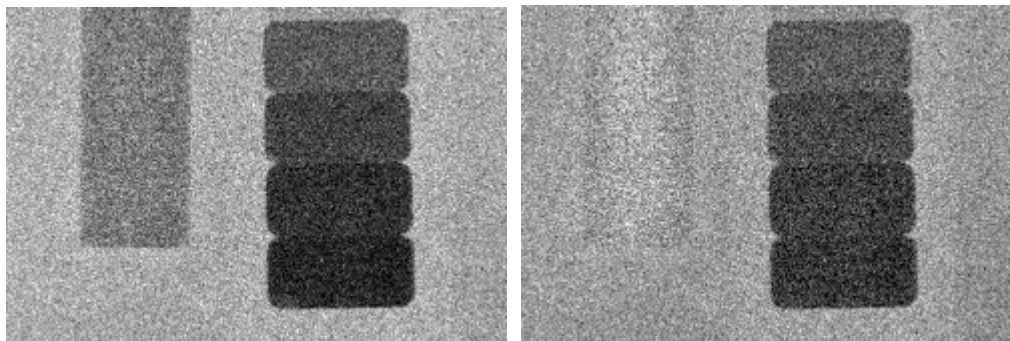ted ($w = 0.60$) suppresses the calcium quite well, however in the bone-weighted image the signal from the thin gadolinium-filled step does not give good contrast compared to the background and the image is noisy. Using k-edge subtraction would yield poorer contrast because the difference between the mass attenuation coefficients at the mean energies would yield a difference comparable to the difference in water.

6.2.2 Conclusion

We conclude that gadolinium as a contrast agent would not be useful for low gadolinium in dual-energy angiography. Iodine is a better choice for contrast agent compared to gadolinium.

6.3 References

[250] T. Albrecht and P. Dawson. Gadolinium-DTPA as x-ray contrast medium in clinical studies. *The British Journal of Radiology*, 73(872):878–882, 2000.

[251] John R Mayo Christiane S Burton and I. A. Cunningham. Theoretical comparison of image signal and noise for dual-energy subtraction angiography and conventional x-ray angiography. *Med Img*, 2015.

[252] I. A. Cunningham and R. Shaw. Signal-to-noise optimization of medical imaging systems. *J. Opt. Soc. Am. A*, 16(3):621–632, 1999.

[253] G. T. Barnes D. M. Tucker and D. P. Chakraborty. Semiempirical model for generating tungsten target x-ray spectra. *Medical Physics*, 18(2):211–218, 1991.

[254] P M Joseph F Kelcz and S K Hilal. Noise considerations in dual energy ct scanning. *Med Phys*, 6(5):418–426, 1979.

[255] Francois Nicolas Bernhart Claus Jianguo Zhao John M. Sabol, Gopal B. Avinash and James T. Dobbins. The development and characterization of a dual-energy subtraction imaging system for chest radiography based on csi:ti amorphous silicon flat-panel technology. *SPIE.Medical Imaging*, 4320:399–409, 2001.

[256] Y. Kinno, K. Odagiri, and K. Andoh. Gadopentetate dimeglumine as an alternative contrast material for use in angiography. *Am J Radiol*, 160:1293–1294, 1993.

[257] P. H. Kuo, E. Kanal, A. K. Abu-Alfa, and S. E. Cowper. Gadolinium-based mr contrast agents and nephrogenic systemic fibrosis. *Radiology*, 242(3):647–649, 2007.

[258] R. Freytag M.Spahn, V.Heer. Flat-panel detectors in x-ray systems. *Radiologe*, 43:340–350, 2003.

[259] U. Nyman, B. Elmstahl, P. Leander, M. Nilsson, K. Golman, and T. Almen. Are gadolinium-based contrast media really safer than iodinated media for digital subtraction angiography in patients with azotemia? *Radiology*, 223(2):311–318, 2002.

[260] I. Fram P. Hua. Feature-basedimage registration for digital subtraction angiography. *SPIE*, 1898:24–31, 1993.

[261] M. Remy-Jardin, J. Bahepar, J. J. Lafitte, P. Dequiedt, O. Ertzbischoff, J. Bruzzi, V. Delannoy-Deken, A. Duhamal, and J. Remy. Multi-detector row ct angiography of pulmonary circulation with gadolinium-based contrast agents: prospective evaluation in 60 patients. *Radiology*, 238(3):1022–1035, 2006.

[262] S. Richard and J. H. Siewerdsen. Optimization of dual-energy imaging systems using generalized neq and imaging task. *Medical Physics*, 31(1):127–139, 2007.

[263] V. M. Runge, J. A. Clanton, C. M. Lukehart, C. L. Partain, and A. E. James. Paramagnetic agents for contrast-enhanced nmr imaging: a review. *Am J Roentgenol*, 141(6):1209–1215, 1983.

Lawrence M. Boxt Stephen Wilmot Miller and Suhny Abbara. Cardiac imaging.

Appendices

November 18, 2016

SPRINGER LICENSE
TERMS AND CONDITIONS

Dec 02, 2015

This is a License Agreement between Christiane Burton ("You") and Springer ("Springer") provided by Copyright Clearance Center ("CCC"). The license consists of your order details, the terms and conditions provided by Springer, and the payment terms and conditions.

All payments must be made in full to CCC. For payment instructions, please see information listed at the bottom of this form.

License Number	3760920053348
License date	Dec 02, 2015
Licensed content publisher	Springer
Licensed content publication	International Journal of Cardiac Imaging
Licensed content title	Left ventricular dual-energy digital subtraction angiography: a motion immune digital subtraction technique
Licensed content author	Michael S. Van Lysel
Licensed content date	Jan 1, 1991
Volume number	7
Issue number	1
Type of Use	Thesis/Dissertation
Portion	Figures/tables/illustrations
Number of figures/tables/illustrations	1
Author of this Springer article	No
Order reference number	None
Original figure numbers	7
Title of your thesis / dissertation	Energy-based subtraction angiography for cardiac application
Expected completion date	Feb 2016
Estimated size(pages)	200
Total	0.00 CAD

Terms and Conditions

Introduction

The publisher for this copyrighted material is Springer Science + Business Media. By clicking "accept" in connection with completing this licensing transaction, you agree that the following terms and conditions apply to this transaction (along with the Billing and Payment terms and conditions established by Copyright Clearance Center, Inc. ("CCC"), at the time that you opened your Rightslink account and that are available at any time at http://myaccount.copyright.com).

Limited License

Curriculum Vitae

Name: Christiane Sarah Burton

Year of birth: 1989

Education and Training

09/12-08/16   Ph.D. Candidate

                Department of Medical Biophysics

                University of Western Ontario

                London, Ontario, Canada

                Thesis:

                Supervisor: Dr. Ian A. Cunningham

09/07-04/11   B.Sc. (Hon.) Physics

                Ryerson University

                Toronto, Ontario, Canada

                Thesis:

Academic Awards, Scholarships, and Distinctions

03/16
3rd place for Young Investigator Symposium American Association of
Physicists in Medicine (AAPM) Spring Clinical meeting
National
$150 USD

05/15
Selected as being within top 2 % of PhD students in Canada 2015
National

03/15
1st place poster competition category: Medical Physics, Engineering
Imaging, Transplantation, Biomedical Devices, Surgical and Clinical
Studies
London Health Research Day
National
$ 500

09/13-08/14
Ontario Graduate Scholarship (OGS)
Provincial
$15,000 per year for 1 year

09/13-08/14
Schulich Graduate Scholarship
Institutional
The University of Western Ontario, London, Ontario, Canada
$6,670 per year for 1 year

09/12-09/13
Canadian Institutes of Health Research Strategic Training Program in
Vascular Research. Institutional
The University of Western Ontario, London, Ontario, Canada
$12,000 per year for 2 consecutive years

09/12-present
Western Research Graduate Scholarship
Institutional
The University of Western Ontario, London, Ontario, Canada
$2,500 per semester until graduation

05/11-08/11
Harold E Johns Summer Studentship in Medical Physics
National

Publications and Presentations

Peer-reviewed journal manuscripts (3 publications)

C. S. Burton, John R. Mayo, I. A. Cunningham. Energy Subtraction Angiography can compete with Digital Subtraction Angiography in Terms of Image SNR. Published in Medical Physics Journal 2016.

C. S. Burton, John R. Mayo, I. A. Cunningham. Optimization of iodine signal-to-noise ratio for energy-dependent and conventional x-ray angiography methods. Submitted to Medical Physics 2016.

C. S. Burton, John R. Mayo, I. A. Cunningham. Calibration and bone removal for energy-dependent subtraction methods. In preparation for submission in Medical Physics 2016.

Published Non-Peer Reviewed Journal Manuscript (1 publication)

C. Burton, I. Cunningham. A theoretical and experimental comparison of x-ray angiographic image quality using energy-dependent and conventional subtraction methods. Published in Proceedings in SPIE medical imaging 2015

Presentations

C. S. Burton, John R. Mayo, I. A. Cunningham. Energy-subtraction angiography for dynamic vascular imaging: Comparison of image quality with conventional methods. AAPM Spring Clinic 2016, Salt Lake City, UT.

C. S. Burton, John R. Mayo, I. A. Cunningham. Energy-subtraction angiography for dynamic vascular imaging: Comparison of image quality with conventional methods. COMP World Congress June 2015, Toronto, ON.

C. S. Burton, John R. Mayo, I. A. Cunningham. Energy-subtraction angiography for dynamic vascular imaging: Comparison of image quality with conventional methods. Canadian Student Research Forum 2015, Winnipeg, MB.

C. Burton, **I. A. Cunningham**. Energy-subtraction angiography for dynamic vascular imaging: Comparison of image quality with conventional methods. SPIE medical imaging conference Feb 2015, Orlando, FL.

C. Burton, I. A. Cunningham. Energy-subtraction angiography for dynamic vascular imaging: Comparison of image quality with conventional methods. Medical Biophysics Seminar Series 2014.

C. Burton, I. A. Cunningham. An X-Ray-Energy Subtraction Method to Enhance Arteries in Cardiac Imaging. Medical Biophysics Seminar Series 2013.

C. Burton, I. A. Cunningham. Signal and noise model of a novel energy-dependent x-ray angiographic technique. Guelph Mathematics Conference 2013, Guelph Ontario